SELF ASSEMBLY OF MICROSTRUCTURES

THESIS

Paul Emmanuel Kladitis, Second Lieutenant, USAF

AFIT/GE/ENG/97D-02

DEPARTMENT OF THE AIR FORCE
AIR UNIVERSITY
AIR FORCE INSTITUTE OF TECHNOLOGY

Wright-Patterson Air Force Base, Ohio

AFIT/GE/ENG/97D-02

SELF ASSEMBLY OF MICROSTRUCTURES

Paul Emmanuel Kladitis, B.S.E.E
Second Lieutenant, USAF

Presented to the Faculty of the Graduate School of Engineering
of the Air Force Institute of Technology
In Partial Fulfillment of the Requirements for the Degree of
Master of Science in Electrical Engineering

Approved:

Victor M. Bright, Ph.D., Committee Chairman
Department of Electrical and Computer Engineering — 24 Nov. '97 Date

Matthew Kabrisky, Ph.D., Committee Member
Department of Electrical and Computer Engineering — 24 Nov 97 Date

James A. Lott, Ph.D., Major, Committee Member
Department of Electrical and Computer Engineering — 24 Nov 97 Date

AFIT/GE/ENG/97D-02

SELF ASSEMBLY OF MICROSTRUCTURES

THESIS

Presented to the Faculty of the Graduate School of Engineering
of the Air Force Institute of Technology (AFIT)
Air University (AU)
Air Education and Training Command (AETC)
In Partial Fulfillment of the Requirements for the
Degree of Master of Science in Electrical Engineering

Paul Emmanuel Kladitis, B.S.E.E
Second Lieutenant, USAF

16 December 1997

Acknowledgments

I would like to acknowledge the Creator of the universe whose wonderful optimum designs I have tried to emulate. Although, "tried" is really too strong of a word. I would also like to thank Him for keeping my family safe and providing for us during my time at AFIT.

Being consumed with schoolwork and research, my participation with my family and ability to perform my share of household duties was lacking. I would like to thank my virtuous and faithful wife for keeping a joyful and peaceful attitude, managing the household, and skillfully raising our precious little daughter. I would also like to thank my daughter, born while at AFIT, for being a happy, content, carefree, and otherwise perfect little child. Bethany Blosser, my young Research Assistant, deserves credit for teaching me all about insects, especially in the way they walk.

I am grateful for Dr. Victor Bright, my academic advisor, thesis advisor, and thesis committee chairman, for always challenging me, urging me on, and combating my negative attitude with consistent encouragement. I would also like to thank Dr. Matthew Kabrisky and Major James Lott, my thesis committee members, for their sacrifice of time to help me. Also, Major John Comtois and USAF Philips Lab deserve thanks for their sponsorship of this research.

I also owe thanks to the MEMS Ph.D. students who, it seems, almost know everything -- Major Dave Burns, Major Bill Cowan, and Captain Jeff Butler sacrificed

their own, sparingly little, time to help me. Also, Captain Glenn Kading and Captain Joseph Bouchard, fellow MEMS classmates, were wonderful and easy to work with.

Special thanks goes to all the lab technicians who made it possible for me to have a successful laboratory experience. Bill Trop, my right hand man, never failed at getting me anything I needed or to show me how to use the equipment. Also thanks goes to Chris O'Brien for teaching me how to use the lab equipment. Thank you Belinda Johnson for assisting me in the physics lab. And last, but not least, thank you Gary Mauersberger, the head of the Engineering School's Computer Support, for his excellent computer assistance. If not for Gary, you would be reading a thesis written in crayon.

Although not from AFIT, but just as deserving in thanks are Dr. Junghsen Lieh and Dr. Joseph Slater from Wright State University. Great thanks goes to Dr. Lieh, one of the busiest men on the planet, for helping me with mechanical engineering problems. Dr. Slater also helped me with mechanical engineering and finite element analysis problems.

Paul E. Kladitis

Table of Contents

Table of Contents (Continued)

Table of Contents (Continued)

Page

List of Figures

Page

List of Figures (Continued)

Page

List of Figures (Continued)

Page

List of Figures (Continued)

Page

List of Figures (Continued)

Page

List of Figures (Continued)

Page

List of Figures (Continued)

Page

Abstract

In this research, four areas are investigated to develop microstructures whose operation transcends the plane of the substrate and to break new ground in developing micro unmanned vehicles. The four research areas are erecting microstructures normal to the substrate plane without direct human intervention (self assembled), providing low resistance electrical connections to the erected microstructure, realizing circular motion normal to the substrate plane, and implementing a microrobot. The designs in this research concentrate on erecting and providing power to a leg designed for use with the microrobot. The leg and the attached low resistance electrical connectors were not self assembled because the accompanying actuators were not powerful enough. However, the novel connectors provide the most practical, versatile, and lowest possible resistance connections for the MUMPs fabrication process. The microrobot was a 1 cm by 1 cm by 0.125 mm thick silicon chip with ninety-six legs micromachined on one side. The legs were able to support the weight of the chip but could not move the chip. The gold wires used to remotely power the legs restricted the chip's movement. The chip was turned over, and used as a micropositioner to transport a 1 cm by 1 cm by 0.023 mm piece of kapton film. A vertically deflecting actuator was used to bump the edge of a 222 μm diameter wheel, causing circular motion normal to the substrate.

1. Introduction

Since ancient times, mankind has striven to automate his tasks. Despair over routine manual labor was expressed by King Solomon when he pondered mankind's tasks [1]:

> *"What does a man get for all the toil and anxious striving with which he labors under the sun? All his days his work is pain and grief; even at night his mind does not rest. This too is meaningless."*

Today, a great challenge confronting engineers can be found in trying to automate the task of assembling microelectromechanical systems (MEMS). MEMS is an emerging engineering field birthed by the microelectronics industry and the present trend to miniaturize sensors. MEMS are micrometer-sized structures (microstructures) or systems of microstructures (micromachines) fabricated using the same techniques as used in microelectronic fabrication, the fabrication of transistors, computer chips, and other non-mechanical microelectronic devices. MEMS are usually fabricated from silicon. The actual fabrication process used here is described in detail in Chapter 3. Figure 1-1 shows captured video images of a section of a chip containing microelectronics and sections of a chip containing MEMS. The MEMS chip shows examples of micromachine components alongside a human hair for size perspective.

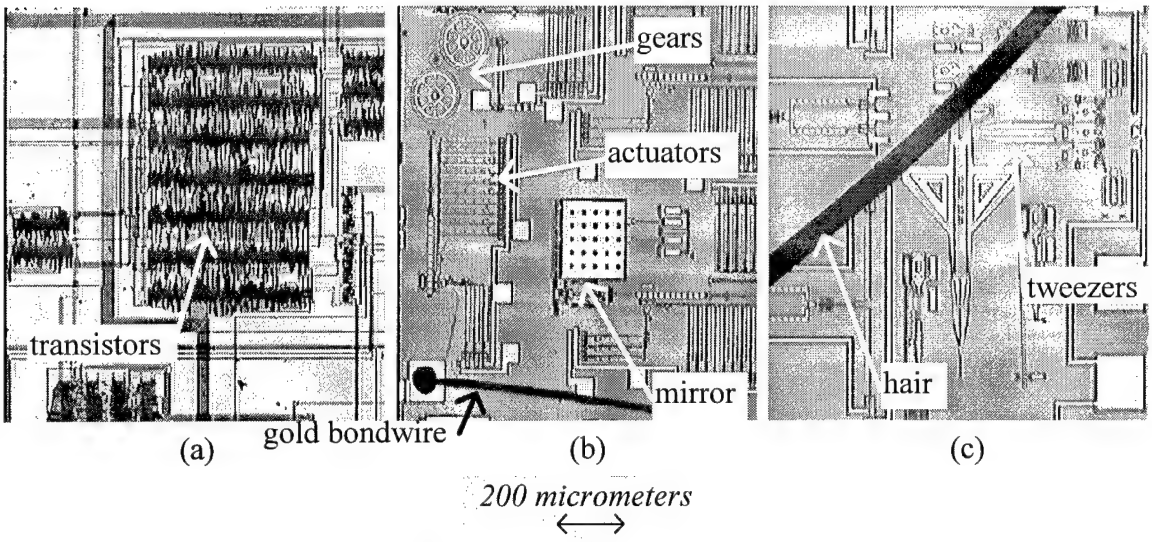

Figure 1-1: Captured video images of (a) a section of a microelectronics chip; (b) a section of a MEMS chip showing gears, actuators, hinged mirror, and a gold bondwire; and (c) another section of a MEMS chip showing microtweezers alongside a human hair for size perspective.

The present challenge with MEMS is to find ways to automate the manipulation of the microstructures which can be fabricated. By using automated manipulation, the number of applications for MEMS is expanded. Furthermore, MEMS then become reliable, can be mass-produced, and thus become economically feasible products [2, 3].

Human labor rules the day with structure manipulation in MEMS. MEMS structures can be manipulated by hand using microprobes and microscopes, but this method of manipulation is very time consuming, tedious, and unreliable due to the microscopic size of the structures. However, engineers are learning to manipulate and assemble MEMS without the use of the human hand.

1.1 Intent of Research

Present implementation of MEMS is limited by hand assembly and operation planar to the substrate surface. The research in this thesis concerns the inventions, innovations, and research relevant to automated manipulation, that is, the *self assembly* of MEMS. The goal of this research is to also develop new designs and techniques which will enable self assembly of microstructures, and realize system operation normal to the substrate surface, as well as, lateral operation.

This research is original: it does not work to a specific design; it does not follow prior research. The designs and research goals have originated in the author's imagination. Suggestions for designs have also come from the thesis advisor. The research goals are as follows:

1) Erect microstructures, originally in their parallel to the substrate post fabrication position, to a position normal to the substrate, using self assembly techniques. The substrate is the silicon wafer on top of which the MEMS are fabricated.
2) Provide electrical power to erected structures by means of practical low resistance electrical connections.
3) Realize circular motion normal to the substrate.
4) Realize a microrobot that can move on a flat surface.

MEMS are commonly fabricated from multiple layers of silicon or oxides of silicon, and are planar to the substrate's surface, having form and functionality much like flat paper cut-outs lying on a flat table; the paper cut-outs being compared to microstructures and the table being compared to the substrate. By nature of the fabrication process, MEMS are restricted to move or operate planar to the substrate surface. MEMS demonstrating motion normal to the substrate are a rarity. Furthermore, demonstrations of providing electrical power to MEMS which have been erected out of the substrates plane is an even greater rarity. Microstructures which demonstrate circular motion normal to the substrate's surface can be compared to the circular motion of a carnival Ferris wheel with respect to the earth. This type of motion has not been demonstrated with MEMS. However, circular motion parallel to the substrate's surface, similar to a carnival carousel, has been demonstrated. The development of practical methods and designs that realize MEMS operation out of the substrate's plane are applied to the creation of a microrobot.

1.2 Defining Self Assembly

The phrase "self assembly" in this document is defined as post fabrication manipulation or construction of microelectromechanical systems or structures necessary to enable intended operation, without the direct aid of a human operator. For example, sliding a microstructure into final operating position on a microchip indirectly by hand using probes is not considered self assembly. However, the same microstructure slid into

place by another microstructure, perhaps a micromotor, is considered self assembly; even though a human operator was needed to turn-on a supply of electricity for the process. Figure 1-2 shows a prototype design of a micromirror that has been slid into place for electrostatic actuation [4]. A linear, thermally actuated micromotor is used to slide the mirror. This MEMS design is considered a self assembled system.

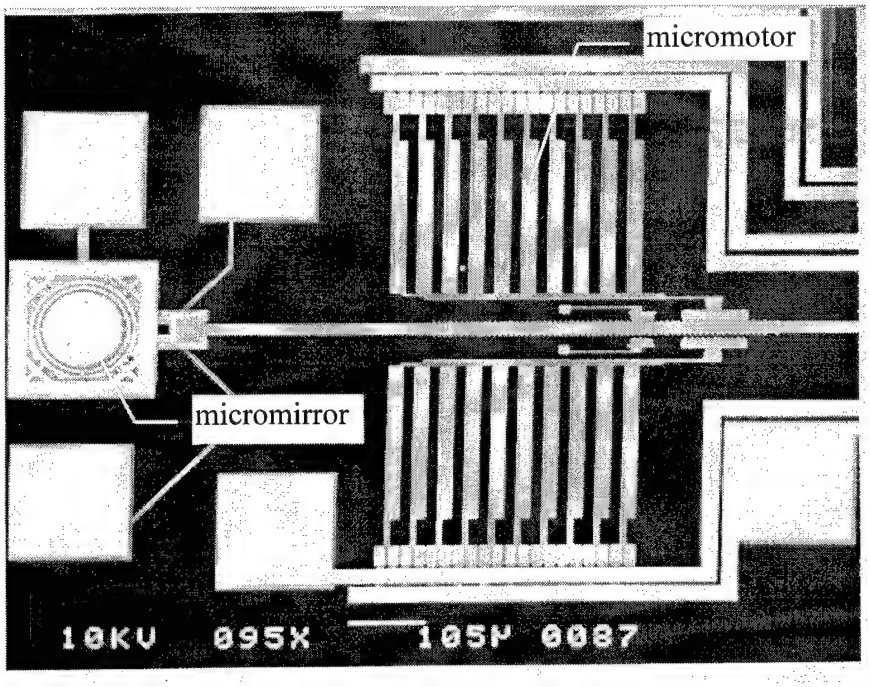

Figure 1-2: Scanning electron micrograph of a prototype self assembly system where a micromirror has been slid into place, for future electrostatic actuation, by a linear thermally actuated micromotor [4].

Other phrases found in the literature and the MEMS community that have the same meaning as "self assembly" are "micro assembly," "remote assembly," "electronic assembly," "micromanipulation" [5], and "self adjusting" [6].

1.3 Organization of Thesis

The remainder of this thesis is organized in the following manner. Chapter 2 is a literature survey on the background of self assembly. In this Chapter, relevant actuation methods for self assembly and existing self assembly schemes are reviewed.

Chapter 3 discusses the design tools, fabrication, and post processing used for the MEMS in this research. In Chapter 4, test equipment used for this research is described.

Due to the broad scope of the research goals and its "trial and error" nature where the design process and results are intimately related, experimental theory and design, and experimental results are presented in Chapter 5. Each research goal is covered seperately, from theory and design to results. It is hoped that this method of presentation will provide a clearer picture for the reader, than that of separating the theory and design from the results in different chapters. Chapter 6 concludes with a report of the final status of this research and recommendations for future research.

1.4 References

[1] *The Holy Bible*, Ecclesiastes, Chapter 2, Verses 22-23, New International Version, International Bible Society, 1984.

[2] T. Akiyama, D. Collard, E. H. Yang, and H. Fujita, "Scratch drive actuator with mechanical links for self-assembly of three-dimensional MEMS," *Journal of Microelectromechanical Systems*, vol. 6, no. 1, pp. 10-17, Mar. 1997.

[3] Y. Fukata, D. Collard, T. Akiyama, E. H. Yang, and H. Fujita, "Microactuated self assembling of 3D polysilicon structures with reshaping technology," *Proceedings of the IEEE MEMS Workshop*, pp. 477-481, 1997.

[4] D. Burns and V. Bright, "Designs to improve polysilicon micromirror surface topology," *Proceedings of SPIE*, San Jose, CA, vol. 3008, pp. 100-110, Feb. 10, 1997.

[5] S. Johansson, "Micromanipulation for micro- and nano-manufacturing," *Proceedings of the INRIA/IEEE Symposium on Emerging Technologies and Factory Automation*, vol. 3, pp. 3-8, 1995.

[6] M. Judy, Y. Cho, R. Howe, and A. Pisano, "Self-adjusting microstructures (SAMS)," *Proceedings of the IEEE MEMS Workshop*, pp. 51-56, 1991.

2. Background of Self Assembly

This chapter is a survey of existing technology relevant to the self assembly of microstructures. The literature review in Section 2.1 surveys self assembly topics relevant to this research. Topics covered in this section include: existing self assembly systems or methods; micro actuators or micro actuator systems which are, or conceivably could be, used for self assembly purposes; attempts at microrobot creation; and attempts at providing electrical power to erected micro structures. Section 2.2 concludes with a brief discussion of the usefulness of the reported technology to this thesis research.

2.1 Literature Survey

Few practical self assembly schemes and no commercial self assembly schemes of any form exist. Technology is usually market driven. The MEMS field is no exception. The present lack of commercial need for self assembly is probably a reason behind the slow development of self assembly techniques or microrobots. Current commercial MEMS for example: scanning-force microscope tips, accelerometers for auto airbags, gas sensors, pressure sensors, gyroscopes, and spray nozzles, do not require self assembly [1].

Nonetheless, the MEMS field stands poised on the edge of a major technological advance, with self assembly being the advancing agent. This advancement may be comparable to the microelectronics revolution [2]. The possible uses for self assembly

systems are endless, including: microsurgeons operating in the blood stream, reduction of space vehicle payloads due to miniaturized equipment, cleaner fabrication of micro and nano devices due to reduced human interaction, optical switching, microspies/reconnaissance, laser guidance mechanisms on-board of microchips, microoptical benches, micro assembly lines (machines building machines), sonar guided explorers, small quarters inspectors/repairers, and micro weapons [2, 3, 4].

Self assembly technology is gaining momentum. The government is sponsoring research in this field. The Defense Advanced Research Projects Agency (DARPA) has awarded sponsorship to a project involving MEMS-based active control of macro-scale objects and microrobot assembly systems, and is proposing $20 million worth of funding for research into micro unmanned aerial vehicles (MAVs) for the battlefield [5, 6, 7].

The rest of this section discusses existing components which can or do make possible self assembly systems. Section 2.1.1 reviews various types of actuators which could be harnessed or integrated into self assembly systems. Section 2.1.2 reviews existing self assembly schemes. Section 2.1.3 discusses some attempts at microrobots and small scale robots. Finally, Section 2.1.4 contains a review of connecting structures and attempts at supplying electrical power to erected micro structures.

2.1.1 Review of Actuation for Use in Self Assembly Systems

Several types of actuators are currently being used or could be used in self assembly. These actuators vary in material and operating principle. The following is literature survey of some of the known actuators in use in MEMS.

2.1.1.1 Thermal Actuators

Thermal actuators operate by taking advantage of the thermal expansion of a material. These actuators can be fabricated to move vertically or horizontally with reference to the substrate's surface. Henceforth, motion described as being horizontal or vertical will be with reference to the substrate surface associated with the device or system discussed.

A drawing of a horizontally deflecting thermal actuator is shown in Figure 2-1. Here, as current is applied through the device through the anchor/probe pads, the current causes the thin hot arm to heat up more than the wide cold arm. As a result, the hot arm expands more than the cold arm and the actuator flexes in the direction shown in the figure (a positive deflection). The drive current is restricted from heating up the hot arm to the point of plastic deformation.

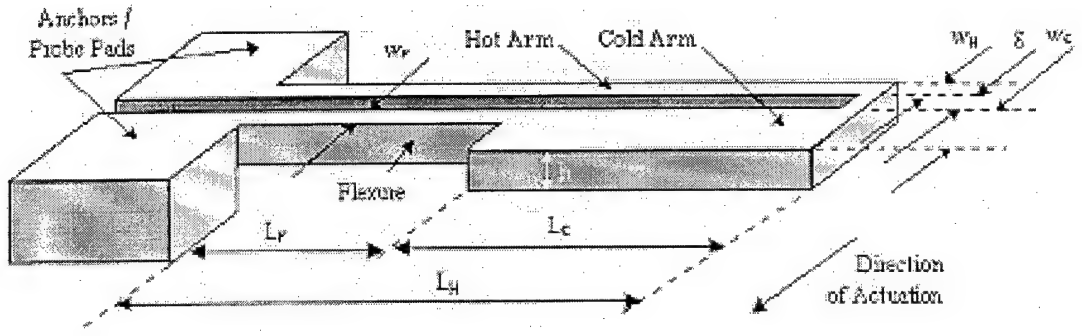

Figure 2-1: Drawing of a horizontally deflecting thermal actuator [8].

This type of actuator has been studied and fabricated extensively [8, 9]. Optimum dimensions for this device, fabricated from polysilicon of thickness h, have been determined: $w_h = 1.25 \times h$, $w_c = 7 \times w_h$, and $L_f = (1/3) \times L_c$. For an actuator with dimensions $w_h = 2\ \mu m$, $w_c = 14\ \mu m$, $L_f = 40\ \mu m$, and $L_c = 160\ \mu m$, deflections on the order of 12 μm at 4.5 mA of current have been measured and forces on the order of 4.4 μN have also been measured. Microgrippers, actuated by the horizontally deflecting thermal actuators, are shown in Figure 2-2 [8].

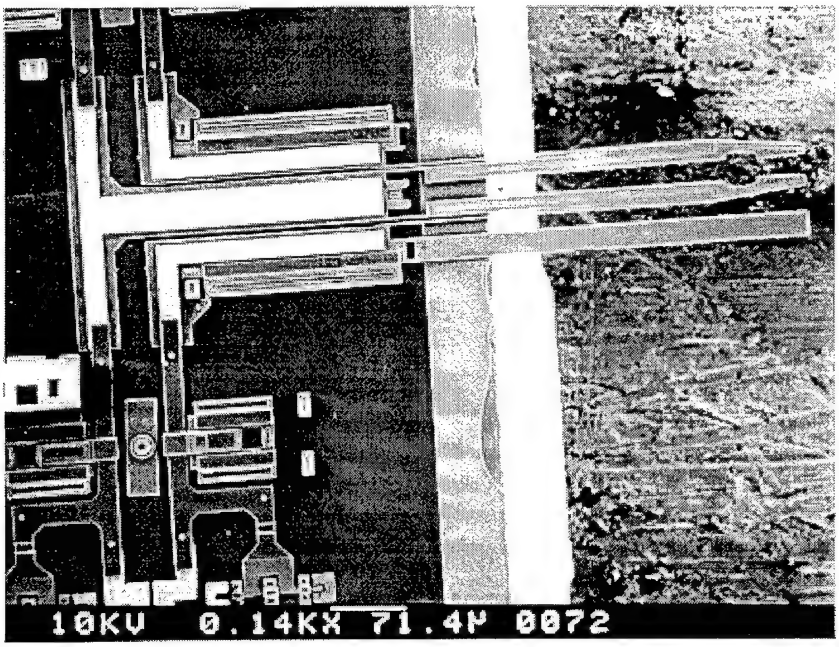

Figure 2-2: Scanning electron micrograph of thermally actuated microgrippers hanging over the edge of a micro chip [8].

The horizontally deflecting and the vertically deflecting (discussed next) thermal actuators can be operated in two modes: forward and back bent mode. Operation in forward mode has already been described in the previous paragraph. The back bent mode of operation occurs after the hot arm has been heated, by appropriate over-driving of current, to the point of plastic deformation. As the hot arm cools, it deforms and shrinks, causing the actuator to permanently deflect in a negative direction. After this one time over-driving of current, the actuator can be operated as in the forward mode [9].

Figure 2-3 shows a vertically deflecting thermal actuator lifting a mirror after being back bent. This type of actuator works on the same principle as the actuator described above except that the hot arm and cold arm are arranged above or below each

other instead of side by side as in the horizontally deflecting case.

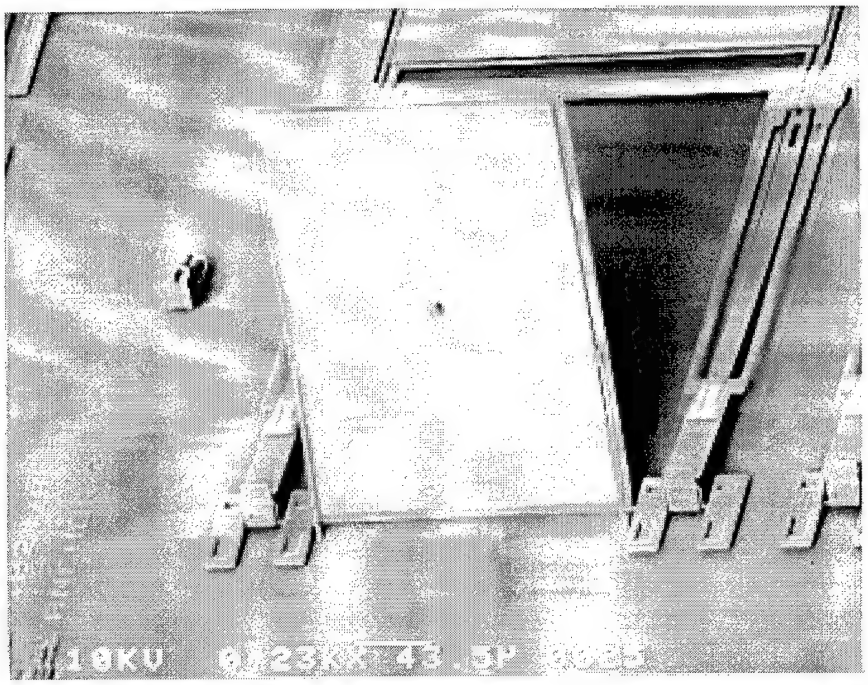

Figure 2-3: Scanning electron micrograph of a micro mirror erected to an almost vertical position by a back bent, vertical, thermal actuator [10].

Another type of vertically deflecting actuator referenced in the literature is a three layer polyimide/metal/polyimide bimorph actuator [11]. The bottom layer is a polyimide with a smaller thermal expansion coefficient than the top polyimide layer. A metal heater layer is sandwiched in between the polyimide layers. After fabrication, the free end of the structure is initially curled away from the substrate (typically 250 μm) because of residual stress. When the heater is powered, the top layer expands more than the bottom layer causing the structure to uncurl. Figure 2-4 shows a drawing of this actuator. Arrays

of these actuators have been used to convey pieces of silicon (dimensions 2.6 mm x 1.5 mm x 0.26 mm, and mass 2.4 mg) across the substrate.

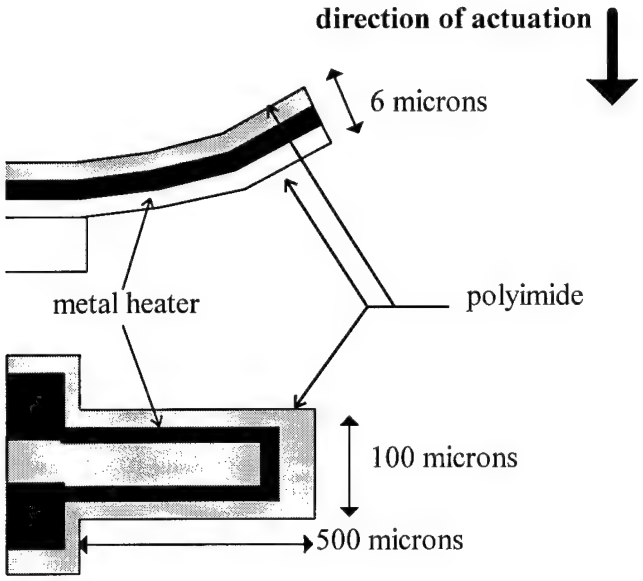

Figure 2-4: Drawing of polyimide bimorph actuator showing layers and direction of actuation.

2.1.1.2 Electrostatic Actuators

Electrostatic actuation takes advantage of the attraction or repulsion of charged surfaces. Ideally, there is no current flow in these devices, but the operating voltages can be large (i.e. greater than 100 V) [8]. However, a novel low voltage electrostatic actuator has been developed [12]. The operating voltage (11.8 V) is reported to be CMOS compatible. Many examples of electrostatic actuators exist. The following is a survey of some of the different types.

One type of actuator can be levitated 50-200 μm above the substrate surface and

made to deflect horizontally [13]. Conducting pads are fabricated on a 24 mm x 24 mm x 180 μm microscope cover slip (actuator) and on a glass plate (fixed stator). The capacitance between the conducting plates in series with external inductors and an ac drive signal form a tuned circuit which enables the actuator to be levitated below the fixed stator.

Another type of electrostatic actuator is a polysilicon plate suspended above the substrate surface by polysilicon flexures [8]. Actuation is achieved by applying a differential voltage between the suspended plate and a contact on the substrate (or the substrate itself). The plate is attracted toward the substrate.

Elwenspoek et al. developed an electrostatic actuator made from two layers joined at one end, but still electrically isolated [14]. Because one of the layers is constructed as a bimorph, it is normally curled away from the other layer. When a differential voltage is applied between the two layers, the curled layer is attracted back to the uncurled layer. It has been proposed by the authors that this structure can be used as active joints (or muscles) for microrobot limbs.

Electrostatic actuators can be arrayed together and used as a drive source for a motor. One such array is called a comb drive, and is composed of arrays of parallel plates electrostatically attracted to each other by an ac drive voltage [15]. This motor converts linear motion of the actuator into rotational motion of an output gear, which can be coupled to other structures to provide a motive force for self assembly.

2.1.1.3 Electromagnetic Actuators

Electromagnetic actuators exist which operate on the same principle as macro electric motors. In fact, a majority of microelectromagnetic actuators are motors, and are mostly fabricated using the Lithographie Galvonoformung Abformung (LIGA) process [8].

2.1.1.4 Residual Stress Actuators

Judy et al. developed a method of self assembly or self adjusting microstructures (SAMS) using the residual stress of silicon nitride on polysilicon to provide horizontal or vertical deflection, with respect to the substrate, after being released [16]. Beginning with a polysilicon surface, a thin layer of oxide is deposited. Next, a thin layer of polysilicon is deposited on top of the oxide. However, one end of the thin polysilicon layer is anchored to the original polysilicon surface through a window etched in the oxide. Finally, a thin layer of silicon nitride is deposited on the thin polysilicon layer. When the oxide is etched away (released), the free end of the thin polysilicon layer is free to curl away from the original silicon surface due to the residual stress of the nitride layer on the polysilicon. The authors report that the curled polysilicon layer can be used to push or adjust micro structures into a final operating position.

2.1.1.5 Pneumatic, Shape Memory Alloy (SMA), and Magnetostrictive Actuators

Other examples of actuation include pneumatic actuation, where a small tube containing three inner chambers has the pressures varied differentially between the three chambers causing the tube to flex in a specified direction. Also, shape memory alloys can be used as actuators by heating the SMA flexure causing its shape to change. And finally, flexures can be fabricated from magnetostrictive materials which change shape when introduced to a varying magnetic field. These three methods of actuation can be used as microrobot joints or limbs. Also, flexures made by these techniques, can be used to propel or manipulate a microstructure [2].

2.1.1.6 Thermodynamic Actuators

A microactuator is reported which harnesses the thermal expansion of a fluid in a microcylinder via a piston [17]. Energy is imparted to the fluid filled microcylinder by light incident from a laser beam.

2.1.1.7 Piezoelectric Actuators

Actuation using piezoelectric materials which take advantage of the piezo effect, converting electrical energy into mechanical energy, can be used for self assembly systems. Many piezoelectric micromotors have been reported [4, 18], also piezo flexures

used to propel miniature robots have been reported [2].

2.1.2 Review of Self Assembly Schemes

This section describes different self assembly methods or self assembly systems reported in the literature. These include the scratch drive actuator and various micromirror positioners. One micromirror positioning system has already been described in Section 1.2 [19].

2.1.2.1 Scratch Drive Actuator (SDA)

Figure 2-5 shows the scratch drive self assembly process [20]. A scratch drive is an electrostatic actuator driven by an ac signal. Figure 2-5 (a) shows the original structure before self assembly, Figure 2-5 (b) shows the SDA moving to the left causing the polysilicon plate to rise, Figure 2-5 (c) shows the SDA held in place while a dc current is applied though the SDA causing the polysilicon to heat up and plastic deformation to occur, and finally, Figure 2-5 (d) shows the final position of the microstructure. Figure 2-6 shows the actuator alone, and illustrates how the applied drive signal causes movement.

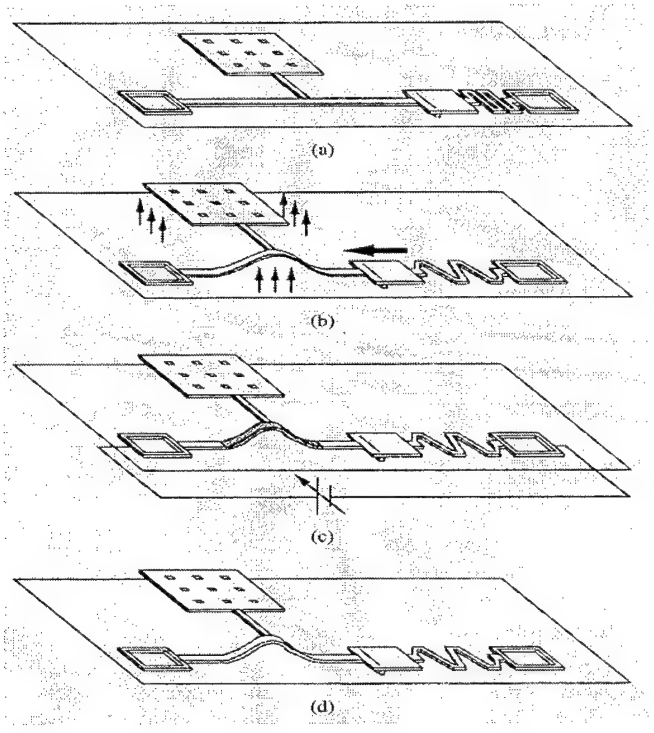

Figure 2-5: Illustration of 3-D self-assembled polysilicon structure showing assembly process [20].

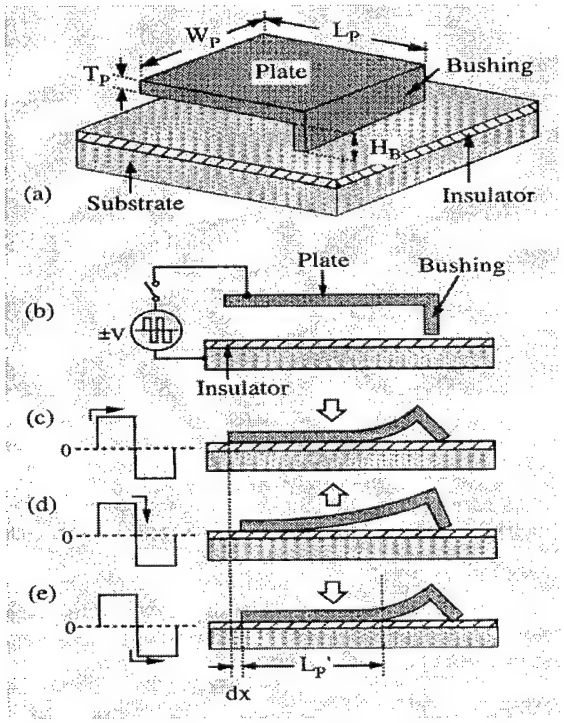

Figure 2-6: Illustration of SDA movement [20].

2.1.2.2 Thermally Actuated Systems

Figure 2-7 shows an example of vertically deflecting thermal actuators integrated into a self assembly system [10]. Three actuators are used to maneuver a micro mirror into operating position after being back bent. Figure 2-8 also shows the actuators integrated into a self assembly system [10]. Here, a whole array of micromirrors has been erected to an almost vertical position by back bent thermal actuators.

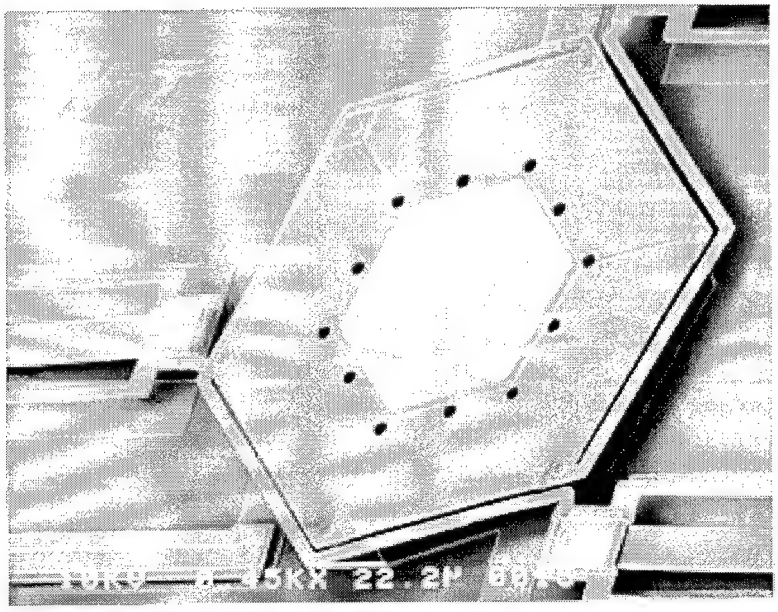

Figure 2-7: Scanning electron micrograph of a hexagonal mirror elevated into position by three backbent vertical thermal actuators [10].

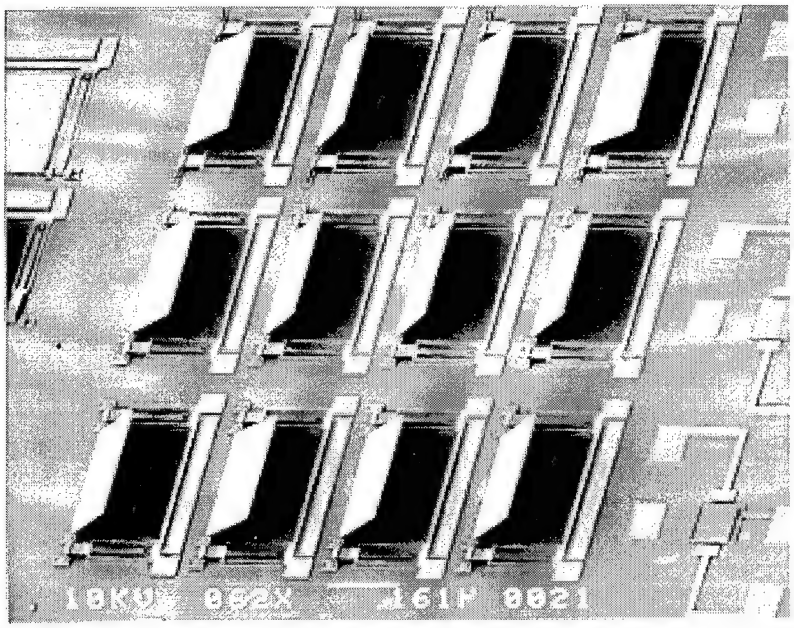

Figure 2-8: Scanning electron micrograph of array of micro mirrors erected to an almost vertical position by back bent vertical thermal actuators [10].

Figure 2-9 shows a full view of another micro mirror self assembly system [21]. The function of this MEMS is to raise the square micro mirror by an initial lift using the vertical deflecting thermal actuator located near its base. Next, a rack connected to the mirror and powered by an array of horizontally deflecting thermal actuators pushes the mirror up the rest of the way to its final, perpendicular to the substrate, position. Once the mirror is close to being perpendicular with the substrate, a locking tab is engaged. This locking tab is also connected to a thermal actuator array, which is then used to wiggle the mirror. Figure 2-10 shows the mirror partially lifted, and a close up of the back bent vertical thermal actuator.

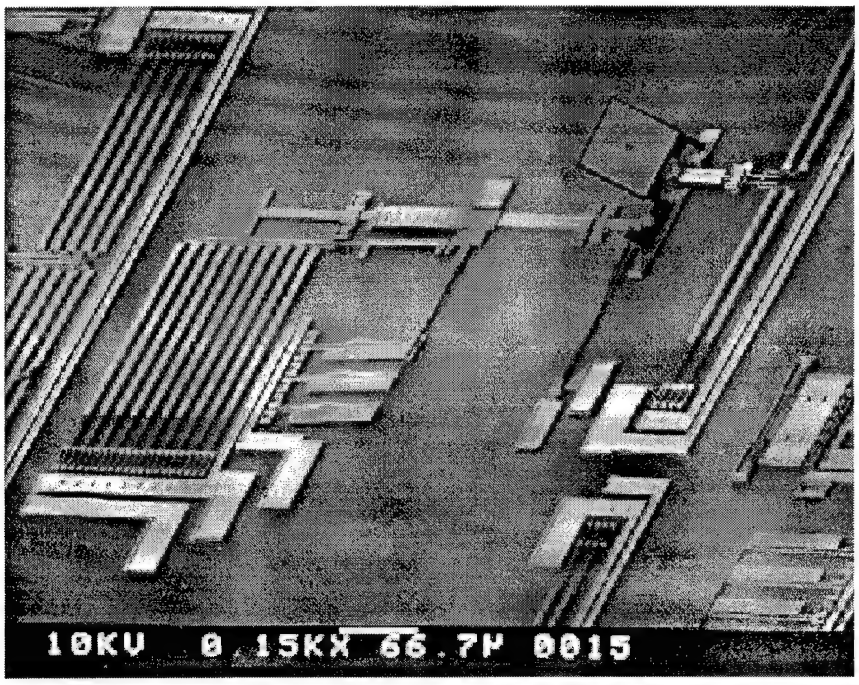

Figure 2-9: Scanning electron micrograph of mirror self assembly system [21].

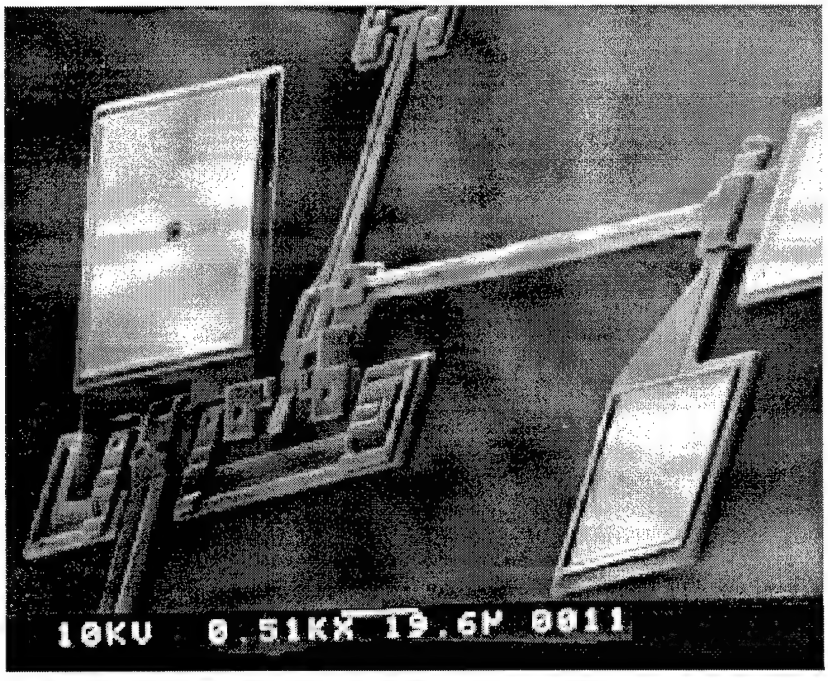

Figure 2-10: Scanning electron micrograph showing mirror partially assembled by vertically deflecting thermal actuator [21].

2.1.2.3 Fractal Structures

Shahinpoor proposes that highly expandable/collapsible folding structures (fractal structures) be used as deployable microrobot arms or manipulators [22]. Several designs are presented. Some of the designs could be patterned in two dimensions on the substrate, and then deployed using any of the various actuation techniques described in this paper.

2.1.2.4 Fluidic and Vibrational

One self assembly technique is performed by flowing fluid over micromachined plates [23]. Initially, the plates are in their post fabrication position parallel to the substrate. The drop in pressure over the surface of the plates causes the plates to rise to an upright position and lock into strategically placed locking tabs. Another form of fluidic assembly reported in the literature is performed by passing a liquid slurry, containing specially shaped micro structures, over a substrate which has bulk micromachined receptors [24]. The receptors are the same shape as the microstructures suspended in the slurry. Random processes cause the free microstructures to arrange themselves and fit into the receptors. Similarly, another form of self organization is reported by placing specially shaped microstructures on a vibrating surface, where random processes cause the structures to arrange themselves [25].

2.1.2.5 Off Chip Assembly

Other forms of self assembly or remote assembly reported are by assembling or handling microstructures with a high precision macro "probe station" outfitted with micro grippers and other micro sized manipulators [3]. Also, fabricating 3-D structures using ion milling could be considered as self assembly, in that the device is already assembled [26].

2.1.3 Review of Microrobot Schemes

In this research, micro sized robots (microrobots) are considered synonymous with self assembly, therefor, reviewing microrobots adds to the collective knowledge of self assembly. To this end, this section surveys some of the different microrobot systems found in the literature. The existence of a microrobot can imply self assembly techniques or systems. For instance, suppose a microfish has been created and swims in water. It can be considered a microrobot, and by nature of its micro size and autonomous behavior possesses self assembly systems or components [27, 28].

Robots have been classified by size into three categories [2]: miniature robots, microrobots, and nanorobots. A microrobot's size is on the order of micrometers; most likely a modified chip fabricated with silicon micromachining technologies; and containing actuators, sensors, and/or processing. A nanorobot would operate and be modeled on a scale similar to the biological cell.

An operational 7-mm microfabricated car is reported in the literature [29]. Although this machine is not truly a micromachine, its small size makes it a valuable example from which to draw conclusions. For instance, it was determined from the report that for rough surfaces, other forms of propulsion, other than wheels, should be used for micromachines or microrobots.

Shimoyama et al. attempt to realize microflight of a microstructure that is anchored to a silicon substrate [30]. The microstructure possesses wings made from polyimide and nickel. The structure is introduced into an alternating magnetic field which causes the wings to flap. The authors claim that their microflight mechanism shows true promise for actual flight. If actual flight is achievable, this flying scheme could be harnessed as an actuation method for self assembling microstructures, besides being a microrobot.

A miniature robot actuated and controlled by vibration operates by taking advantage of resonant frequencies of different geometry structures [31]. This idea could possibly be scaled to the micro level to be used in self assembly.

In working towards a silicon microrobot, several microrobot components are reported [32, 33], including: hollow triangular beams that can be rotated off of the substrate individually or chained together forming a robot arm allowing 6 degree-of-freedom movement. Actuators or linkage can be placed inside the hollow triangular beams for strategic actuation of joints.

Other reported microrobot components which could be part of self assembly systems are elastic polyimide hinges and silicon exoskeletons formed from two

dimensional fabrication using simple paper folding techniques [34, 35].

2.1.4 Connecting Structures and Electrical Power to Erected Micro Structures

Figure 2-11 shows two microstructures tethered together [36]. This simple tether structure enables multiple microstructures to be assembled at one time. The two microstructures are part of a microinterferometer. One of the structures is a beam splitter grating, and the other is a DC block plate used to block the zero order energy coming through the grating.

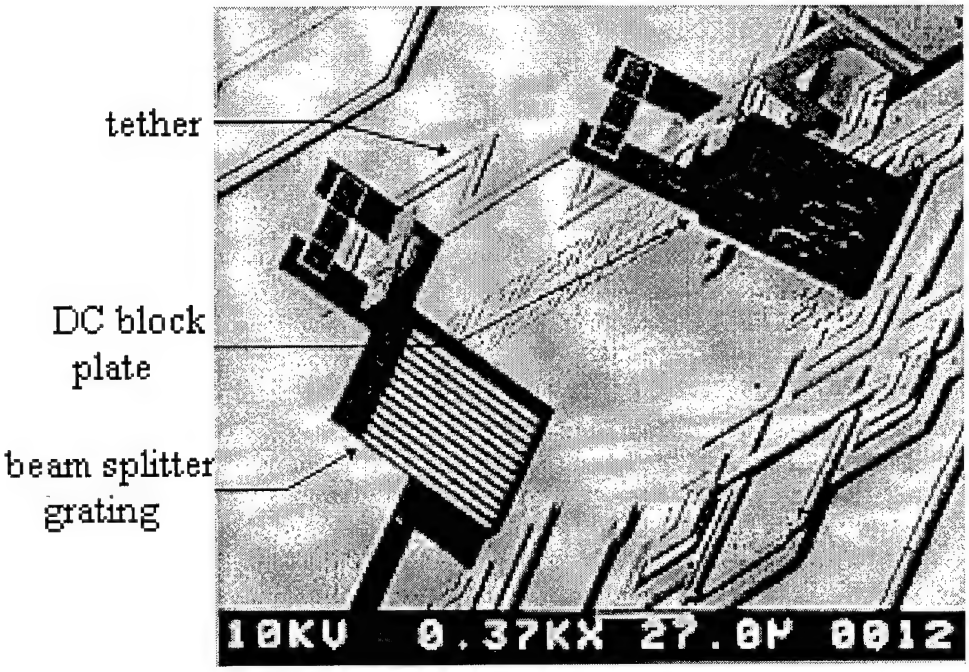

Figure 2-11: Scanning electron micrograph of a microinterferometer where a tether has been used to assemble two microstructures simultaneously [36].

Figure 2-12 is a drawing of a hinged wire. A hinged wire is a microstructure used to make low resistance electrical contact to an erected microstructure. The hinged wire is initially fabricated planar to the substrate surface. The hinged wire can be flipped over and laid across an erected microactuator to provide a contact for electrical power. Figure 2-13 shows a scanning electron micrograph of hinged wire contacting a flip-up infrared light source [8].

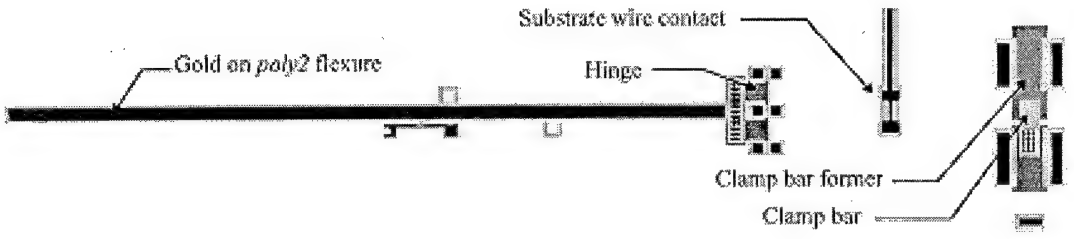

Figure 2-12: Drawing of hinged wire [8].

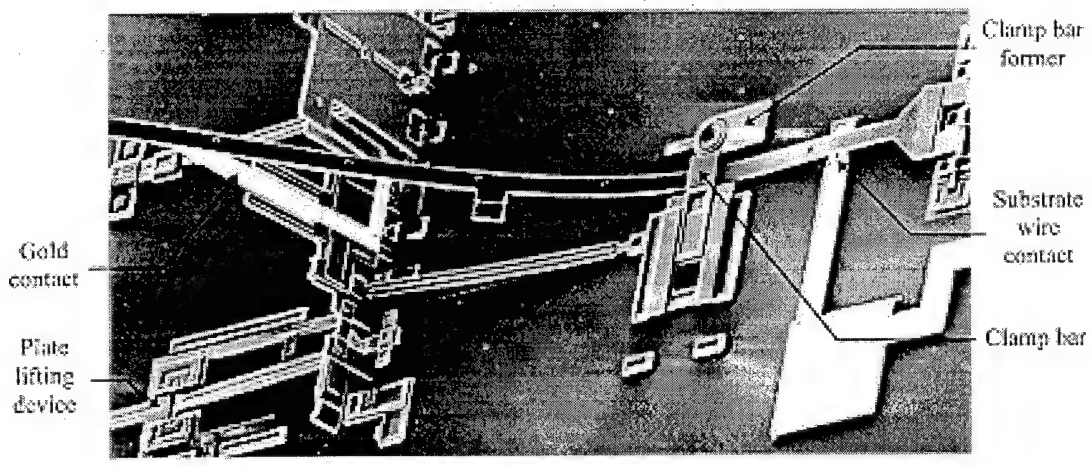

Figure 2-13: Scanning electron micrograph of hinged wire powering a flip-up infrared light source [8].

2.2 Conclusions

The designs and techniques developed in this thesis research are restricted to fabrication through a commercial surface micromachining process, specifically, the Multi-User MEMS Process (MUMPs) by MCNC [37] which will be described in detail in Chapter 3. Most of the designs presented in this literature review were not fabricated using MUMPs, and therefore, could not be used directly in this research. Nonetheless, insights gained from studying these designs were used for this research. The designs developed at AFIT, however, were fabricated using MUMPs, and are indeed used as building blocks in this thesis research.

2.3 References

[1] R. Allan, "Silicon MEMS technology is coming of age commercially," *Electronic Design*, pp. 75-88, 20 Jan. 1997.

[2] P. Dario, R. Valleggi, M. C. Carrozza, M. C. Montesi, and M. Cocco, "Microactuators for microrobots: A critical survey," *Journal of Micromechanics and Microengineering*, vol. 2, no. 3, pp. 141-157, Sep. 1992.

[3] S. Johansson, "Micromanipulation for micro- and nano-manufacturing," *Proceedings of the INRIA/IEEE Symposium on Emerging Technologies and Factory Automation*, vol. 3, pp. 3-8, 1995.

[4] M. Flynn, L. Tavro, S. Bart, R. Brooks, D. Ehrlich, K. Udayakumar, and L. Cross, "Piezoelectric micromotors for microrobots," *IEEE/ASME Journal of Microelectromechanical Systems*, vol. 1, no. 1, pp. 44-51, Mar. 1992.

[5] A. Berlin, "MEMS-based active control of macro-scale objects," DARPA Project, Xerox Palo Alto Research Center, POC phone (415) 812-4372.

[6] P. Will, "Microrobot assembly systems (MASS), " DARPA Project, University of Southern California, Information Sciences Institute, POC phone (213) 822-1511.

[7] Jane's International Defence Review, February 1997.

[8] J. Comtois, *Structures and techniques for implementing and packaging complex, large scale microelectromechanical systems using foundry fabrication processes.* Doctoral Dissertation, Air Force Institute of Technology, Wright-Patterson AFB, Ohio, AFIT/DS/ENG/96-04, 12 May 1996.

[9] J. Reid, *Microelectromechanical isolation of acoustic wave resonators.* Doctoral Dissertation, Air Force Institute of Technology, Wright-Patterson AFB, Ohio, AFIT/DS/ENG/96-12, Dec. 1996.

[10] W. Cowan and V. Bright, "Vertical thermal actuators for micro-opto-electro-mechanical systems," *Proceedings of SPIE*, Austin, TX, vol. 3226, pp. 137-146, Sep. 1997.

[11] M. Ataka, S. Omofsks, N. Takeshima, and H. Fujita, "Fabrication and operation of polyimide bimorph actuators for a ciliary motion," *IEEE/ASME Journal of Microelectromechanical Systems*, vol. 2, no. 4, pp. 146-150, Dec. 1993.

[12] T. Yasuda, I. Shimoyama, and H. Miura, "CMOS drivable electrostatic microactuator with large deflection," *Proceedings of the IEEE MEMS Workshop*, pp. 90-95, 1997.

[13] S. Kumar and D. Cho, "Electrostatically levitated microactuators," *Journal of Micromechanics and Microengineering*, vol. 2, no. 2, pp. 96-103, June 1992.

[14] M. Elwenspoek, L. Smith, and B. Hok, "Active joints for microrobot limbs," *Journal of Micromechanics and Microengineering*, vol. 2, no. 3, pp. 221-223, Sep. 1992.

[15] E. Garcia and J. Sniegowski, "Surface micromachined microengine," *Sensors and Actuators, A: Physical*, vol. 48, no. 3, pp. 203-214, 30 May 1995.

[16] M. Judy, Y. Cho, R. Howe, and A. Pisano, "Self-adjusting microstructures (SAMS)," *Proceedings of the IEEE MEMS Workshop*, pp. 51-56, 1991.

[17] W. Nogimori, K. Irisa, M. Ando, and Y. Naruse, "A laser-powered micro-gripper," *Proceedings of the IEEE MEMS Workshop*, pp. 267-271, 1997.

[18] M. Bexell, A. Tiensuu, J. Schweitz, J. Soderkvist, and S. Johansson, "Characterization of an inchworm prototype motor," *Sensors and Actuators, A: Physical*, vol. 43, no. 1, pp. 322-329, 3 May 1994.

[19] D. Burns and V. Bright, "Designs to improve polysilicon micromirror surface topology," *Proceedings of SPIE*, San Jose, CA, vol. 3008, pp. 100-110, Feb. 10, 1997.

[20] T. Akiyama, D. Collard, E. H. Yang, and H. Fujita, "Scratch drive actuator with mechanical links for self-assembly of three-dimensional MEMS," *Journal of Microelectromechanical Systems*, vol. 6, no. 1, pp. 10-17, Mar. 1997.

[21] J. Reid, V. Bright, and J. Comtois, "Automated assembly of flip-up micromirrors," *International Conference on Solid-State Sensrs and Actuators, Transducers '97*, Chicago, IL, pp. 347-350, Jun. 1997.

[22] M. Shahinpoor, "Introduction to smart fractal structures and mechanisms," *ASME Intelligent Structures, Materials, and Vibration*, vol. 58, pp. 67-74, 1993.

[23] S. Burgett, K. Pister, and R. Fearing, "Three dimensional structures made with microfabricated hinges," *Proceedings of the Winter Annual Meeting of the American Society of Mechanical Engineering*, Dynamic Systems and Control Division, DSC vol. 40, pp. 1-11, 1992.

[24] H. Yeh, and J. Smith, "Fluidic self-assembly of microstructures and its application to the integration of GaAs on Si," *Proceedings of the IEEE MEMS Workshop*, pp. 279-284, 1994.

[25] M. Cohn and C. Kim, "Self-assembling electrical networks: An application of micromachining technology," *International Conference on Solid-State Sensors and Actuators, Transducers '91*, pp. 490-493, 1991.

[26] Y. Hatamura, M. Nakao, T. Sato, K. Koyano, K Ichiki, and H. Sangu, "Construction of 3-d micro structure by multi-face FAB, Co-Focus Rotational Robot and various Mechanical Tools," *Proceedings of the IEEE MEMS Workshop*, pp. 297-302, 1994.

[27] T. Fukada, A. Kawamoto, F. Arai, and H. Matsuura, "Micro mobile robot in fluid (1st report, mechanism and swimming experiment of micro mobile robot in water)," *Transactions of the Japan Society of Mechanical Engineers*, part C, vol. 60, no. 569, pp. 204-210, 1994.

[28] C. Liu, T. Tsao, Y. Tai, W. Liu, P. Will, and C. Ho, "Micromachined permalloy magnetic actuator array for micro robotics assembly systems," *Proceedings of the International Conference on Solid-State Sensors and Actuators, Eurosensors IX*, vol. 1, pp. 328-331, 1995.

[29] A. Teshigahara, M. Watanabe, N. Kawahara, Y. Ohtsuka, and T. Hattori, "Performance of a 7-mm microfabricated car," *IEEE/ASME Journal of Microelectromechanical Systems*, vol. 4, no. 2, pp. 76-80, June 1995.

[30] I. Shimoyama, Y. Kubo, T. Kaneda, and H. Miura, "Simple microflight mechanism on silicon wafer," *Proceedings of the IEEE MEMS Workshop*, pp. 148-152, 1994.

[31] T. Yasuda, I. Shimoyama, and H. Miura, "Microrobot actuated by a vibration energy field," *Sensors and Actuators, A: Physical*, vol. 43, no. 1, pp. 366-370, 3 May 1994.

[32] R. Yeh, E. Kruglick, and K. Pister, "Towards an articulated silicon microrobot," Proceedings of ASME Dynamic Systems and Control, vol. 2, pp. 747-754, 1994.

[33] R. Yeh, E. J. J. Kruglick, and K. S. J. Pister, "Surface-micromachined components for articulated microrobots," *IEEE/ASME Journal of Microelectromechanical Systems*, vol. 5, no. 1, pp. 10-17, Mar. 1996.

[34] K. Suzuki, I. Shimoyama, and H. Miura, "Insect-model based microrobot with elastic hinges," *IEEE/ASME Journal of Microelectromechanical Systems*, vol. 3, no. 1, pp. 4-9, Mar. 1994.

[35] K. Suzuki, I. Shimoyama, H. Miura, and Y. Ezura, "Creation of an insect based microrobot with an external skeleton and elastic joints," *Proceedings of the IEEE MEMS Workshop*, pp. 190-195, 1992.

[36] D. Sene, "Design, fabrication, and characterization of micro-opto-electro-mechanical systems," Master's Thesis, Air Force Institute of Technology, Wright-Patterson AFB, Ohio, AFIT/GEO/ENP/95D-03, Dec. 1995.

[37] D. Koester, R. Mahadevan, and K. Markus, "SmartMUMPs design handbook including MUMPs introduction and design rules," rev. 4, DARPA project (DABT 63-93-C-0051) of MEMS Technology Applications Center MCNC, 3021 Cornwallis Road, Research Triangle Park, NC 27709, 1996.

3. Design, Fabrication, and Post Processing

This chapter discusses the design tools, fabrication, and post processing used for the MEMS in this research. Sections 3.1 - 3.3 describe the design process of the MEMS, from conception to testing: computer aided drawing design, fabrication process, and release process, respectively.

3.1 Computer Aided Drawing (CAD) Design of a Microstructure

The method of creating MEMS involves designing a CAD schematic of the desired microstructures, sending the CAD schematic to a commercial fabrication company, and finally receiving the fabricated microstructures on 1 cm x 1 cm die where a release process is performed in an AFIT laboratory. The CAD design involves simply drawing a picture of the desired microstructure on the computer with a mouse. Shapes of any geometric pattern may be created, and the structural material used to create that shape can be specified. The CAD program used to design the MEMS is CADENCE version 9502 distributed by Cadence Design Systems, Inc. [1]. CADENCE was originally meant for VLSI design and simulation, but was adapted for creating MEMS by providing the appropriate technology file. The technology file is a data file that specifies the available MEMS structural layers, the appearance of the structural layers when displayed on the computer screen, the relationships between the layers, and how the drawing of the layers is translated into the mask file format. The mask file is a representation of the CAD

drawing of the MEMS which the commercial fabricators use to create their fabrication masks. The mask file format used is the Caltech Intermediate Format, more commonly referred to as ".CIF" file format. The mask file is sent to the commercial fabrication company by electronic mail. CADENCE is run on a SPARC 20 SUN Workstation running at 75 MHz with 128 Mbytes of RAM. For comparison, Figure 3-1 (a) shows an example of a CADENCE drawing of a horizontally deflecting thermal actuator, and Figure 3-1 (b) shows the same microstructure after fabrication and release.

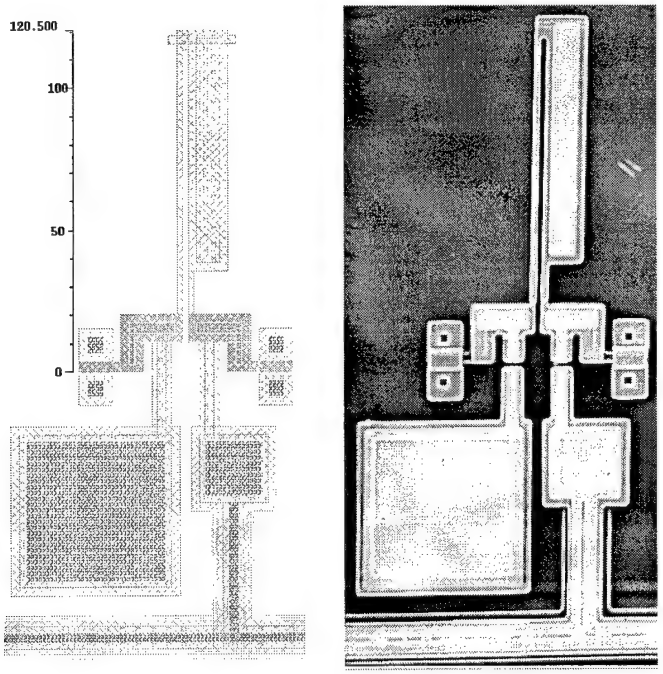

(a) (b)

Figure 3-1: Example of (a) a CAD drawing of a microstructure and (b) a SEM of the same microstructure after fabrication and release. The scale shown in the CAD drawing is in micrometers.

Although the method of drawing a microstructure is straightforward and simple, the actual design of the microstructure is not so straightforward. When drawing a microstructure, the designer must keep in mind the many available structural layers and connecting layers that can be utilized to create a microstructure. Also, the designer must be aware of the actual fabrication process used to create the final product. If the designer is not careful, serious flaws in the fabricated design may result. Design errors can result in much wasted time and effort, especially since the fabrication process takes two months to complete. The above concerns are embodied in the design rules that are specific to the fabrication process used, which will be discussed next.

3.2 Fabrication of a Microstructure

The MEMS used in this research are limited to be fabricated entirely from polycrystalline silicon (polysilicon). The commercial surface micromachining fabrication process used by AFIT is the Multi-User MEMS Process (MUMPs) by MCNC [2]. There are three polysilicon layers available for constructing microstructures. Two of the layers are releasable and the third can only be patterned on the substrate. MUMPS leaves the finished polysilicon microstructures encased in phosphosilicate glass (PSG), also known as sacrificial layers. The sacrificial layers can be removed which "releases" the polysilicon microstructures, leaving them free to move on the face of the die, if so designed. The "release" process will be discussed in Section 3.3.

The MUMPS process begins with 100 mm diameter, 500-550 μm thick, n-type, (100) oriented silicon wafers. The wafers are heavily doped with phosphorus (POC13) in a standard diffusion furnace to a resistivity of 1-2 ohm-cm. Next, a 0.6 μm thick layer of silicon nitride (nitride) is deposited on the surface of the wafer using low pressure chemical vapor deposition (LPCVD). The silicon nitride layer is used to electrically isolate the surface of the wafer. The nitride layer is followed immediately by the deposition of a 0.5 μm thick layer of polysilicon (poly0) using LPCVD. The poly0 is then patterned using photolithography. The photolithography process entails coating the wafer with positive photoresist, exposing the wafer with UV-light through the appropriate mask, developing the resist which removes the exposed resist, reactive ion etching (RIE) of the exposed polysilicon, and removal of the remaining resist.

After patterning the poly0 layer, a 2.0 μm thick layer of PSG (oxide1) is deposited using LPCVD. The oxide1 layer is then patterned by photolithography using the "dimples" mask. The RIE for this step etches 0.75 μm into the oxide1 layer. The oxide1 layer is again patterned by photolithography using the "anchor1" mask. The RIE for this step etches through the oxide1 layer, and stops at poly0 or nitride. The anchor1 patterns allow the "poly1" layer to be deposited or anchored onto the substrate.

Next, the second layer of polysilicon (poly1) is deposited using LPCVD to a thickness of 2.0 μm. A 0.2 μm layer of PSG is deposited over poly1, and the wafer is annealed at 1050° C for 1 hour to dope the polysilicon layers with phosphorous. The PSG acts as the dopant source. The PSG is then patterned using photolithography. The

patterned PSG in turn becomes a mask for poly1, which is etched using RIE. The remaining PSG mask is then removed by RIE.

After patterning poly1, a second 0.75 μm thick PSG layer (oxide2) is deposited using LPCVD. The oxide2 layer is then patterned using the "poly1poly2via" mask and patterned again using the "anchor2" mask. The poly1poly2via patterns are etched only through oxide2, which, are meant to provide mechanical and electrical contact between poly1 and the third polysilicon layer. The anchor2 patterns are etched through oxide1 and oxide2, and are meant to provide mechanical and electrical contact between the third polysilicon layer and poly0 or nitride. As a side note, the nitride layer can be removed by combining an anchor1 and poly1poly2via etch, or an anchor1 and anchor2 etch directly over top of each other. The conductive substrate can be utilized as an electrical contact by removing the nitride layer.

The third, 1.5 μm thick, polysilicon layer (poly2) is deposited followed by a 0.2 μm PSG layer using LPCVD. The wafer is annealed at 1050° C for 1 hour to dope the polysilicon layers. Next, the PSG layer is patterned using photolithography. The patterned PSG in turn becomes a mask for poly2, which is etched using RIE. The remaining PSG mask is then removed by RIE.

Finally, a 0.5 μm thick gold layer with a 0.02 μm thick chromium adhesion layer is deposited and patterned using the lift-off method. Figure 3-2, is a drawing of the different layers used in the MUMPs process. The drawing shows the relative thicknesses and layer names. Note, the names used to describe the different MUMPs layers and etch

masks will be used again throughout this document when describing the micromachines used in this research.

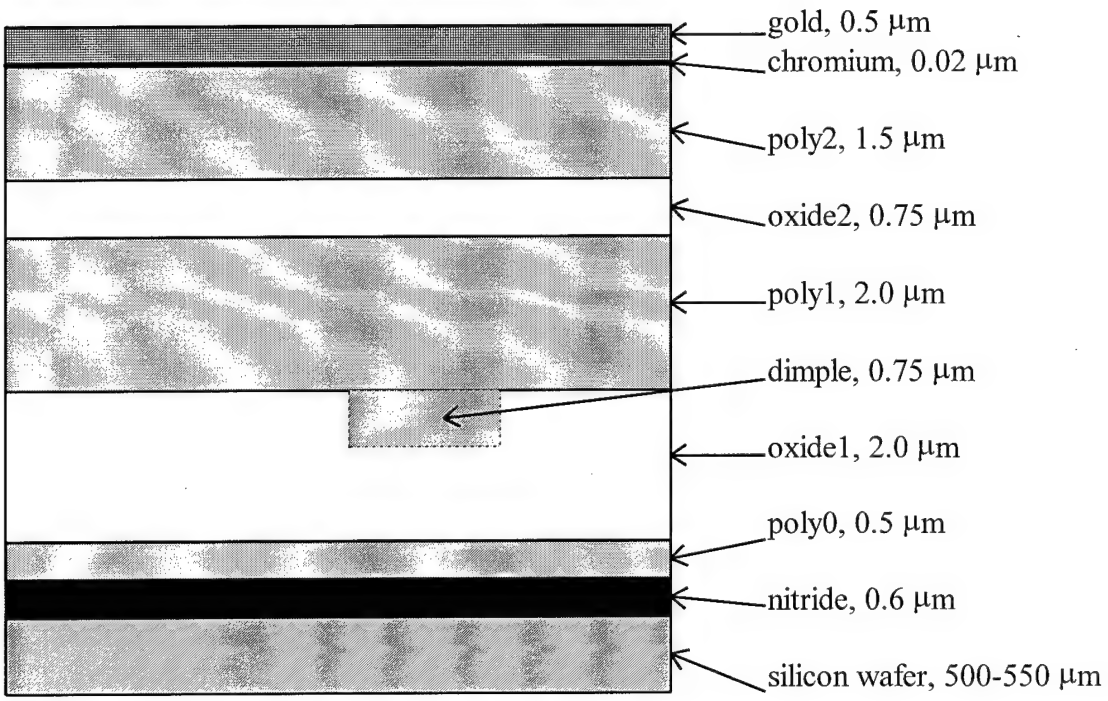

Figure 3-2: Drawing of the different layers used in the MUMPs process. The drawing shows the relative thicknesses and layer names.

The MUMPs process guarantees a minimum feature widths and feature spacings of 2 μm. Smaller feature widths and feature spacings can be achieved, but may not be reliable from one fabrication run to another. Figure 3-3 shows a process gauge fabricated on the MUMPs 18 run illustrating achievable feature widths and spacings with the three polysilicon layers. The guaranteed 2 μm width and spacing is marked, the remaining spacings and widths decrease in increments of 0.25 μm. From Figure 3-3 it can be seen

that a 1.5 μm feature spacing is achieved for all three layers, and a 0.5 μm feature width is achieved for all layers except poly0.

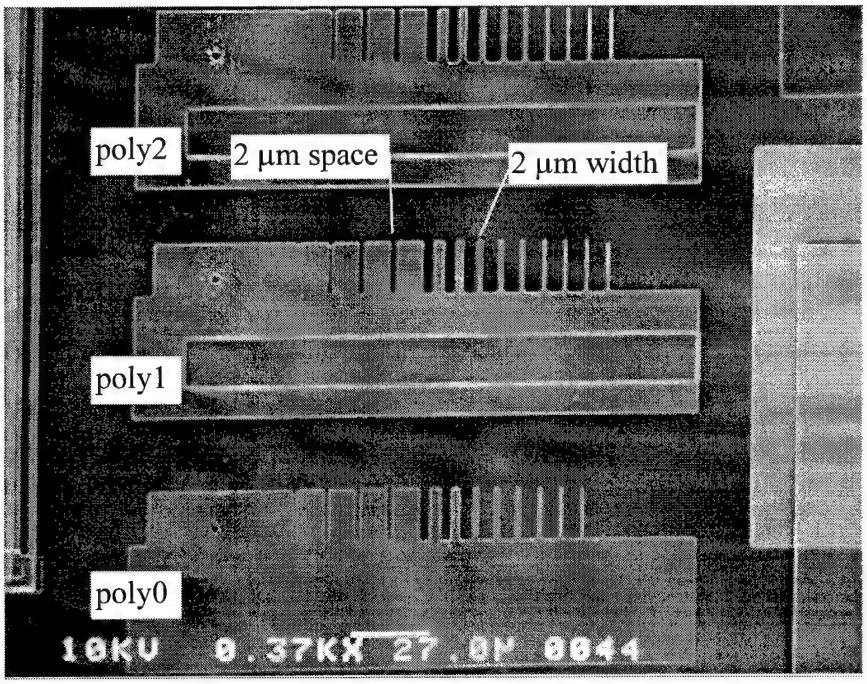

Figure 3-3: Scanning electron micrograph of a process gauge fabricated on the MUMPs 18 run showing achievable feature widths and spacings.

Figure 3-4 shows a comparison between the CADENCE drawing of a hinge to the actual hinge after fabrication. The CADENCE drawing distinguishes the different structural layers and mask layers using color. With reference to the fabricated hinge, the space between the nitride and poly2 hinge cap is where the oxide1 and oxide2 layers were situated before releasing. The space between the poly1 hinge pin and the poly2 hinge cap was formed by the oxide2 layer, which has also been removed by the release process. The release process is discussed next.

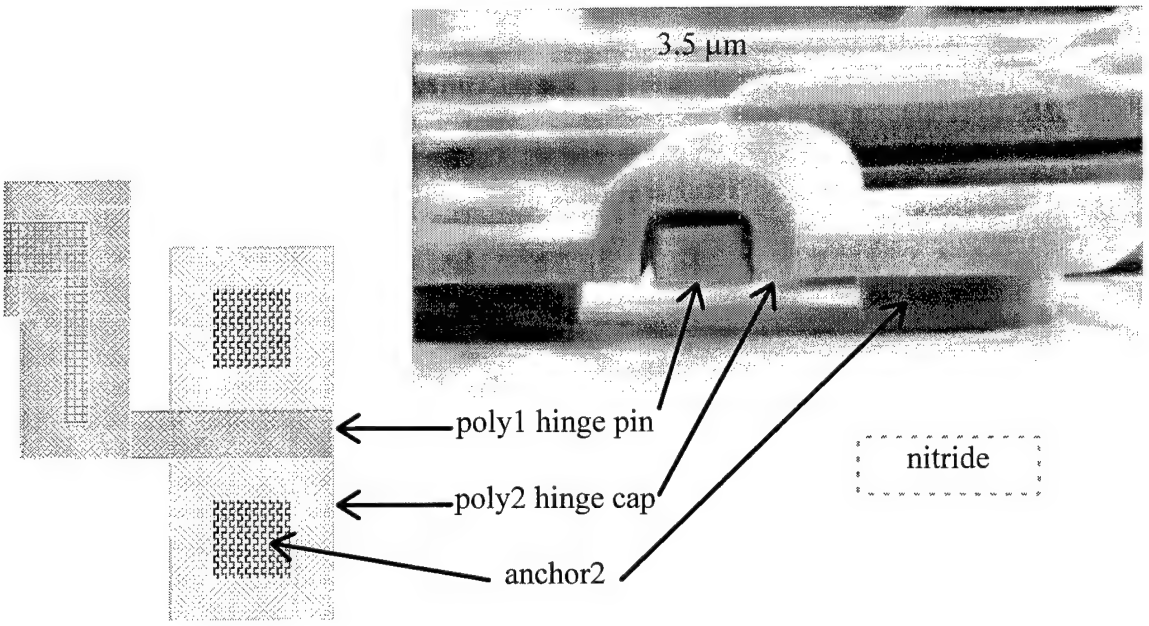

Figure 3-4: Comparison of the CADENCE drawing of a hinge to the actual hinge after fabrication.

3.3 Release Process of a Microstructure

After the CAD designed micromachines are fabricated using the MUMPs process, fifteen copies of the die (the micromachines are fabricated on a 1 cm x 1 cm die) are delivered to AFIT. The polysilicon microstructures, on each die, are still encased in the PSG from the fabrication process. Also, a coating of photoresist is applied to the surface of each die to help protect it during shipping. This section describes the "release" process, which is the process used to remove the photoresist coating and the PSG.

The release process is performed in an AFIT laboratory under a chemical hood. Caution must be taken when releasing. Some of the chemicals used give off harmful

vapors and can cause severe injury if contact with the skin occurs. A laboratory coat, eye protection, and rubber gloves are worn when releasing. The following are the steps used for releasing one die:

1) Soak die in 50 ml of acetone for 5 minutes. This step removes the bulk of the photoresist, if not all.
2) Soak die in 50 ml of new acetone for 10 minutes. This step ensures complete removal of any traces of photoresist.
3) Soak die in 50 ml of isopropyl alcohol for 5 minutes. This step is used to displace the acetone from the die.
4) Soak die in 50 ml of methanol for 5 minutes. This step is used to displace the isopropyl alcohol from the die.
5) Heat the die on a hot plate at 70° C for 3 minutes. This step is used to completely evaporate the methanol from the surface of the die.
6) Soak die in 49% hydrofluoric acid for 4 minutes. This step is used to etch away the PSG which encases the microstructures on the die.
7) Dip die in 1 liter of deionized water for 3 seconds. This step is used to dilute and displace the hydrofluoric acid to stop etching.
8) Soak die in 50 ml of new isopropyl alcohol for 5 minutes. This step is used to displace the water from the die.
9) Soak die in 50 ml of methanol for 5 minutes. This step is used to displace the isopropyl alcohol from the die.

10) Soak die in 50 ml of new methanol for 10 minutes. This step is used to ensure that the die is cleansed from the other chemicals in the process and dust contamination.

11) Heat the die on a hot plate at 70° C for 3 minutes. This step is used to completely evaporate the methanol from the surface of the die.

12) Store die in a clean, dry, and air-tight container. The microstructures are now released and ready for testing.

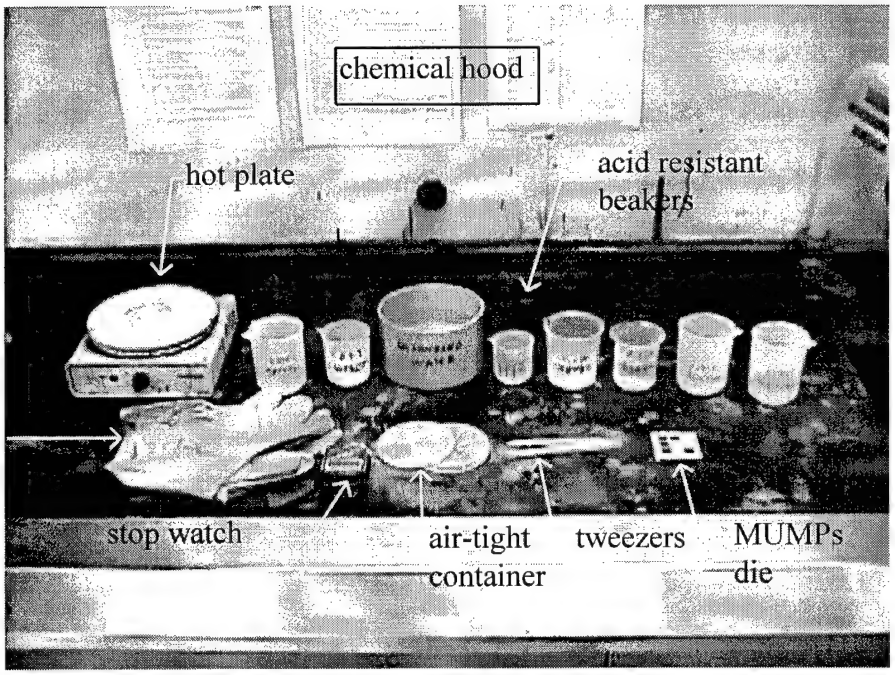

Figure 3-5: Photograph of the setup typically used during the release process.

Figure 3-5 shows a photograph of the setup typically used during the release process. All of the chemicals used during the process are contained in acid resistant

beakers. The die is transported, during the process, using acid resistant tweezers. Care must be taken to not contaminate the die with oils or particulates by contact with the skin. When not testing, the die should be stored in a dry place or contamination from moisture may affect the performance of the microstructures.

3.4 References

[1] CADENCE version 9502, Cadence Design Systems Inc., 555 River Oaks Parkway, San Jose, CA 95134.

[2] D. Koester, R. Mahadevan, and K. Markus, "SmartMUMPs design handbook including MUMPs introduction and design rules," rev. 4, DARPA project (DABT 63-93-C-0051) of MEMS Technology Applications Center MCNC, 3021 Cornwallis Road, Research Triangle Park, NC 27709, 1996.

4. Experimental Setup

This chapter describes the equipment used to test the MEMS in this research. Section 4.1 describes the equipment used to manipulate and electrically characterize microstructures. Section 4.2 describes the equipment used to obtain images of MEMS. Section 4.3 discusses the equipment used to perform minor post-processing on the MUMPs die, and Section 4.4 describes the system used to test the microrobot.

4.1 Manipulation and Characterization of MEMS

For this research, all manipulation and electrical characterization of microstructures is performed on a probe station using probes. Figure 4-1 shows a photograph of the probe station with probes, setting on a vibration isolation table. Figure 4-2 shows a drawing of the probe station only, with its components labeled. The probe station is a Model 6200 Analytical Probe Station from The Micromanipulator Company, Inc. The probe station is operated on a vibration isolation table. Microstructures can be viewed through 2.25× (0.04 N.A.), 8× (0.15 N.A.), 25× (0.31 N.A.), or 50× (0.45 N.A.) objectives.

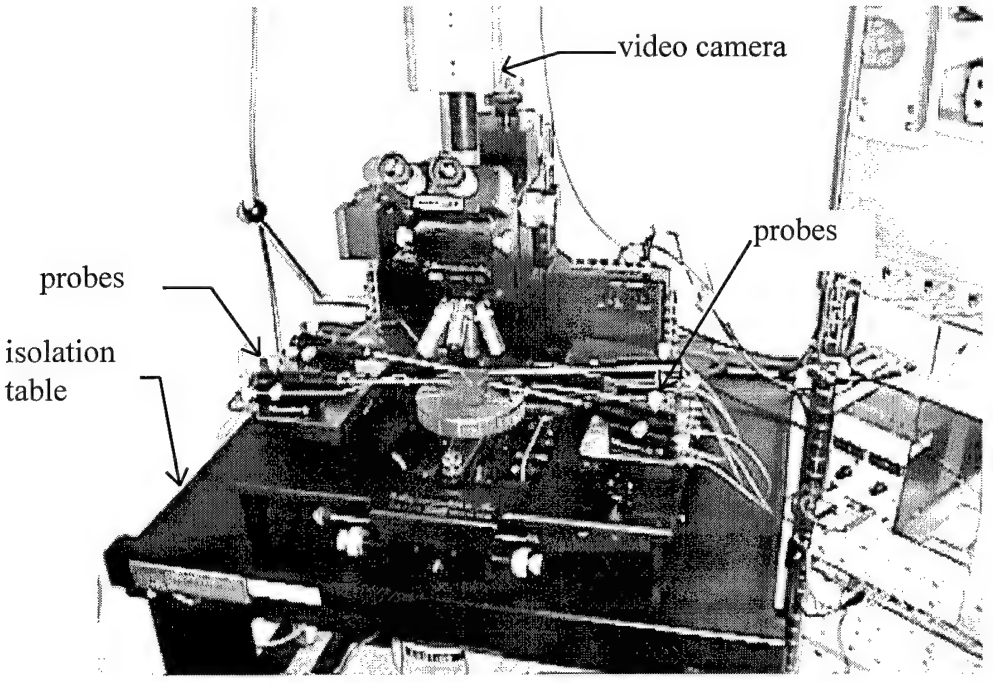

Figure 4-1: Photograph of Micromanipulator Analytical Probe Station with probes and vibration isolation table.

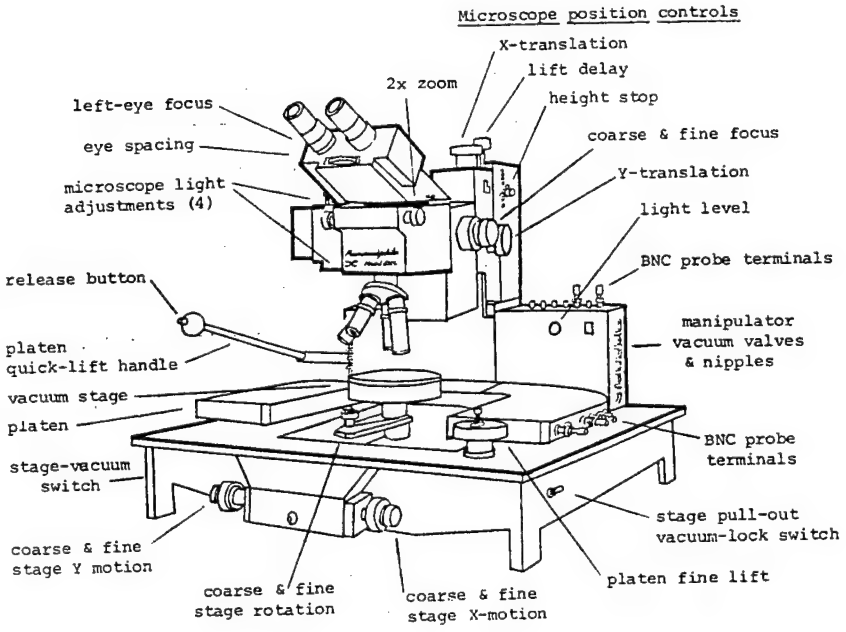

Figure 4-2: Drawing of Micromanipulator Analytical Probe Station. Drawing taken from instruction manual.

With a MUMPs die positioned on the center of the vacuum stage, microstructures are manipulated using four probes that are positioned from the platen and are held in place by vacuum. Microsystems are supplied electricity, and resistance readings are measured, through the probes. The probes can be connected to power supplies and measurement equipment, which, will be described later. For electrical supply and measurements, Micromanipulator Model 7B tungsten probe needles, with a 0.5 mm tip and 0.02 inch shank, are used. For manipulation, more fine Model 7F nickel probe needles, with a 0.5 mm tip and 0.001 inch shank, are used.

The probes can be connected to a variety of power supplies and test equipment. For this research, all voltage and resistance measurements were taken using a Fluke 77/BN Multimeter. All current measurements were taken with a Fluke 8600A Digital Multimeter. The low voltage power supply used is a HP 6236B Triple Output Power Supply, that can provide 0 - 6 V with a current limit of 2.5 A or 0 - ±20 V with a current limit of 0.5 A. The high voltage power supply used is a Kikusui Electronics Model PAD 160-1L regulated D. C. power supply that can provide 0 - 160 V with a current limit of 1 A. For pulsed input signals, a three channel sequencer is used. The three channel sequencer is powered by 5 V, an internal clock runs switches three relays that can be connected to the power supplies discussed above. The operation of the three channel sequencer is described in detail by Comtois [1]. Figure 4-3 shows a photograph of the test equipment described above.

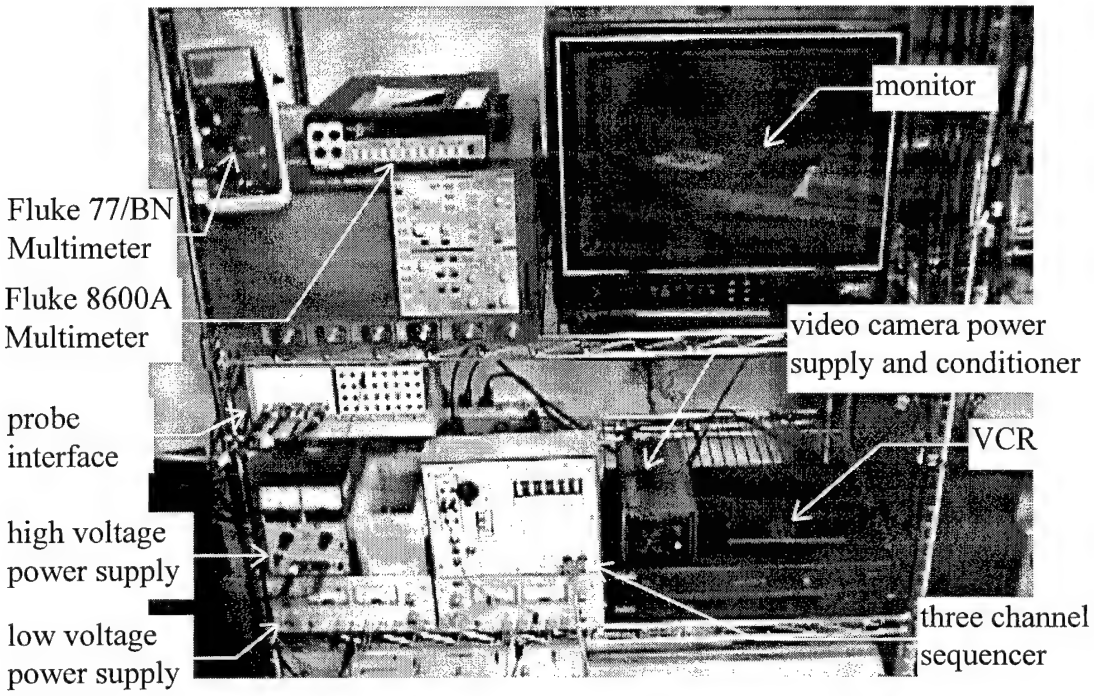

Figure 4-3: Photograph of test equipment used with the probe station.

4.2 Image Recording and Photography

Video recordings of microstructures were taken through a Sanyo VCC 3700 Color CCTV video camera (shown in Figure 4-2) mounted near the eyepieces of the analytical probe station, and connected to a VCR (shown in Figure 4-3). All still video images presented in this thesis were captured on an Alessi REL-5500 probe station using Cascade Microtech Prober Software through a Panasonic GP-KR222 video camera connected to a video capture card. The captured images are stored as bitmaps.

All scanning electron micrographs presented from this research, were taken on an International Scientific Instruments WB-6 Scanning Electron Microscope (SEM). The

film used is Polaroid, black and white, Type 55, Positive-Negative, 4x5 Instant Sheet Film. The SEM, shown in Figure 4-4, was operated using a 200 micron aperture with a gun potential of 10 kV, emission current of 90 μA, medium working distance, and a photo speed of 2.

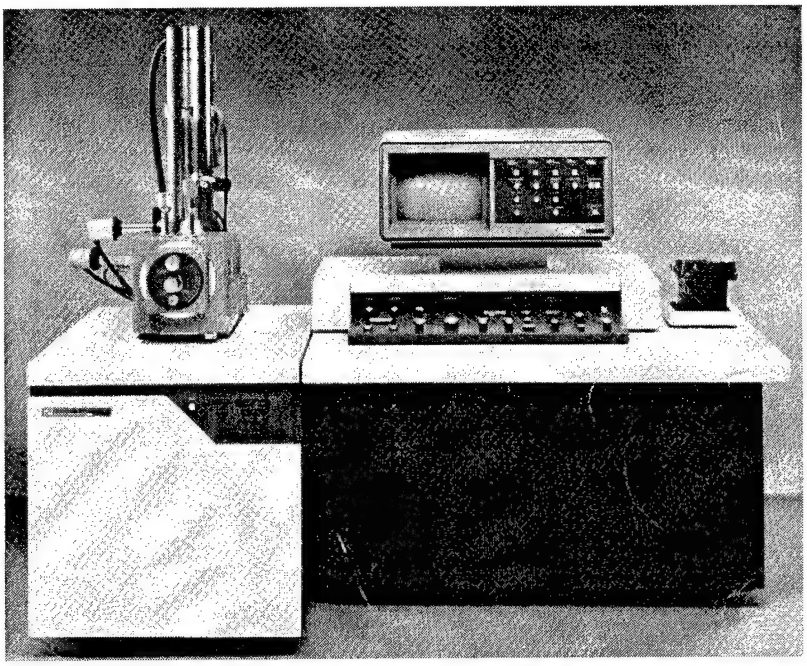

Figure 4-4: Photograph of scanning electron microscope used in this research.

4.3 Post-processing of MUMPs Die

The weight of MUMPs die and other related samples were measured in this research. All mass measurements presented in this thesis were measured using a Mettler Toledo Electronic Scale, model no. AG245. The accuracy of the scale is ± 0.01 mg.

All wirebonding was performed on a Kulicke and Soffa Industries, Model 4124, Universal Thermosonic Gold Ball Bonder using 0.001 inch diameter gold wire. The settings for the bonder are as follows for the ball and wedge bonds respectively: force, 4.0 and 4.0; time, 5.4 and 6.0; power, 3.4 and 5.8. The loop and search heights were adjusted as needed for the specific situation. The bonder is shown below in Figure 4-5.

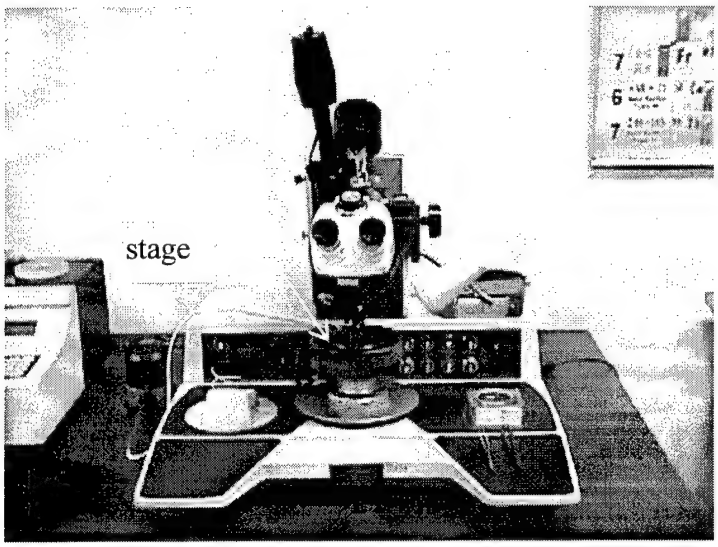

Figure 4-5: Photograph of Thermosonic Gold Ball Bonder.

During this research, the need for modifying MEMS designs after fabrication arose. A laser cutter provided an elegant way for modification. The laser cutter was used to correct design errors and to modify microstructures to enhance experiments. Figure 4-6 shows a drawing of the laser cutter mounted to the Micromanipulator probe station described in Section 4.1.

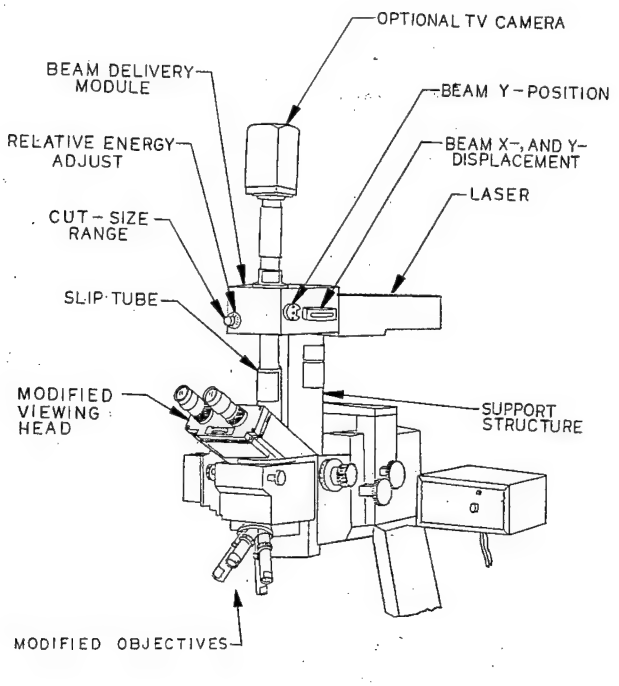

Figure 4-6: Drawing of laser cutter used in this research. Drawing taken from instruction manual.

The laser cutter is a Micromanipulator Model LAS-2001 Class I Laser Cutter. The laser has a wavelength of 532 nm (green), and the energy on target can be varied from 10^{-8} J to 10^{-4} J. The cut hole can be varied from approximately 1 μm to 14 μm in diameter, using a 50×/.45 N.A. objective, by varying the cut-size adjustment and the microscope zoom. In general, the cut hole diameter and depth can be varied by varying the output energy, cut-size adjustment, use or non-use of filter, objective, zoom, and focus. Figure 4-7 shows an example of where the laser cutter was used to sever a gold on poly2 wire. Note, the nitride, below the wire, was also damaged by the laser blast.

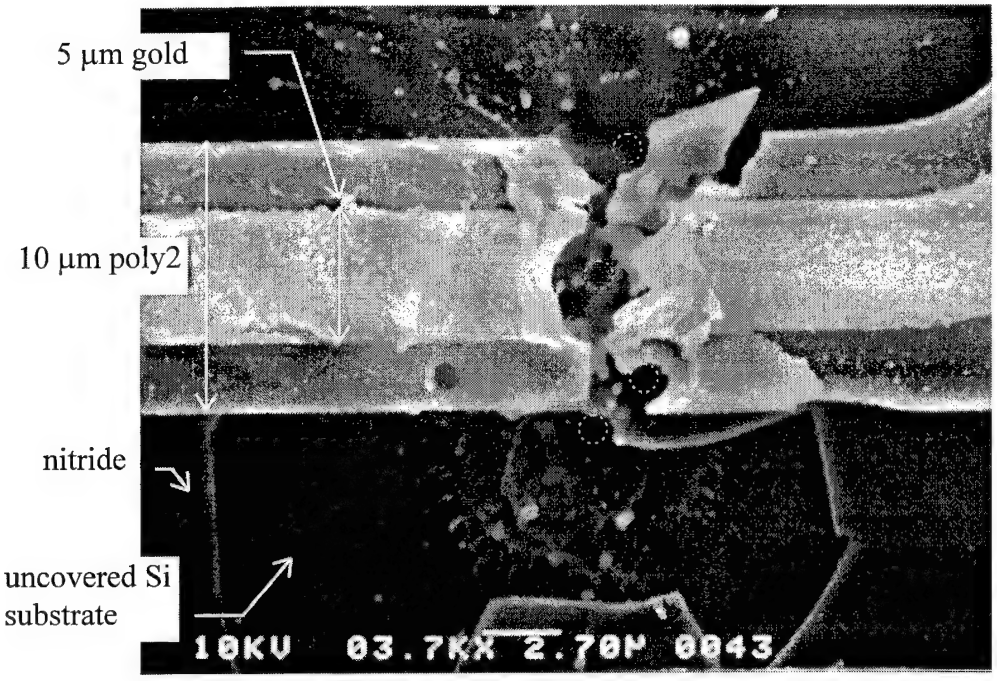

Figure 4-7: Scanning electron micrograph showing a gold on poly2 wire that was severed using the laser cutter.

In the experiment of Figure 4-7, the laser cutter and microscope had the following settings: 100% (10^{-4} J) energy, cut-size set to "small", no filter, 0.5 N.A., 1:1 zoom, and in focus on the gold layer. The wire was severed using four laser cuts. The laser spot was approximately 1-2 μm in diameter, however, the resulting damage has a greater area, as can be seen from Figure 4-7. Figure 4-7 also shows four drawn circles that mark the approximate locations where each laser spot hit.

Some of the experiments in this research required mechanical lapping of the back of the MUMPs die. The die were lapped dry using 320 grit cabinet paper with a Buehler Minimet 1000 Grinder/Polisher, set at 5 lbs pressure and 50 rpm. The following steps were taken to lap a die:

1) Heat the grinder/polisher specimen mount on a hot plate to 97° C.
2) Apply a circular dab of Crystal Bond thermal adhesive to the center of the specimen mount, leaving the specimen mount on the hot plate. The dab must be wide enough to encompass the 1 cm square MUMPs die.
3) Set one unreleased MUMPs die, micromachined face down, onto the dab of thermal adhesive, ensuring the die is in the center of the specimen mount. Leaving the specimen mount on the hot plate for 5 minutes, let gravity settle the die into the thermal adhesive.
4) Remove the specimen mount from the hot plate and let cool to room temperature. Remove excess thermal adhesive from the specimen mount using cotton swabs and acetone. Leave a build-up of thermal adhesive around the edges of the die to help protect the edges of the die from chipping or abrasion during the lapping process.
5) Measure the thickness of the die and specimen mount with a micrometer at several locations on the die.
6) Install the specimen mount onto the grinder/polisher arm and begin lapping.
7) During the lapping, periodically check the thickness of the die with a micrometer, until the desired thickness is reached.
8) Remove specimen mount from the grinder polisher arm, and heat on the hotplate to 97° C. Pick up the die using tweezers. The die can now be released using the same release process described in Chapter 3.

4.4 Microrobot Test Setup

The microrobot will be described in detail in Chapter 5, however, a brief description should be given at this point to assist in understanding the purpose of the test equipment to be described. The microrobot is actually a 1 cm by 1 cm by 550 μm silicon chip with 230 μm long, surface micromachined legs protruding from one side. The other side of the chip has no microstructures on it. The microrobot legs are powered through three attached gold bondwires by the low voltage power supply through the three channel sequencer.

Figure 4-8 shows a photograph of the microrobot test setup.

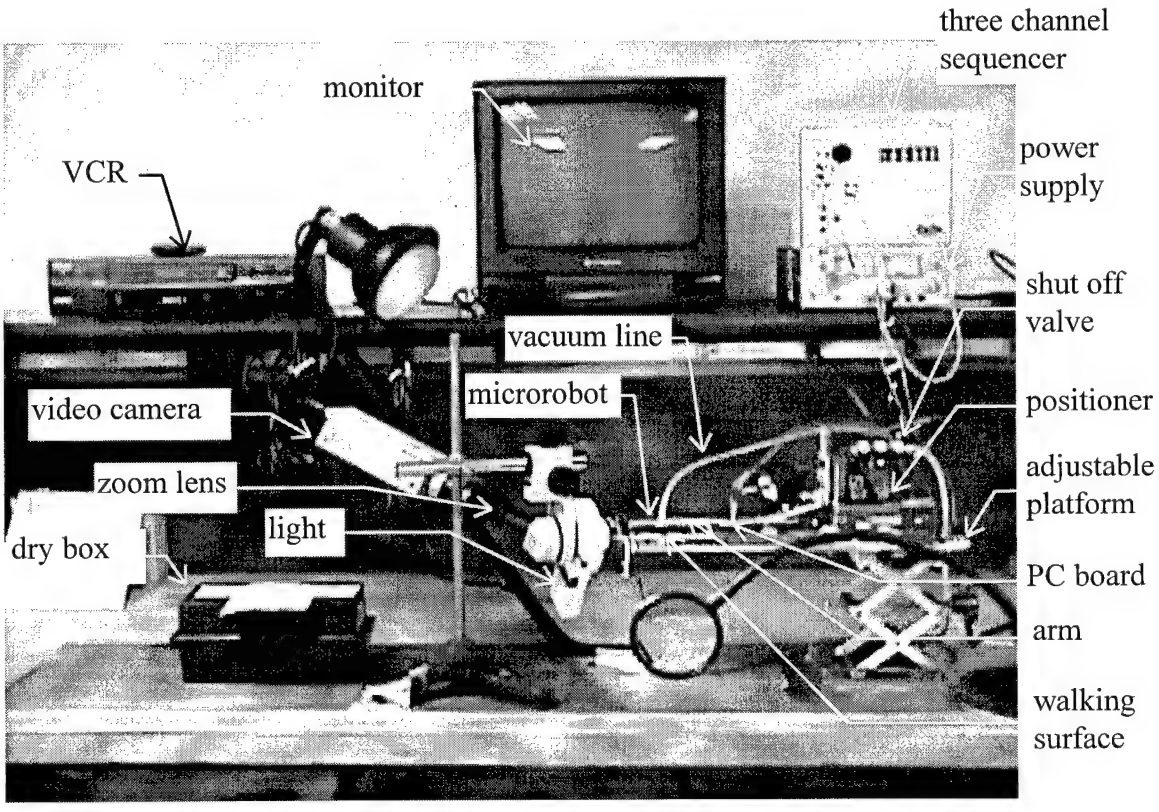

Figure 4-8: Photograph of microrobot test setup.

A special test setup, designed by the author, was used in the testing of the microrobot. The special setup is meant to provide a precise means of release onto the walking surface, retrieval from the walking surface, and capturing video footage of the walking experiment.

Figure 4-9 shows a simplified drawing of the microrobot test setup. The microrobot is connected to the end of an aluminum arm by mechanical hold down devices or by vacuum. The microrobot can be released by turning off the vacuum at the valve. The microrobot chip is wire bonded to a small printed circuit (PC) board five inches away on the arm. The PC board provides an attachment point for the output of the three channel sequencer.

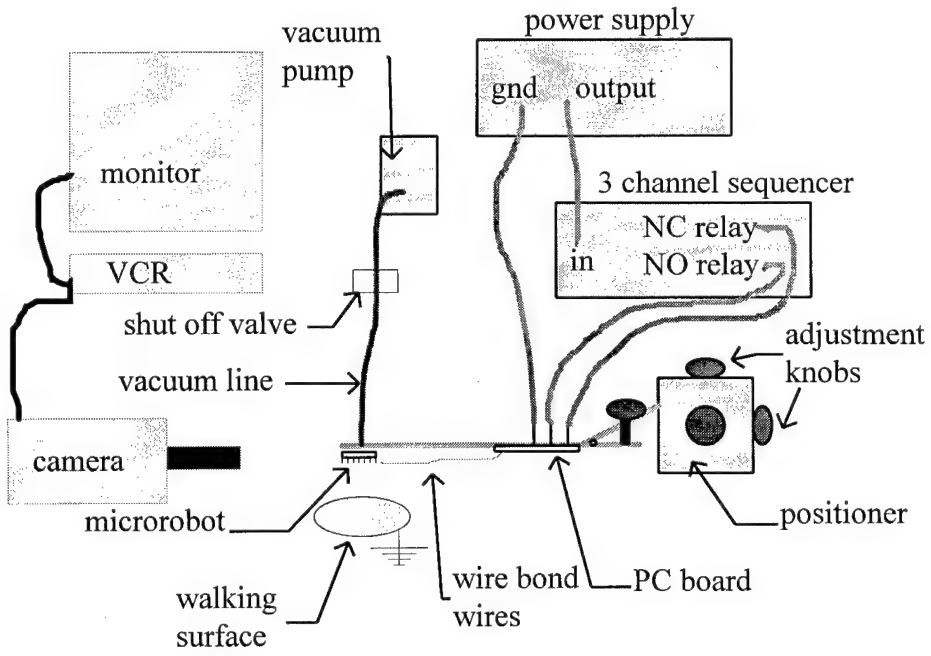

Figure 4-9: Simplified drawing of microrobot test setup.

The arm is attached to a fine motion positioner, essentially a probe positioner. Figure 4-10 shows a closer view of the microrobot positioner. A video camera with a 15× - 50× zoom lens is focused to where the microrobot will contact the walking surface.

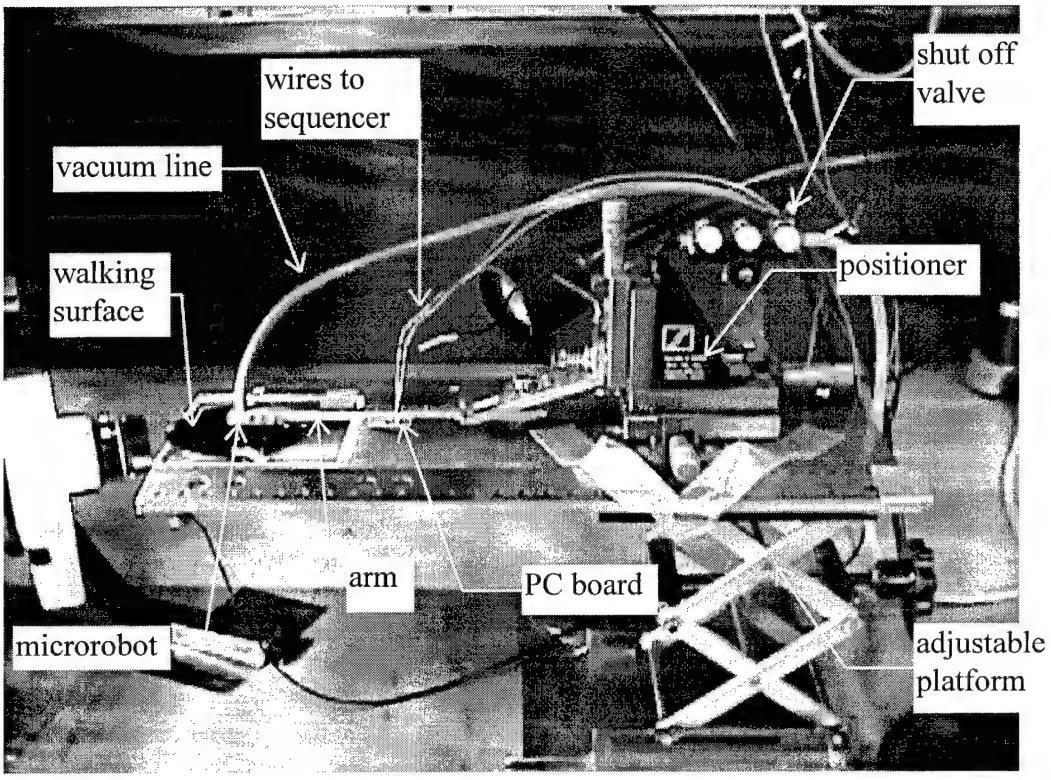

Figure 4-10: Photograph of microrobot positioner.

The position where the robot legs contact the walking surface can be seen on the monitor, so the microrobot can be released without damage to the legs by dropping or crushing. The walking surface is a three inch silicon wafer coated with approximately 11 μm of polyimide. The wafer is used for its flatness, and the polyimide is used to electrically passivate the walking surface. Also, the silicon wafer is grounded with

respect to the microrobot's power supply to help eliminate electrostatic forces between the microrobot and walking surface. The three channel sequencer is supplied by the low voltage power supply. One circuit of the microrobot's legs is supplied by the output of a normally closed (NC) relay, and the other circuit is supplied by the output of a normally open (NO) relay. Supplying power to the microrobot's legs in this fashion allows one leg circuit to operate on one half of a cycle, and the other leg circuit on the other half of the cycle. A dry box is used as a low moisture place to store the microrobot when not in use. Silica gel is used to keep the box dry. Figure 4-11 shows an even closer view of the microrobot positioning arm and the microrobot.

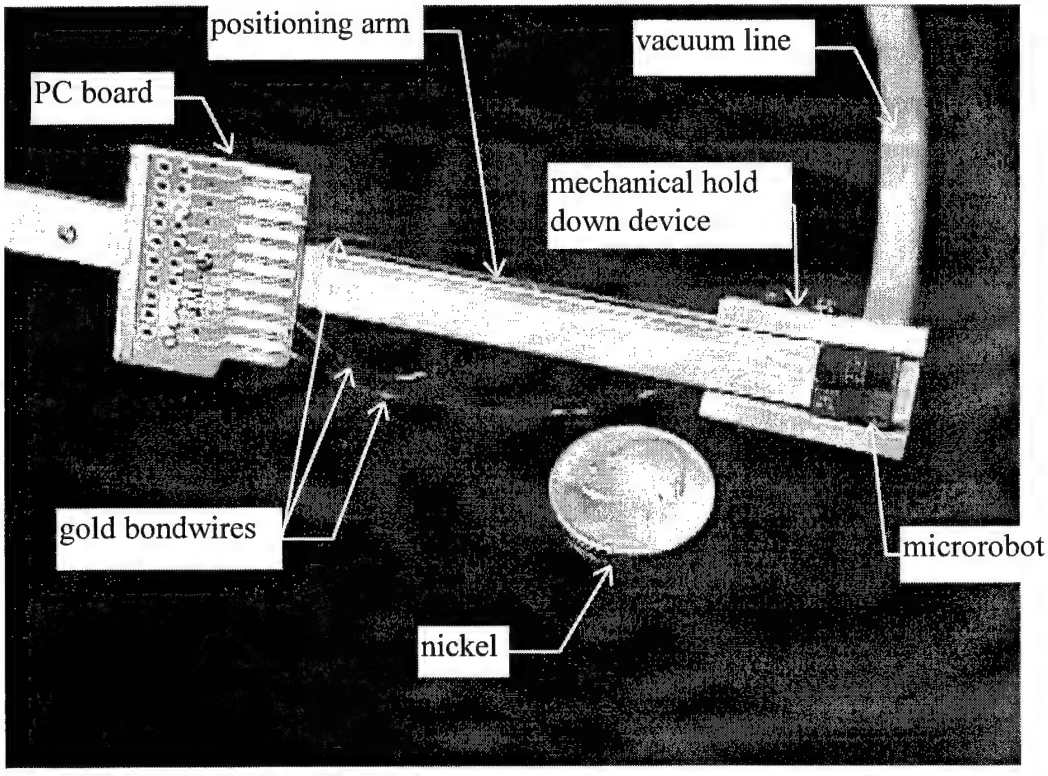

Figure 4-11: Photograph of microrobot positioning arm and microrobot along side of a nickel for size perspective.

4.5 References

[1] J. Comtois, *Structures and techniques for implementing and packaging complex, large scale microelectromechanical systems using foundry fabrication processes.* Doctoral Dissertation, Air Force Institute of Technology, Wright-Patterson AFB, Ohio, AFIT/DS/ENG/96-04, 12 May 1996.

5. Theory, Design, and Results

This chapter presents the theory and design behind, and the results of this thesis research. For convenience, the thesis research goals, from Chapter 1, are repeated here.

1) Erect microstructures, originally in their parallel to the substrate post fabrication position, to a position normal to the substrate, using self assembly techniques.
2) Provide electrical power to erected structures by means of practical low resistance electrical connections.
3) Realize circular motion normal to the substrate.
4) Realize a microrobot that can move on a flat surface.

With reference to the above goals, Sections 5.1 - 5.4 will cover the theory, design, and results pertaining to Goals 1 - 4, respectively.

5.1 Erecting Microstructures Normal to the Substrate

This section presents the theory, design, and results pertaining to Research Goal 1: erect microstructures normal to the substrate, using self assembly techniques. The designs in this section will be presented in chronological order with reference to the different MUMPs fabrication runs. Also, when describing a design, the terminology

specific to the MUMPs fabrication process may be used. The MUMPs process is described in Chapter 3.

Designs Pertaining to the MUMPs 18 Fabrication Run

Figure 5-1 shows a scanning electron micrograph of a first prototype self assembly system from the MUMPs 18 fabrication run. With reference to Figure 5-1, the purpose of this system is to erect the "leg" to a perpendicular position with respect to the substrate, and then be able to actuate the leg. All of the prototype microsystems presented from this research, except for those pertaining to circular motion, have been designed with the intended function of being a microrobot leg system. For this reason, the names and functions of the various components of different prototypes, presented in this section and the following sections, will be the same.

With reference to the leg, labeled in Figure 5-1, the leg is actually a horizontally deflecting thermal actuator, and its operation is described in detail in Chapter 2. The horizontally deflecting thermal actuator is given the name "leg" because this component will eventually be utilized as a leg for the microrobot presented in Section 5.4. Each flexure of the leg is attached to, or part of, the corner of a square support structure. The two electrically isolated, and physically separate, square support structures are, together, named the "base". Each square support structure, or each side of the base, is anchored, to the nitride, through hinges. The base can pivot at the hinges.

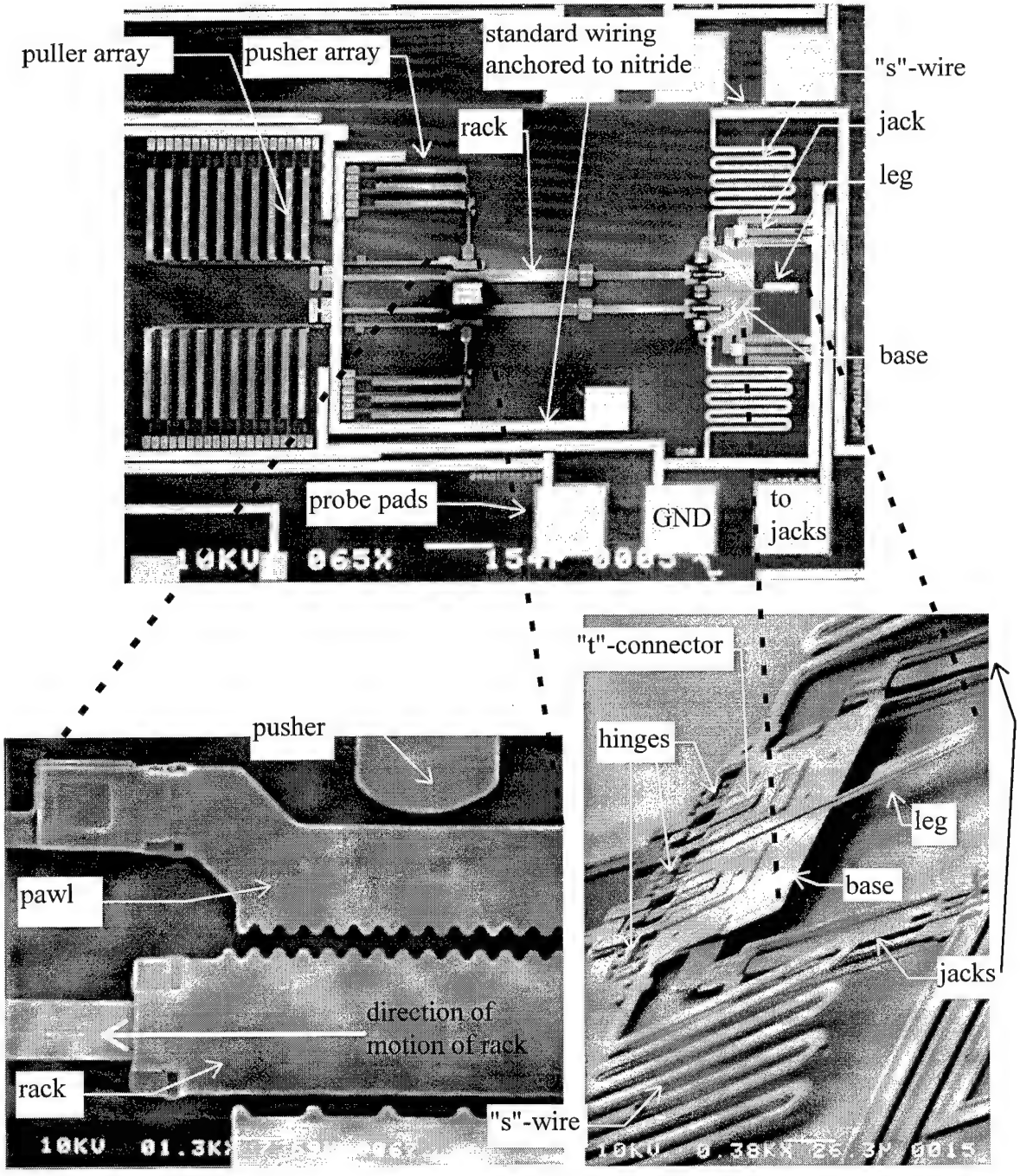

Figure 5-1: Scanning electron micrograph of first prototype self assembly system from the MUMPs 18 fabrication run. The figure shows a closer view of the rack and pawl. Also shown is a closer view of the "s"-wires and partially raised base and leg.

Connected to either side of the base, near the hinges, are "s"-wires. These gold on poly2 structures are free from the substrate, and connected, at the other end, to standard wiring anchored to the nitride. The s-wires are so named for their "s" shaped curves. The purpose of the s-wires is to supply electricity to the leg through each side of the base, while being able to flex and twist. Although each side of the base is fabricated from conductive polysilicon, a gold path is provided from the points where the spring wires meet the base to the point where each flexure of the leg connects to the base. The reason for this is because the gold will provide a lower resistance path for current relative to the path through the polysilicon.

Underneath, and on either side of, the base are "jacks". The jacks are actually vertically deflecting thermal actuators, and their operation is described in Chapter 2. The vertically deflecting thermal actuators are named jacks because, after being back-bent, they curl up and raise the base. The close up of the base, in Figure 5-1, shows the partially raised base, and the back-bent jacks.

Connected to the center of each side of the base, through "t"-connectors, are "racks". The intended purpose of the racks is to further raise the base to a normal to the substrate position, after the jacks have given the base an initial lift. The rack, itself, is pulled back by an arrangement of horizontally deflecting thermal actuators, called a linear motor. The linear motor used in this design is the same motor described, in Chapter 2, used by Reid, et. al., in their self assembly system [1]. A brief description of the operation of the linear motor is as follows. With reference to Figure 5-1, the "pusher array" is back-bent so that the "pusher" is pushing the "pawl" against the rack when

unactuated. With the pawl against the rack, where the teeth of the pawl and the teeth of the rack are interlocked, the pawl can be pulled by the connected "puller array", consequently pulling the rack also. Next, the pusher array is actuated, disengaging the pawl from the rack, and the puller array is unactuated allowing the pawl to return to its initial position, ready to be pushed against the rack and pull again.

All of the components of this prototype self assembly system can be operated electrically through gold on poly2 on poly0 standard wiring anchored to the nitride. The standard wiring is connected to probe pads, made from gold on poly2 on poly0. The probe pads are supplied with electricity through probes at a probe station as described in Chapter 4.

Results Pertaining to the MUMPs 18 Fabrication Run

Several trials of attempting to assemble the system and variants of the system described above were performed at a probe station. The jacks were able to lift the base as intended. The bases were lifted or pivoted about their hinges to angles of typically 7.2°, 8.6°, 13° for the different s-wire designs in Figure 5-2 (a), Figure 5-3 (a), and Figure 5-1, respectively. To backbend the jacks, 7.25 V was applied between the "GND" and "jacks" probe pads (see Figure 5-1) for 3 seconds. The current consumption of the jacks was 23 mA, at this voltage.

Although the jack part of this self assembly system was successful, the linear motor part was not. During several attempts to further lift the base with the linear

motors, no further lifting of the base was observed. The pawls were observed grabbing the racks and the t-connectors were observed vibrating while the motor was running. It is suspected that the resistive torque of the s-wires on the base was too great for the linear motors to overcome.

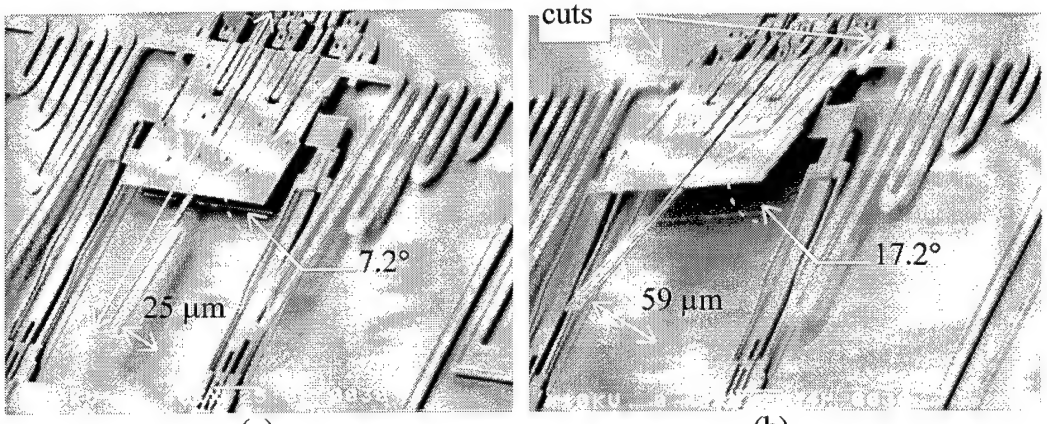

(a) (b)

Figure 5-2: Scanning electron micrographs of the leg and base after being raised by the jacks. The s-wires have been severed from the base, using a laser cutter, in (b).

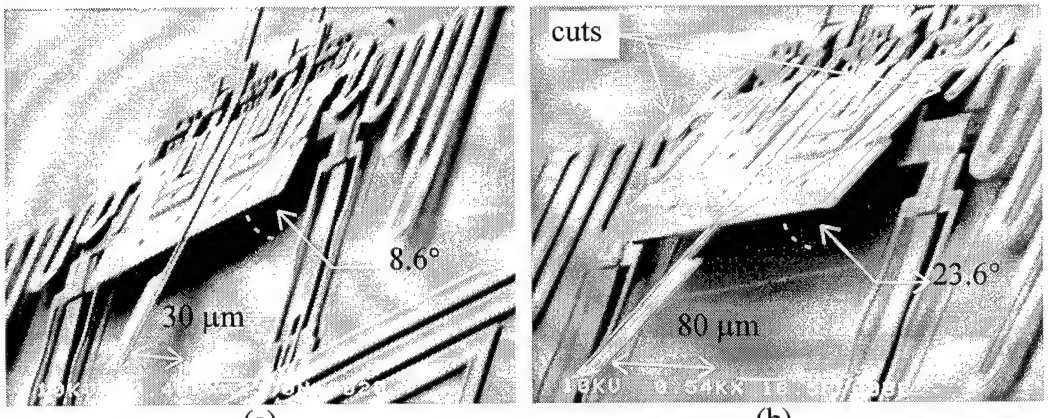

(a) (b)

Figure 5-3: Scanning electron micrographs of the leg and base, using a different s-wire design, after being raised by the jacks. The s-wires have been severed from the base, using a laser cutter, in (b).

Figure 5-2 (b) and Figure 5-3 (b) show the raised leg and base after the s-wires have been severed, from the base, using the laser cutter discussed in Chapter 4. This was done to determine if the jacks were being held back from a full deflection by the resisting torque of the spring wires. The wires were cut after the MUMPs 18 die was fully released. It was found that the jacks were able to deflect more after the wires were cut. For example, the bases were pivoted about their hinges to angles of 17.2° and 23.6° in Figure 5-2 (b) and Figure 5-3 (b), respectively.

Figure 5-4 is a scanning electron micrograph of a more compact self assembly system prototype. Most of the components of this system are the same as the design discussed above.

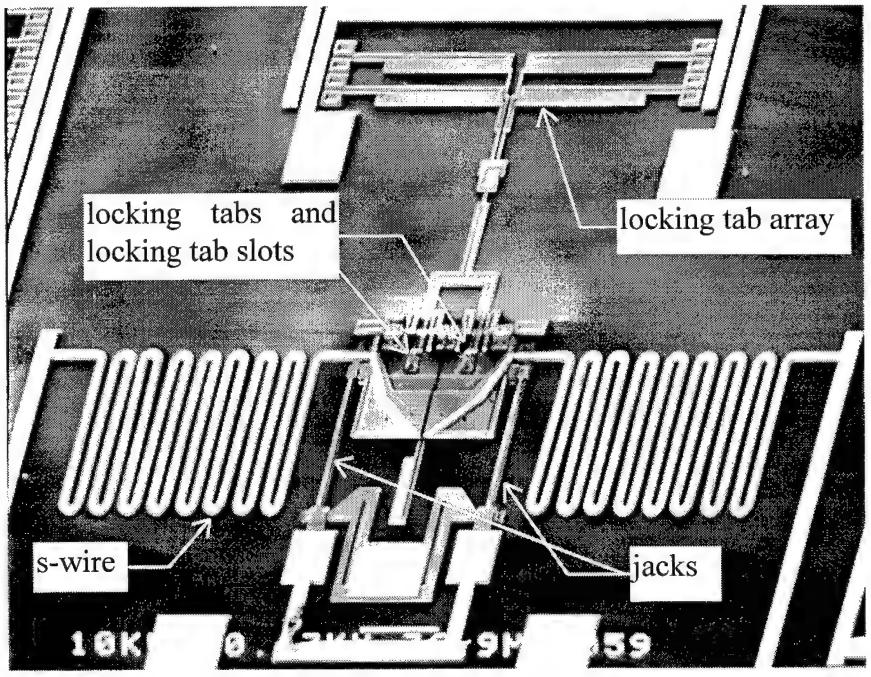

Figure 5-4: Scanning electron micrograph of a more compact self assembly system prototype.

The only difference in design is an array of horizontally deflecting thermal actuators, or "locking tab array", connected to "locking tabs", instead of a linear motor and rack system. The intended operation is as follows. The jacks lift the base part way. Next, the locking tab array flexes forward, inserting locking tabs into locking tab slots in the base. The locking tab array is then back-bent, pulling the base and leg into an upright position.

The jacks were able to pivot the base, however the locking tab array could not flex far enough to lock the locking tabs in the locking tab slots. Figure 5-5 shows the leg and base lifted by the jacks. Figure 5-6 shows the leg and base after being locked into the locking tabs by lifting the base with probes. Also shown is a close up view of a locking tab and locking tab slot.

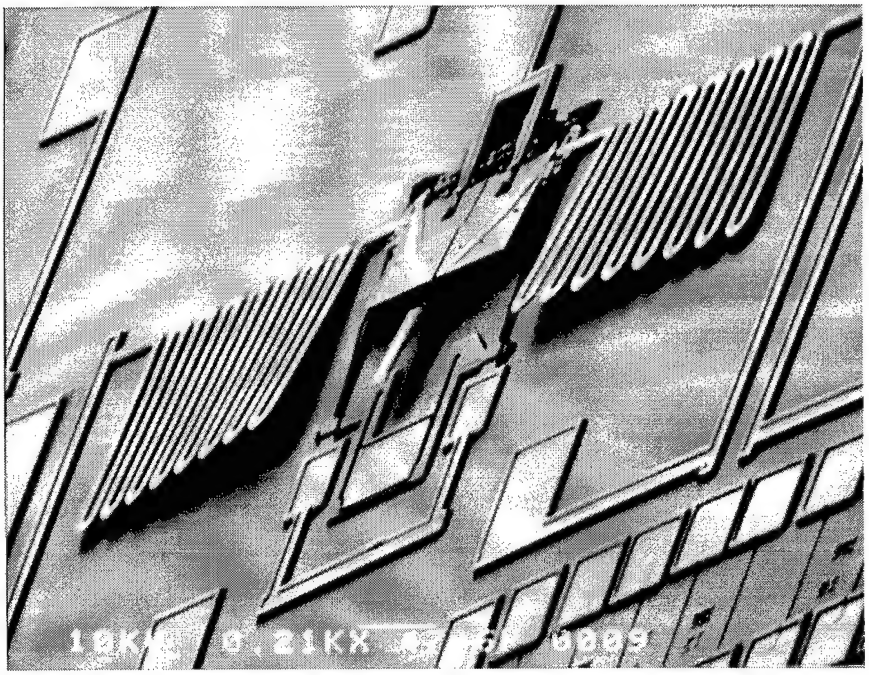

Figure 5-5: Scanning electron micrograph of lifted leg and base.

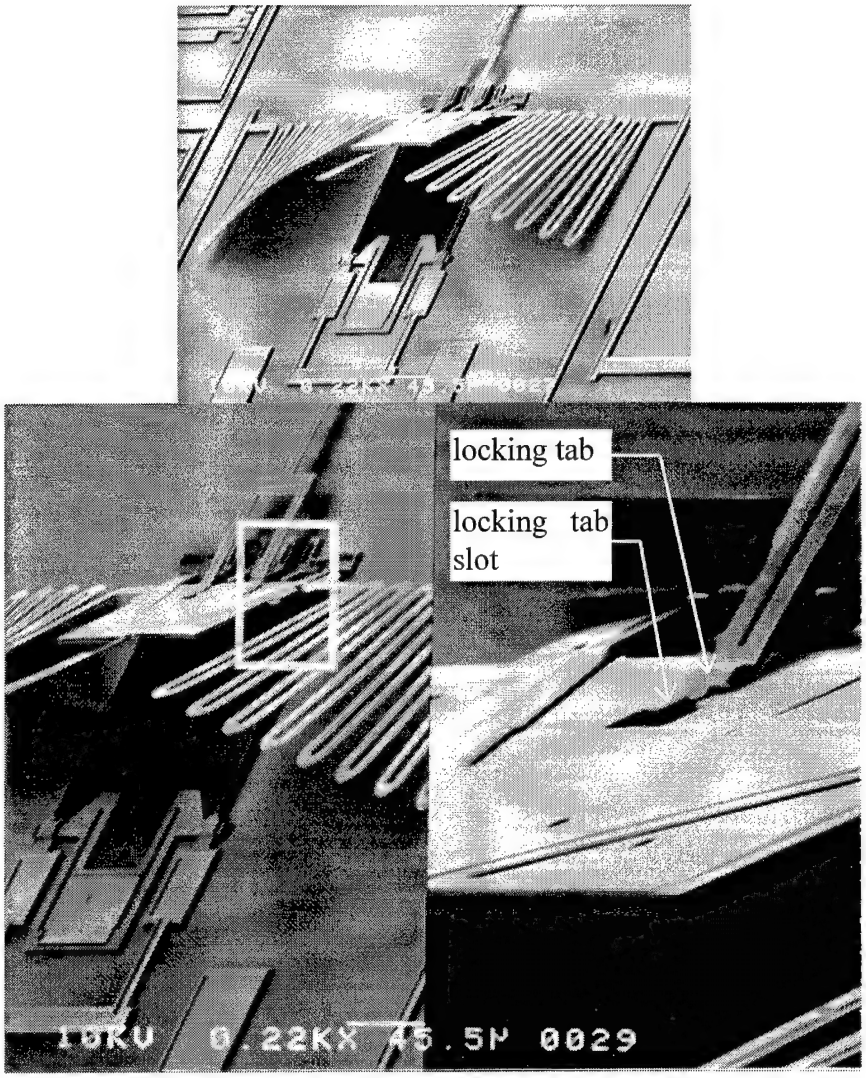

Figure 5-6: Scanning electron micrographs of the leg and base after being locked into the locking tabs and a close up view of a locking tab and locking tab slot. The base was lifted with probes until the locking tabs locked into place.

Designs for the MUMPs 19 fabrication run were due before MUMPs 18 was received at AFIT and analyzed. For this reason, lessons learned from MUMPs 18 could not be applied to this run. In this design, the objective was to make the self assembly system as compact and as simple as possible.

Figure 5-7 shows a captured video image of the prototype self assembly system designed for MUMPs 19. The intended operation of this system is as follows. The jacks give the base an initial lift. Next, the locking tab arrays flex towards the base to lock the locking tabs into the locking slots.

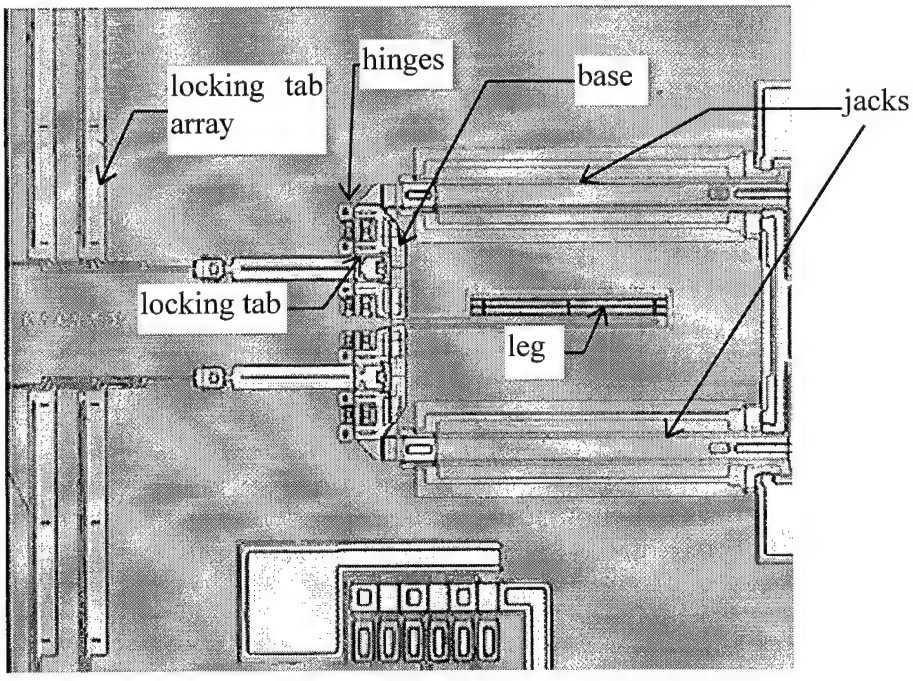

Figure 5-7: Captured video image of a prototype self assembly system designed for MUMPs 19.

The locking tab arrays then can be adjusted by backbending or operation in the normal mode to move the leg into a desired position. Electricity is supplied to the leg through each side of the base. Each side of the base is supplied electricity through the physical contact of the locking tab to the base. The two locking tab arrays are electrically separated, so the leg can be powered through the same probe pads which are used to supply power to the locking tab arrays. Figure 5-8 shows a scanning electron micrograph of the leg and base after being lifted by the jacks. The leg is bent down towards the substrate because the hot arm and cold arm flexure have been melted from being over driven. Figure 5-9 shows a closer view of the leg and base.

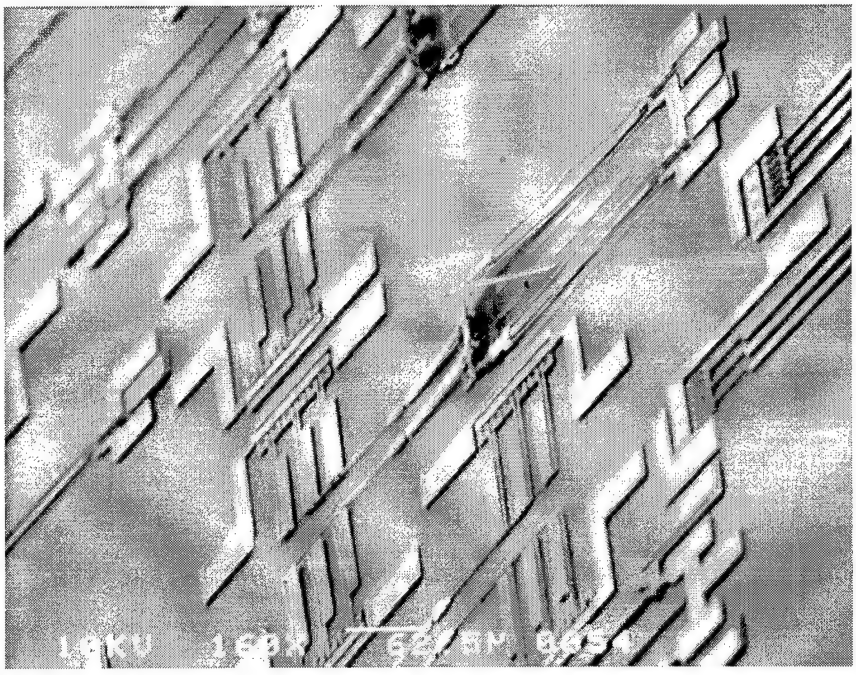

Figure 5-8: Scanning electron micrograph of leg and base after being lifted by the jacks. The leg is bent down towards the substrate because the hot arm and cold arm flexure have been melted from being over driven.

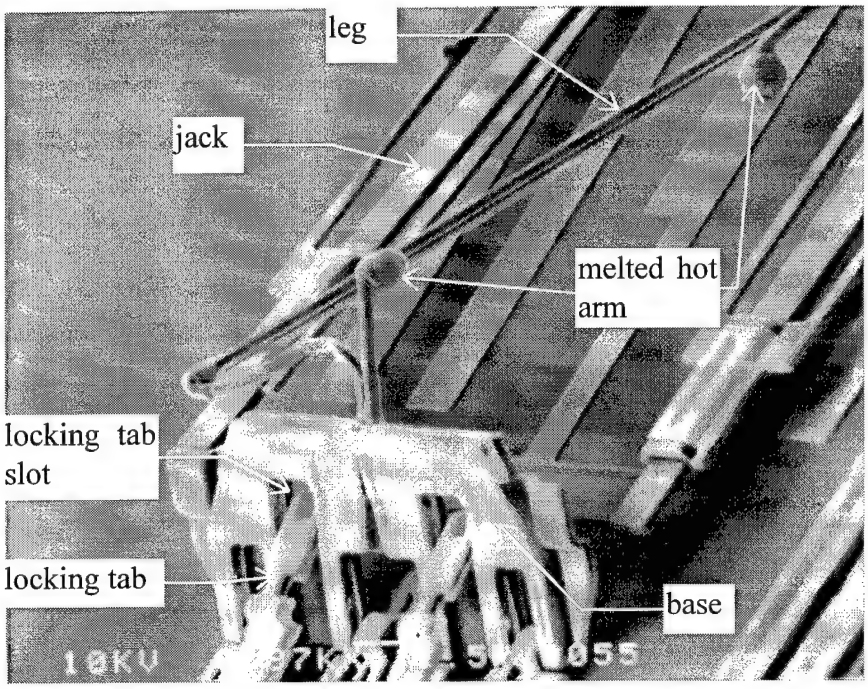

Figure 5-9: A closer view of the leg and base from Figure 5-8. Note, the locking tabs are not fully engaged in the locking tab slots.

Although the jacks were able to lift the base very high, as seen in Figure 5-9, the locking tab arrays were not able to flex far enough for the locking tabs to lock fully into place. The locking tabs missed the locking tab slots by approximately 4 μm. If the locking tabs in this design are extended four or more micrometers, this would be a successful self assembly design, however, the mechanical contacts between the base and locking tabs would not be a low resistance connection. The electrical contacts are discussed further in Section 5.2.

For this fabrication run, the microrobot was designed. The leg for the microrobot is based on the same self assembly systems as in the previous two fabrication runs. In this design, the s-wires have been redesigned for a more compact size, while still being flexible. The redesigned s-wires are now called "spring wires". Also, the jacks were moved closer to the pivot point of the base. This design will be discussed in more detail in Section 5.4 where the microrobot design is presented, however, the results pertaining to self assembly will be discussed here.

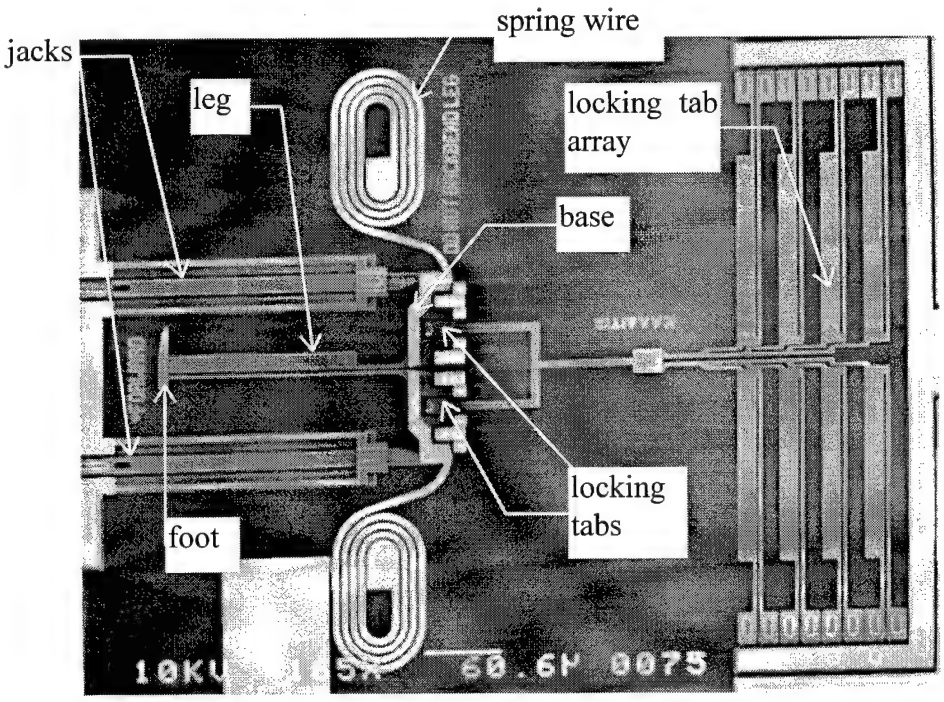

Figure 5-10: Scanning electron micrograph of the microrobot leg self assembly system designed for the MUMPs 20 fabrication run.

Figure 5-10 shows a scanning electron micrograph of the microrobot leg self assembly system designed for the MUMPs 20 fabrication run. The intended method of erecting the leg and base is the same as in the MUMPs 19 design. The jacks are meant to initially lift the base. Next, the locking tab array is flexed to lock the locking tabs into the base. Power is then removed from the locking tab array to allow the leg to be pulled into a normal to the substrate position. The locking tab array can also be back-bent to further pull the base and leg into a desired position.

Unfortunately, the jacks were not able to lift the base significantly. From Figure 5-11, it is estimated that the base is lifted a degree or less.

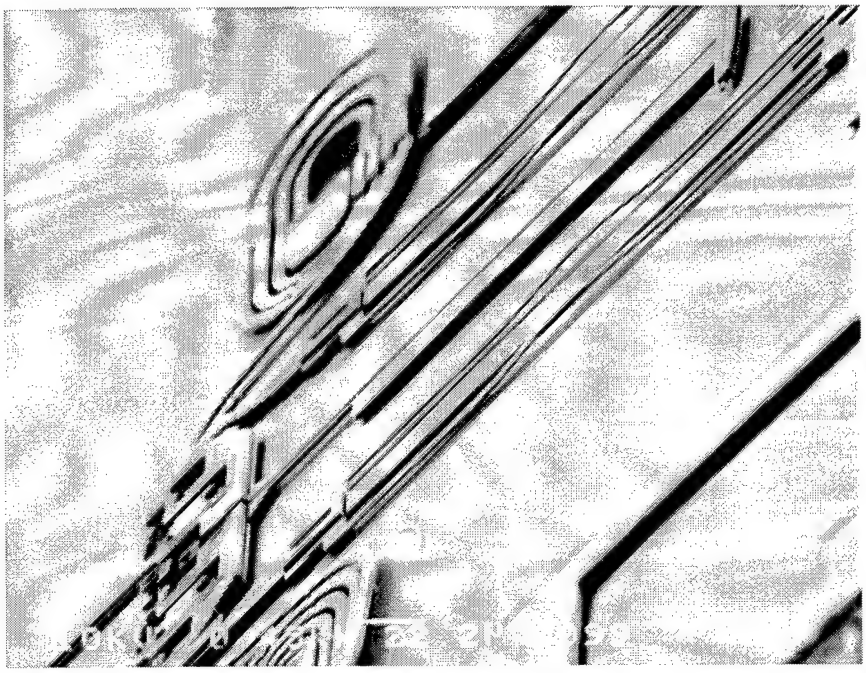

Figure 5-11: Scanning electron micrograph showing leg and base barely lifted from the substrate by the back-bent jacks.

Most likely, the spring wires are too stiff for the jack to twist by lifting the base. To support this conclusion, a static analysis is performed on this design where the force that the jacks provide, the resistive torque from the twisting of the spring wires, and other forces are estimated and compared. For this analysis please see Appendix A.

Design and Results Pertaining to the MUMPs 21 Fabrication Run

Another microrobot leg self assembly system was designed for the MUMPs 21 fabrication run. The leg is part of another microrobot design. Figure 5-12 shows a CADENCE drawing of this self assembly system.

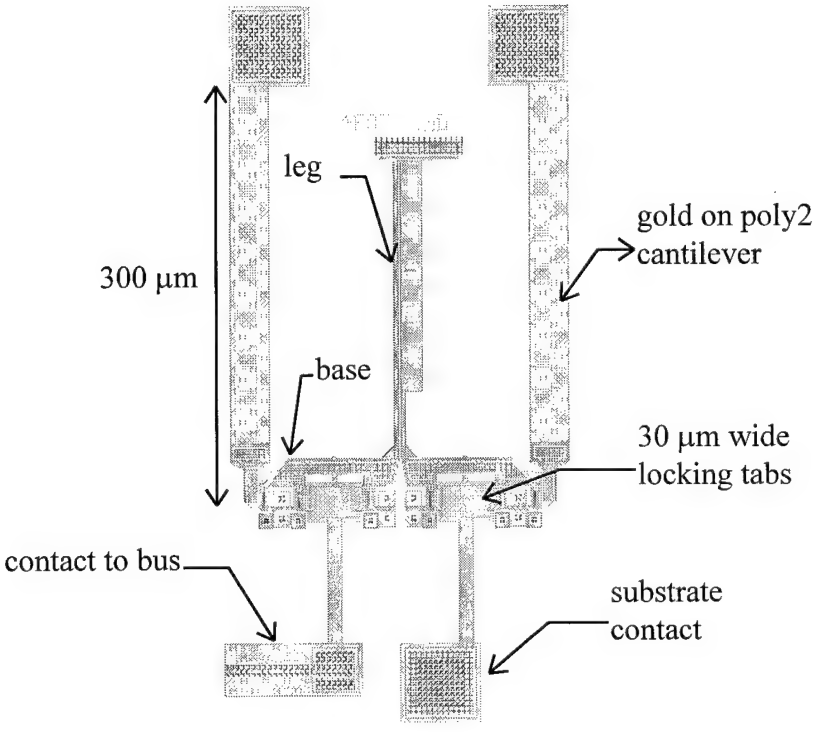

Figure 5-12: CADENCE drawing of a prototype microrobot leg self assembly system designed for fabrication in the MUMPs 21 fabrication run.

This system is intended to assemble during the release process. Gold covered poly2 cantilevers, anchored to the nitride at one end, and positioned under the base at the other, are used as the jacks. The intended operation of this self assembly system is as follows. As this system is released, the cantilevers curl away from the substrate due to the stress of the gold on the poly2. As the cantilevers curl, the base is raised and pivoted about its hinges, and locked onto the locking arms. The agitation of the release fluids, on the leg and base, assist in locking the base onto the locking arms.

Extra wide (30 μm) locking tabs are used to increase contact area between the locking arms and the base. The wide locking tabs are used in hopes of achieving lower resistance electrical connections with the base. The leg is powered through the locking arms.

The deflection (d) of the end of the cantilever was designed using the relationship given by Obermeier [2]:

$$d = \frac{(1-\nu)3L^2 t_{gold}}{Et_{poly2}^2}\sigma_{gold},$$

where ν is Poisson's ratio, L is the length of the cantilever, t_{gold} is the thickness of the gold layer, E is Young's modulus, t_{poly2} is the thickness of the poly2 layer, and σ_{gold} is the stress of the gold layer. Letting $\nu = 0.22$ [3], $L = 300$ μm, $t_{gold} = 0.5$ μm, $E = 169$ GPa [3], $t_{poly2} = 1.5$ μm, and $\sigma_{gold} = 67.5$ MPa (average of the reported gold stress measurements from the previous four MUMPs fabrication runs), the deflection of the cantilever (d) is approximately 18.7 μm.

Figure 5-13 shows an assembled microrobot leg. The deflection of unloaded cantilevers were measured to be 20 - 23 μm, which, agrees rather well with the above prediction. Unassisted by agitation during the release process, the cantilevers could raise microrobot legs to approximately 20 degrees with respect to the substrate. Assisted by agitation during the release process, the legs could be raised to 90 degrees and locked into place.

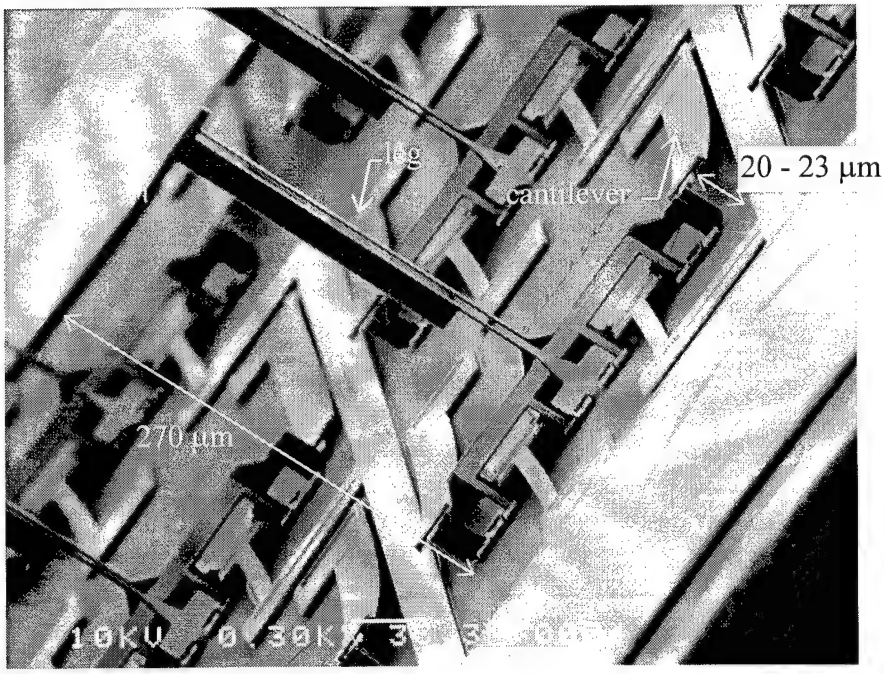

Figure 5-13: Scanning electron micrograph of assembled microrobot leg used in the microrobot design of the MUMPs 21 fabrication run.

The self assembly mechanisms of this system are very unreliable, however, and for the most part, unpredictable. The microrobot in this design has 90 legs. Results varied from as few as one leg being raised 20 degrees to 50 legs being locked into place.

A release method that could reliably assemble the robot legs was not found. The unreliability can be attributed to a design error where the gold layer of the cantilever is the same width as the poly2 layer. Due to slight misalignment of the photoresist mask used in the lift off process of patterning the gold, a thin pattern of gold is formed beside the poly2 cantilevers. During the release process, as the oxide is etched away, the thin pattern of gold drops onto the nitride and sticks. The thin gold pattern can also contact the side of the cantilever. When the thin gold pattern is sticking to the nitride and contacting the side of the cantilever, the cantilever can be restrained from deflecting. Future designs should keep the gold layer at least 2 μm away from the edge of the poly2.

5.2 Providing Electrical Power To Erected Structures By Means Of Practical Low Resistance Electrical Connections

This section presents the theory, design, and results pertaining to Research Goal 2: provide electrical power to erected structures by means of practical low resistance electrical connections. The designs in this section will be presented in chronological order with reference to the different MUMPs fabrication runs.

Designs and Results Pertaining to the MUMPs 17 Fabrication Run

Figure 5-14 (a) shows a scanning electron micrograph of a hinged horizontally deflecting thermal actuator; (b) shows the same actuator after being erected normal to the

substrate with probes. This design is the first attempt, in this research, of providing low resistance electrical connections to erected microstructures. Each flexure of the actuator is connected to a probe pad through gold on poly2 lines that are not anchored to the nitride. However, a small intentional gap was designed in each poly2 line, but not in the gold. The gap was just small enough for a gold bridge to form across the gap during fabrication. This experiment was to determine if the gold could bend, while the actuator is pivoted to the upright position, and still maintain an electrical connection. As shown in Figure 5-14 (b), the gold snapped.

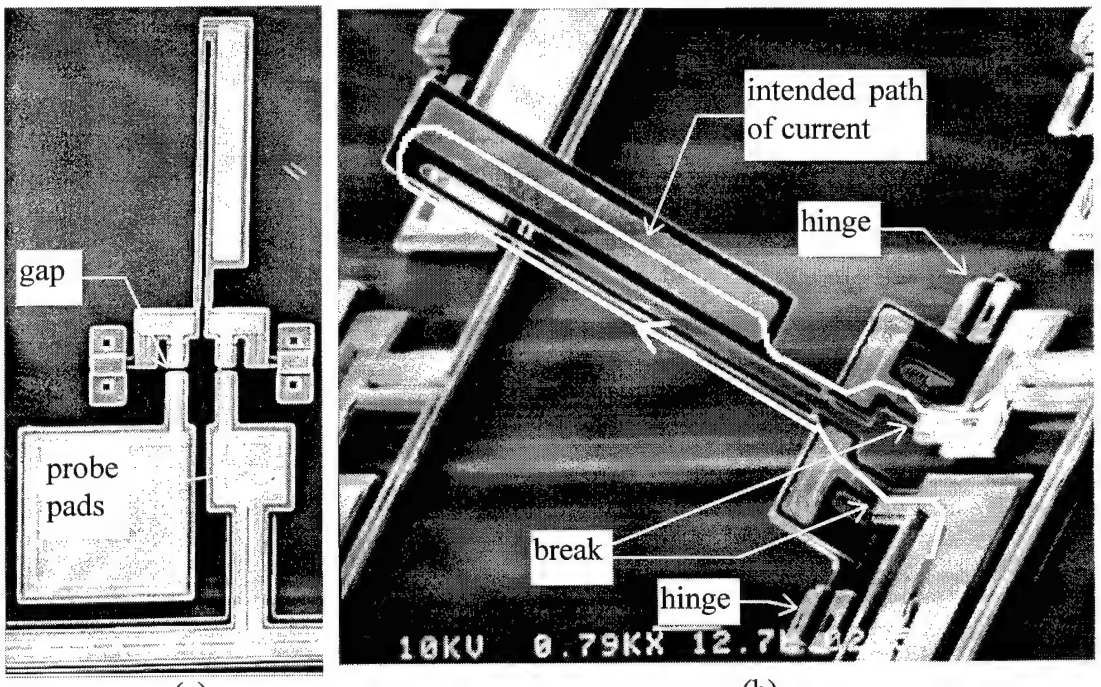

(a) (b)

Figure 5-14: Scanning electron micrographs of a hinged horizontally deflecting thermal actuator: (a) initial position, (b) erected with probes. This device was designed for the MUMPs 17 fabrication run.

Since the hinge pins touch the hinge caps, supplying electricity to the actuator

through the hinge caps was also attempted. A probe was placed on each hinge and a voltage of up to 24 V applied, however, no current flow was measured.

Designs and Results Pertaining to the MUMPs 18 Fabrication Run

In these designs, s-wires were used to successfully supply low resistance electrical connections to erected structures. Figure 5-1, Figure 5-2, Figure 5-3, and Figure 5-6 show four different designs. The s-wires are made from gold on poly2 and are 10 μm wide. The s-wires supply electricity to each side of the base, and each side of the base is connected to each flexure of the leg, respectively. Figure 5-15 shows two legs that were overdriven to provide dramatic evidence of the current capability of the s-wires.

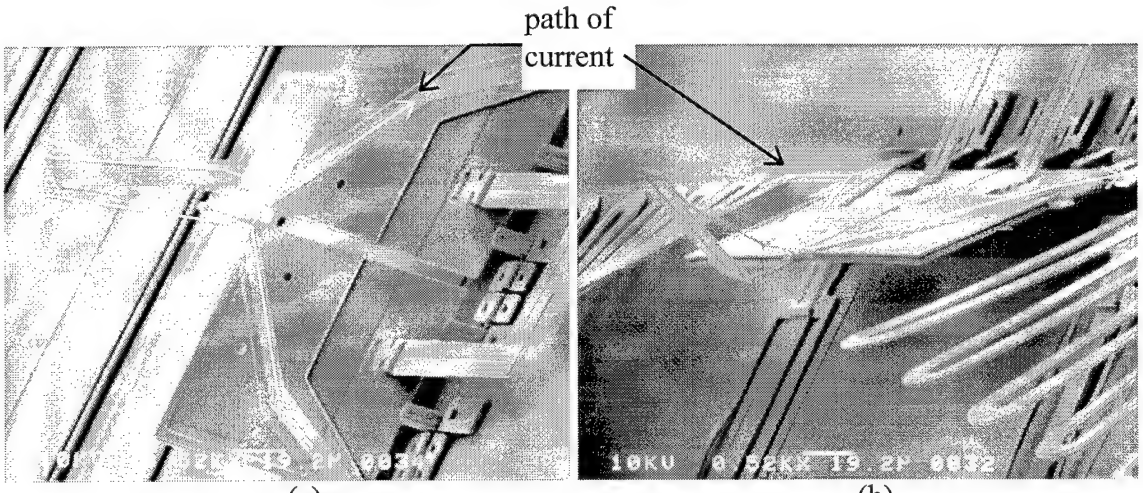

(a) (b)

Figure 5-15: Scanning electron micrographs showing (a) a melted hot arm of a leg, and (b) a back-bent leg. The legs were melted and back-bent through the s-wires.

Designs and Results Pertaining to the MUMPs 19 Fabrication Run

In the MUMPs 19 fabrication, supplying electrical power to erected structures through mechanical contacts was investigated. Figure 5-7 - Figure 5-9 show a design where this concept was tested. Electricity is supplied to each side of the base from locking tabs that are inserted into locking tab slots. The locking tab slots are located in the center of each side of the base. The intended operation of this electrical supply is that the physical contact between the underside and sides of the locking tabs with the edges of the locking tab slots will pass current. An advantage of this method of electrical supply are that the jacks can raise the base with less mechanical resistance than if there were s-wires or spring wires attached to the base. A disadvantage of this method of electrical supply is that it turns out to be a high resistance contact. For example, the device shown in Figure 5-9 would not conduct current until an input voltage of over 20 volts was reached. Consequently, the physical connection must have fused, and the large input voltage immediately caused the leg to melt.

Designs and Results Pertaining to the MUMPs 20 Fabrication Run

In this fabrication run, the s-wires from the MUMPs 18 fabrication run were redesigned to be more compact and flexible. The redesigned wires are named "spring wires". Several different working designs were created. Figure 5-16 shows scanning electron micrographs of some of the versions of spring wires created. Each end of a

spring wire, in Figure 5-16, is connected to a probe pad, and the other end is connected to a base.

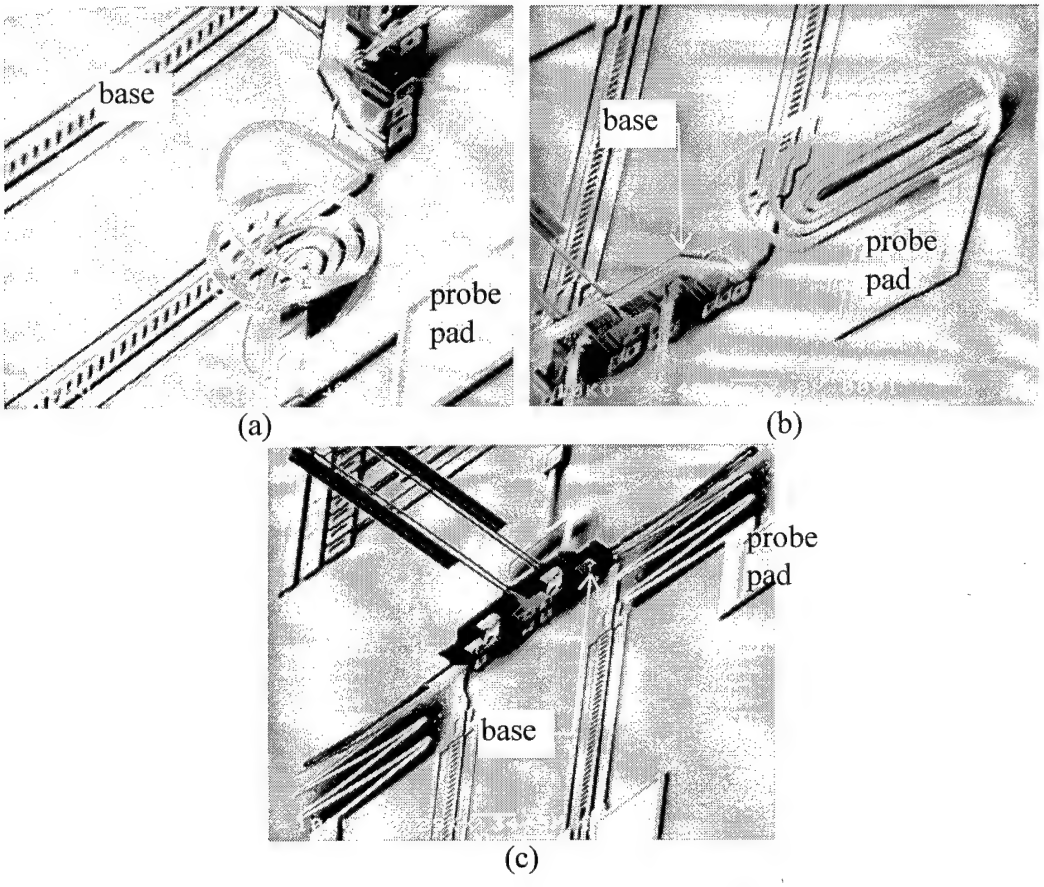

Figure 5-16: Scanning electron micrographs of different style spring wires designed for the MUMPs 20 fabrication run.

Another version of spring wire design was adopted for use in powering the microrobot leg system. The microrobot leg system will be described in detail in Section 5.4. Figure 5-17 (a) shows a scanning electron micrograph of the final microrobot leg design after being erected with probes. The spring wires can be seen connected to either side of the base. Figure 5-17 (c) - (d) shows closer views, from different perspectives, of the spring wire. All of the spring wire designs except for Figure 5-16 (a) can be twisted

to 180°. The spring wire of Figure 5-16 (a) breaks, near the base, at aproximately 135°.

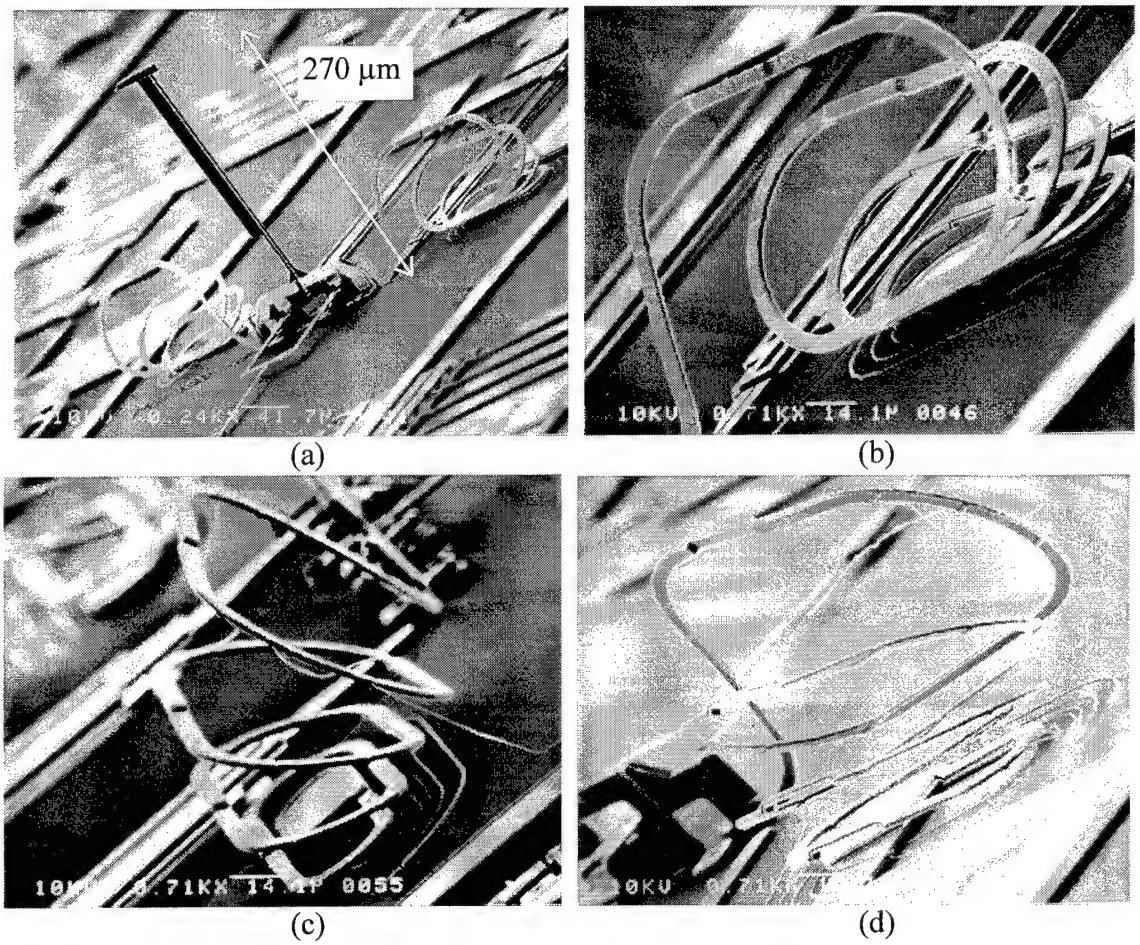

Figure 5-17: Scanning electron micrographs of microrobot leg system and different perspective views of spring wires: (a) shows a full view of microrobot leg system with spring wires connected to either side of the base; and closer views of the spring wire from (b) front or top view, (c) side view, and (d) back or bottom view.

Another attempt at creating a flexible low resistance electrical connections for self assembly systems is "chain wire". Chain wire is an interlocking chain of polysilicon links. The polysilicon chain is then coated with a layer of gold. Figure 5-18 shows two different versions of chain wire.

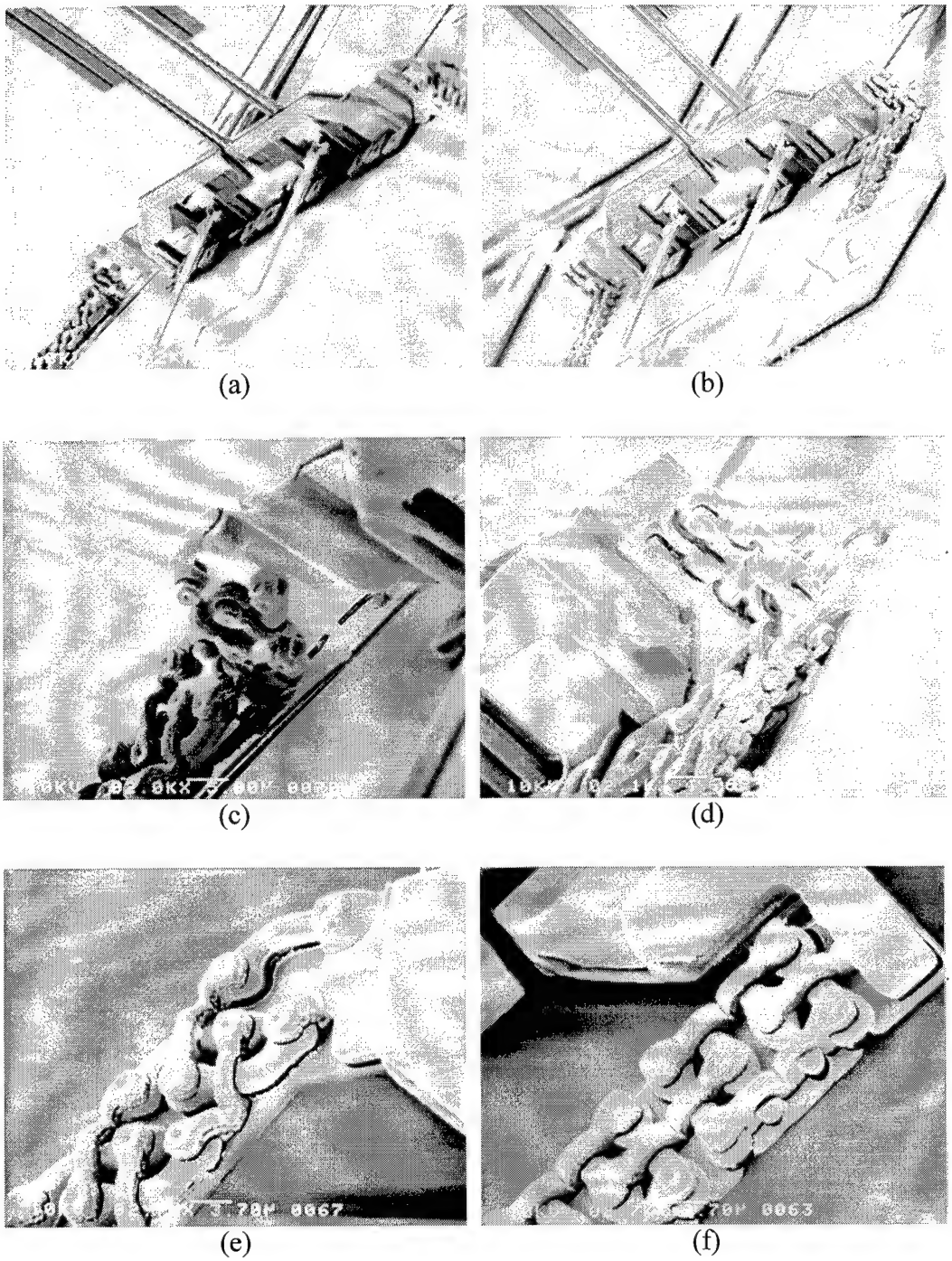

Figure 5-18 Scanning electron micrograph of "chain wire". Subfigure (a) shows a far view of the chain wires connected to either side of the base, and the other ends of the chain wires are connected to probe pads not in view; (c) shows a closer view of the chain wire connected to the left side of the base; and (e) is a close view of the chain wire connected to the base before the base is erected with probes. Subfigures (b), (d), and (f) are the same type of views except a different style chain link is employed in the chain wire.

Figure 5-18 (a) shows a far view of the chain wires connected to either side of the base, and the other ends of the chain wires are connected to probe pads not in view; (c) shows a closer view of the chain wire connected to the left side of the base; and (e) is a close view of the chain wire connected to the base before the base is erected with probes. Subfigures (b), (d), and (f) are the same type of views except a different style chain link is employed in the chain wire.

The gold was intended to form a continuos flexible sheet over the chain links, or at least form conductive bridges between chain links. Although the chain wires turned out to be non-conductive, the design is still noteworthy for its possible applications or refinement.

5.3 Realizing Circular Motion Normal to the Substrate

This section presents the theory, design, and results pertaining to Research Goal 3: realize circular motion normal to the substrate. The designs in this section will be presented in chronological order with reference to the different MUMPs fabrication runs.

Designs and Results Pertaining to the MUMPs 17 Fabrication Run

Figure 5-19 shows a prototype wheel system designed for the MUMPs 17 fabrication run. The objective of this design was to demonstrate that a wheel could be assembled normal to the substrate. Figure 5-19 (a) shows the wheel unassembled, (b)

shows the wheel after being assembled by probes, and (c) is a close side view of the wheel at the hub. The wheel is assembled by first folding up both "hinged A-frames" with probes. The hinged A-frames will remain in an upright position. Next, the 222 μm diameter wheel is snapped off of a thin poly2 hold down with probes, much like snapping off plastic model parts from a model tree. The wheel is then lifted with probes and pressed onto the snap on axle of the A-frame.

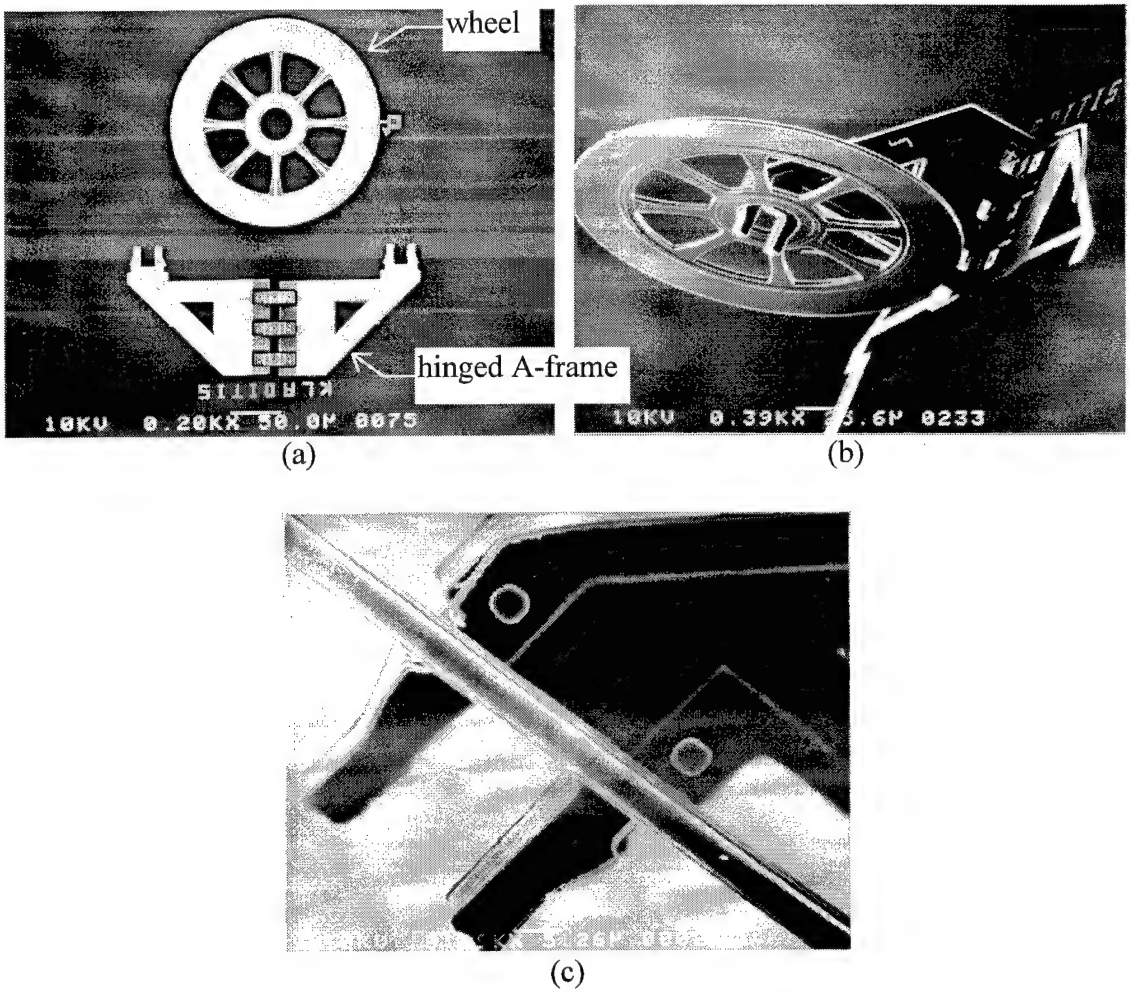

Figure 5-19: Scanning electron micrographs of a wheel erected normal to the substrate: (a) shows the wheel unassembled, (b) shows the wheel after being assembled by probes, and (c) is a close side view of the wheel at the hub.

Figure 5-20 shows a scanning electron micrograph of a wheel with the same basic design as in the MUMPs 17 wheel, except teeth are added to the wheel. Also, a vertically deflecting thermal actuator is added under the wheel. After being back-bent, the actuator can be actuated with a pulsed signal causing the actuator to move up and down with respect to the substrate. The end of the actuator is intended to catch on the teeth of the wheel and cause it to rotate.

Figure 5-20: Same wheel system design as in Figure 5-19 except teeth are added to the wheel and a vertically deflecting thermal actuator is added to spin the wheel. Fabricated in the MUMPs 19 fabrication run.

The wheel in Figure 5-20 did not rotate, because the wheel is too tight on the axle. Both the wheel and the A-frame where observed to shake while pulsing the vertically

deflecting thermal actuator. A design, successful in realizing rotating motion, is shown, unassembled, in Figure 5-21. With reference to Figure 5-21, when the frame is pushed from the left end with a probe, the frame will fold up in the middle. "Folding hinges" allow the middle of the frame to fold up away from the substrate. The right side of the frame is held in place, but allowed to pivot, by hinges anchored to the nitride. Guides on either side of the frame keep the frame straight as it folds into position. The guides have toothed notches that ratchet past a toothed lock. The toothed lock allows the frame to be held at various upright positions. As the frame folds into its upright position a 222 μm in diameter, toothed wheel unfolds off of the frame and drops down into a "V" shaped part of the frame. The final upright position of the frame places the edge of the wheel over the "Y"-shaped end of a vertically deflecting thermal actuator. After being back-bent, the thermal actuator can be pulsed to bump the edge of the wheel, causing the wheel to spin. Figure 5-22 shows the wheel system after being assembled. Figure 5-23 is a closer view of where the tip of the vertically deflecting thermal actuator meets the teeth of the wheel.

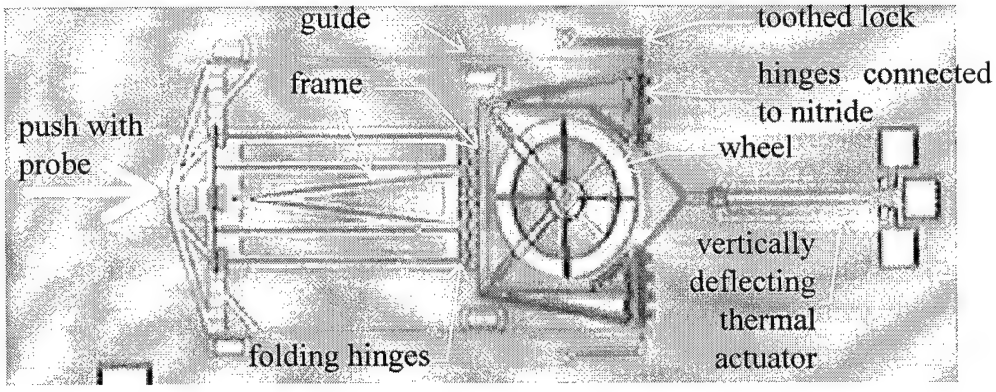

Figure 5-21: Captured video image of an unassembled, rotating wheel system fabricated on the MUMPs 19 fabrication run.

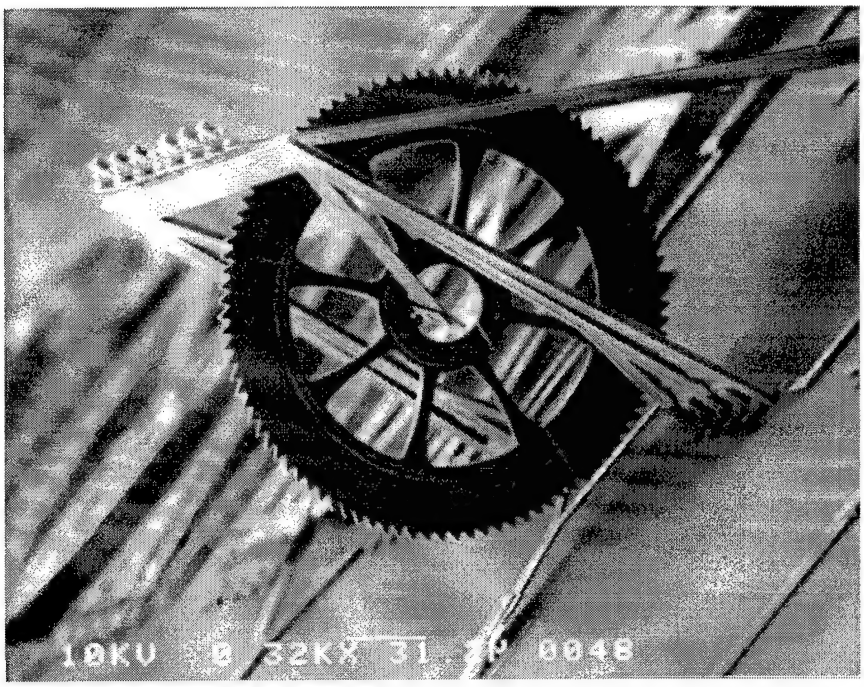

Figure 5-22: Scanning electron micrograph of the rotating wheel from Figure 5-21 after being assembled.

Figure 5-23: Closer view of where the tip of the vertically deflecting thermal actuator meets the teeth of the wheel.

For this experiment, the vertically deflecting thermal actuator was back-bent by applying a potential of 16 volts and 4.3 mA DC through the hot arms of the actuator for 10 seconds. The vertically deflecting thermal actuator was powered using a square wave input. The amplitude and frequency of the square wave was varied. The wheel would not spin because the teeth were getting caught on the top of the frame. To remedy this situation, the laser cutter was used to cut out a section of the top of the frame. Figure 5-24 shows an example of a cut frame (a) before assembly and (b) after assembly.

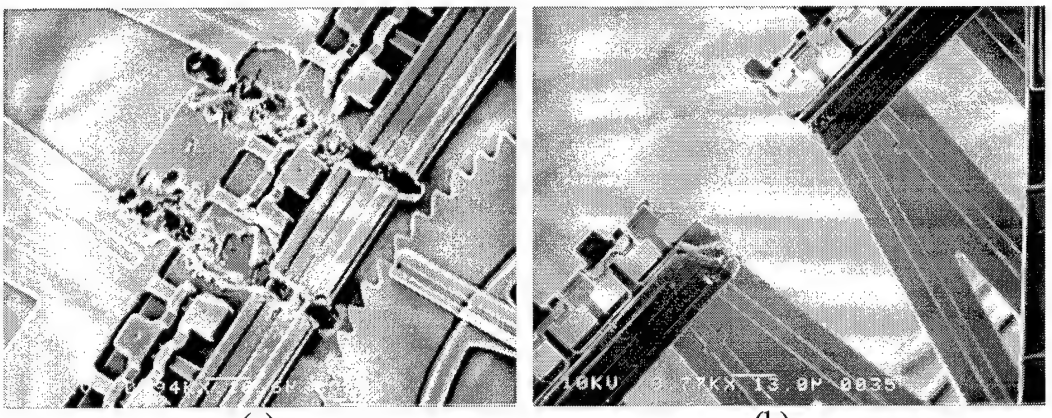

(a) (b)

Figure 5-24: Scanning electron micrographs of the top section of the rotating wheel system, from Figure 5-21, after being cut by the laser cutter: (a) frame before assembly and (b) frame after assembly.

After cutting the frame with the laser cutter, the frame was assembled with probes, and the vertically deflecting thermal actuator back-bent. A 3.2 volt amplitude square wave input to the vertically deflecting actuator at frequencies around 7.2 Hz was found to cause the wheel to rotate. The wheel was observed to spin at an average angular velocity of approximately 2 radians/second. The wheel would not rotate continuously,

however. After a few seconds, the wheel would travel up its "V"-shaped holder in the frame and loose contact with the actuator, or the wheel would turn sideways and get stuck on the frame.

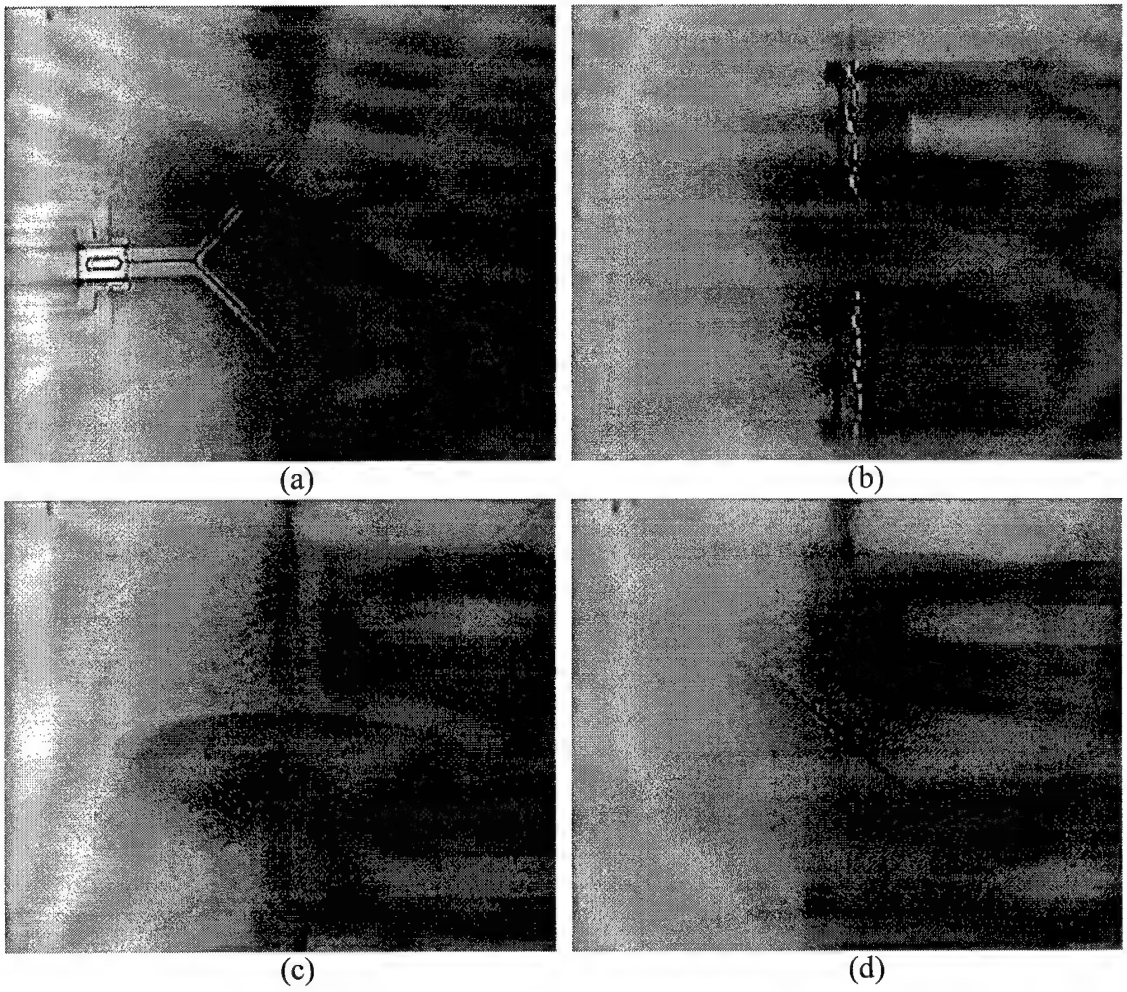

Figure 5-25: Captured video images of the rotating wheel experiment recorded through the video camera on the probe station: (a) is a top view of the rotating wheel system with the microscope objective focused on the vertically deflecting thermal actuator, (b) same view with focus on the top of the frame, (c) same view with focus on the teeth of the wheel before rotating, (d) same view of the top teeth of the wheel after rotating.

Video footage of the experiment was collected through the probe station video

camera. From the video, the displacement of the wheel could be observed and timed. Figure 5-25 shows captured video images of the rotating wheel experiment recorded through the video camera on the probe station. Figure 5-25 (a) is a top view of the rotating wheel system with the microscope objective focused on the pulsing vertically deflecting thermal actuator, and (b) is the same view with the focus on the top of the frame. Figure 5-25 (c) is the same view, as in (a), with focus on the teeth of the wheel before rotating, and (d) is the same view of the top teeth of the wheel, 2.4 seconds later, after rotating $3\pi/2$ radians.

Designs and Results Pertaining to the MUMPs 21 Fabrication Run

Figure 5-26 shows a CADENCE drawing of an unassembled electrostatic version of the MUMPs 19 rotating wheel system. The design in Figure 5-26 uses the same frame design (with slight modifications) as that shown in Figure 5-21. The wheel has been changed by adding large rectangular electrostatic pad teeth. Instead of a vertical thermal actuator to turn the wheel, five pairs of fold up electrostatic pads are provided. At least three consecutive pairs of electrostatic pads, however, are needed for proper operation. Attractive electrostatic forces between the teeth and the electrostatic pads is meant to cause rotation of the wheel. The frame is grounded to the substrate, and the fold up electrostatic pads are connected to probe pads. The geometry of the fold up electrostatic pads and the pads on the wheel is based on the optimized 12:8 salient pole motor analyzed and described by Garverick, et al. [4], and Dufour, et al. [5].

The frame and wheel can be assembled to their upright position using probes. The five pairs of electrostatic pads can then be folded up using probes. Special locking tabs keep the frame and electrostatic pads held in place after assembly.

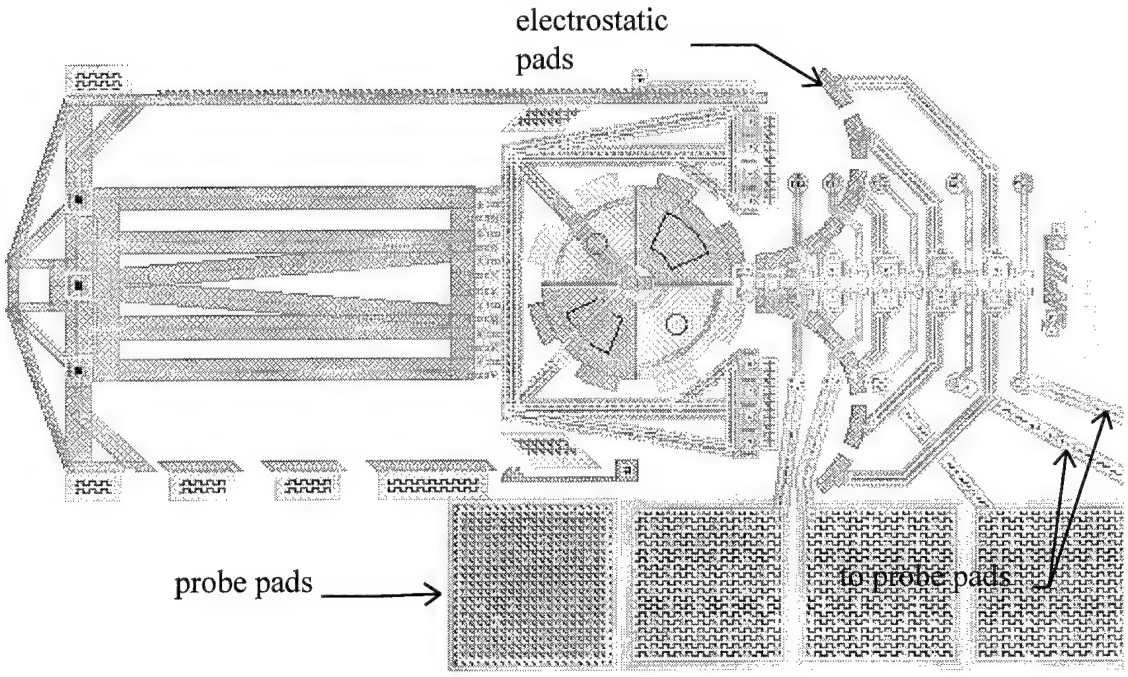

Figure 5-26: CADENCE drawing of an electrostatic rotating wheel designed for fabrication in the MUMPs 21 fabrication run. Note, two of the right most probe pads are not shown.

Figure 5-27 shows the electrostatic wheel system after assembly. The probe pads used to apply potential to the fold up electrostatic pads are labeled "A" - "D" in Figure 5-27. The pair of electrostatic pads supplied by probe pad "D" were not used, and are shown erected, and locked into place, but moved away from the wheel. This same pair of electrostatic pads also demonstrates the, undesired, mechanical play allowed by the

locking tabs. This same mechanical play allowed the other electrostatic pads to short circuit to the wheel, causing this system to fail.

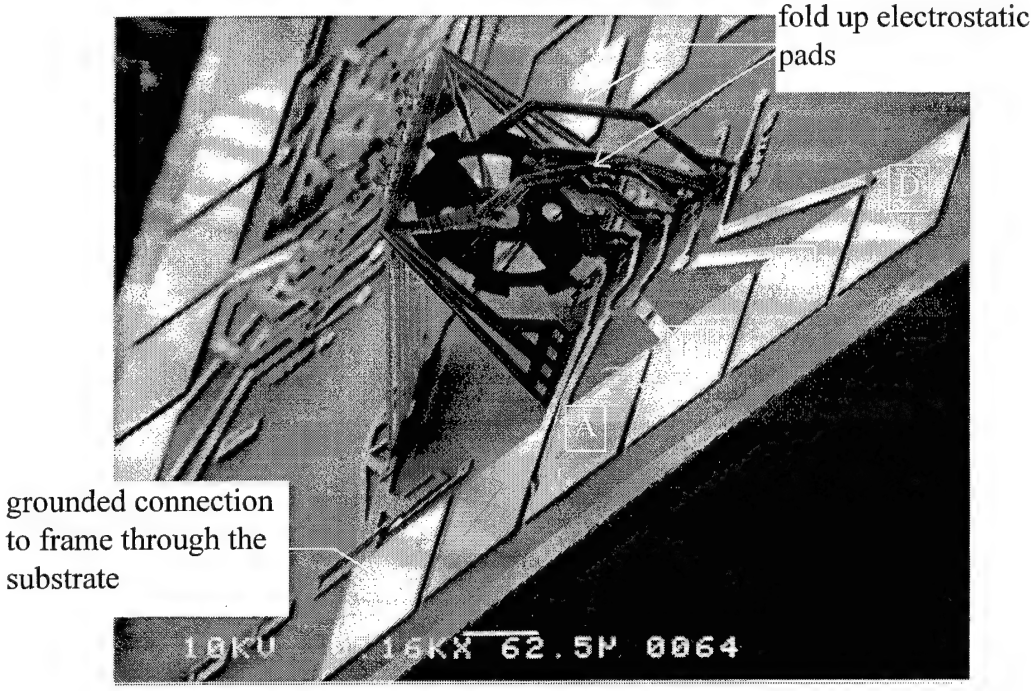

Figure 5-27: Scanning electron micrograph of assembled electrostatic rotating wheel system

Figure 5-28 shows one period of the input signal arrangement used to apply potential to probe pads "A" - "C". The three channel sequencer, described in Chapter 4, was used to implement the input signals. The frequency and amplitude were varied, however, rotation of the wheel was not observed. The wheel was observed to move from side to side, short circuiting to the fold up electrostatic pads. Figure 5-29 and Figure 5-30 show closer views of the wheel system from Figure 5-27. The micrographs in Figure 5-29 and Figure 5-30 also reveal damage to different components of the wheel system. The

damage was caused by melting when the electrostatic pads short circuited to the wheel during the application of high voltage input signals (approximately 10 volts and greater).

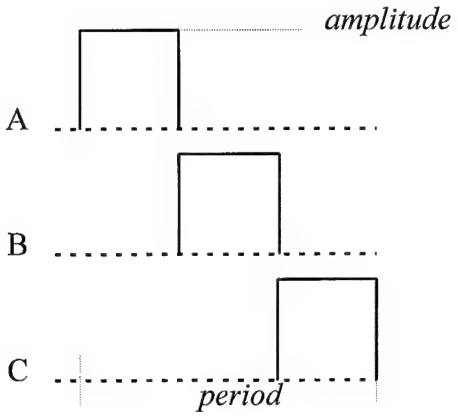

Figure 5-28: Input signal arrangement used to apply potential to the electrostatic pads of the rotating wheel system.

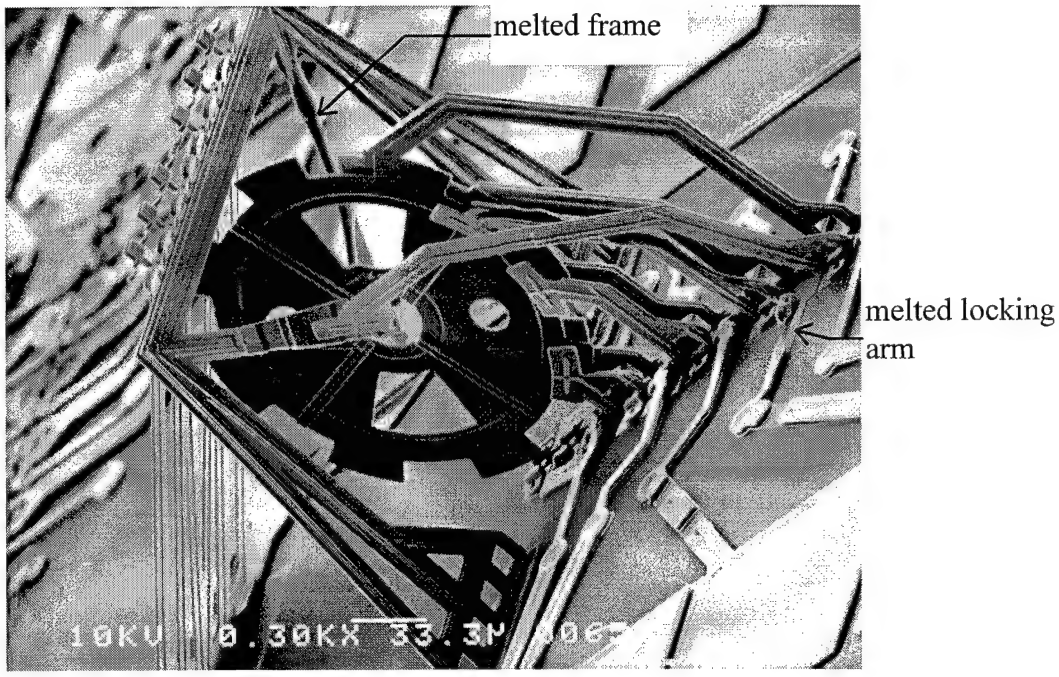

Figure 5-29: Closer view of the electrostatic wheel system from Figure 5-27.

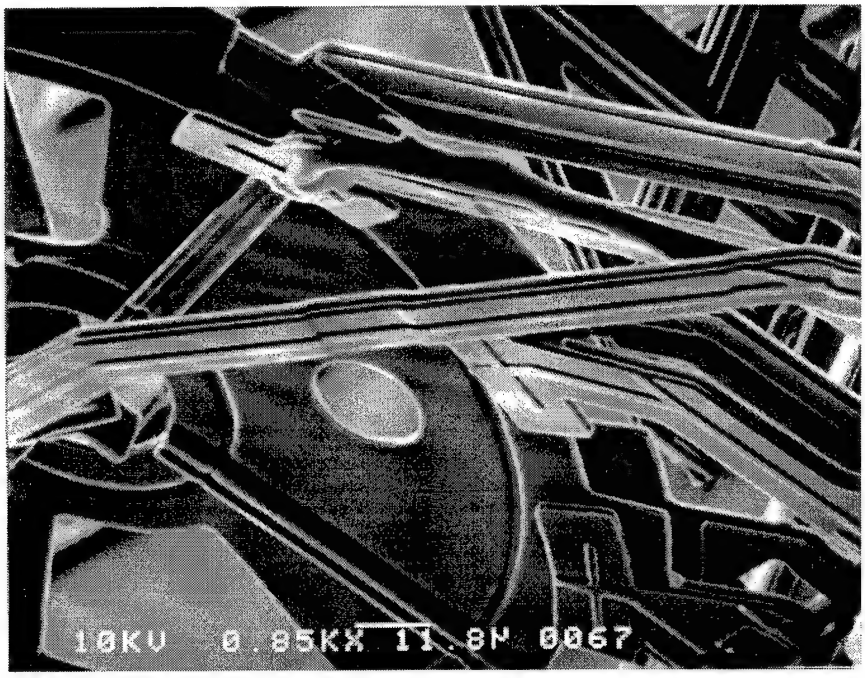

Figure 5-30: Closer view of the electrostatic wheel system from Figure 5-27.

5.4 Realization of a Microrobot That Can Move on a Flat Surface

This section presents the theory, design, and results pertaining to Research Goal 4: realize a microrobot that can move on a flat surface. All the designs presented in this section were fabricated in the MUMPs 20 fabrication run.

Description of Microrobot: Introducing "Chip"

The microrobot, named "Chip," created by this research is intended to be capable of moving or walking across a flat surface. This microrobot is simply a 1 cm x 1 cm by 550 μm die with ninety-six thermal actuators serving as legs when the die is set, micromachined face down, towards the walking surface. Horizontally deflecting thermal actuators are erected normal to the substrate surface, using probes, before the die is turned over and set on the walking surface. The legs are powered remotely through three gold wires connected to the die by wirebonding.

The method of propulsion is modeled after six-legged insects where three legs are contacting the walking surface at any one time [6]. The three legs form a tripod throughout the motion of the insect, this is illustrated in Figure 5-31. However, the microrobot has more than six legs, the several legs needed to support the weight of the die, are functionally and physically arranged into six groups.

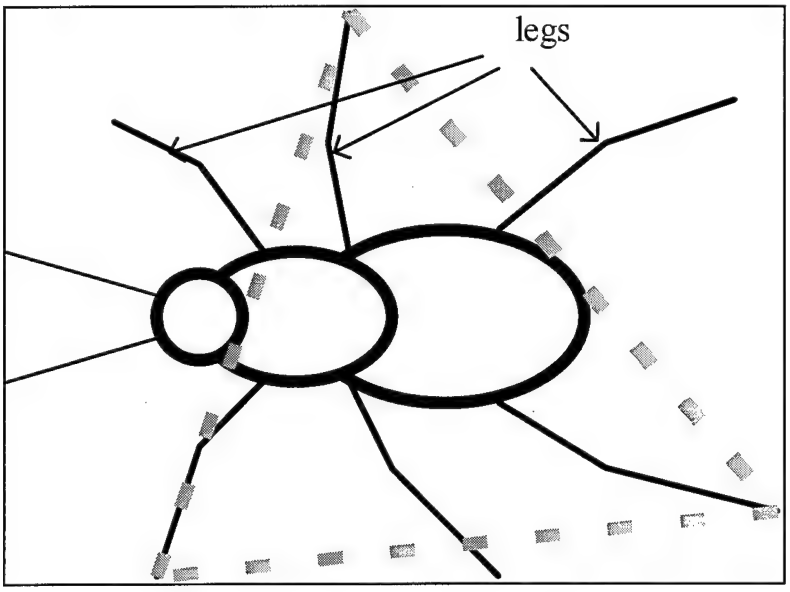

Figure 5-31: Simplified drawing of six legged insect showing three legs in the tripod arrangement [6].

Figure 5-32 is a simplified drawing of the microrobot showing a simplified wiring scheme and drive signal. Note that the six actuators shown in the drawing actually represents six groups, where each group contains sixteen actuators. Each group is labeled "front A," "rear B," etc. Actuators in a group are driven, in parallel, by the same signal from line "A" or "B". The signal on line "A" is 180 degrees out of phase with the signal on line "B." The intended operation is described as follows, with reference to Figure 5-32. During the positive phase of the drive signal on line "A", the actuator groups "A" are deflected (and slightly extended) causing forward motion of the microrobot. During the positive phase of the drive signal on line "B", the actuator groups "B" are deflected (and slightly extended) also causing forward motion of the microrobot. Simultaneously, during this phase, the group A actuators will be returning to their original position to deflect again during the next positive phase of the line "A" drive signal.

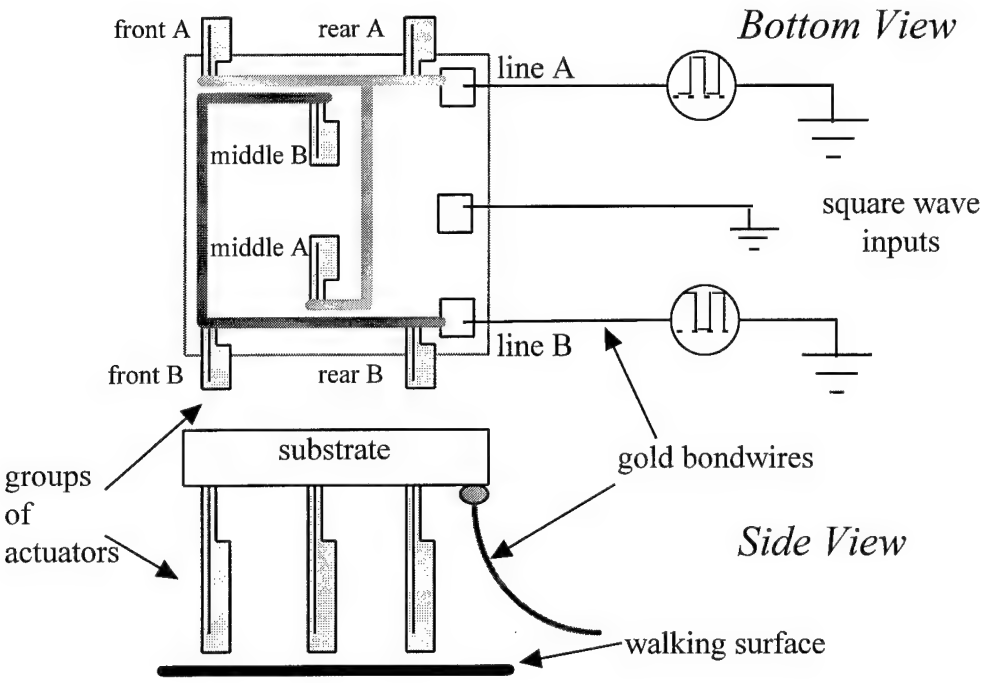

Figure 5-32: Simplified diagram of microrobot showing simplified wiring scheme with drive signal.

Some important factors considered in the design of this microrobot include determining the length of the legs, the number of legs needed to support the weight of the die, the method of self-assembling the leg, and the method of providing electrical power to the leg. These factors will be covered in detail after first introducing the leg system design.

Description of Microrobot Leg

Figure 5-33 shows a scanning electron micrograph of one leg used in the microrobot design. The robot leg is actually a poly1, horizontally deflecting, thermal

actuator connected to a poly2 on poly1 support base. The length of the leg alone is 230 μm plus the height of the support base, which is 40 μm tall -- 270 μm tall together. The leg is 2 μm thick, the narrow flexures of the leg are each 2.5 μm wide, and the wider portion of the leg is 16 μm wide.

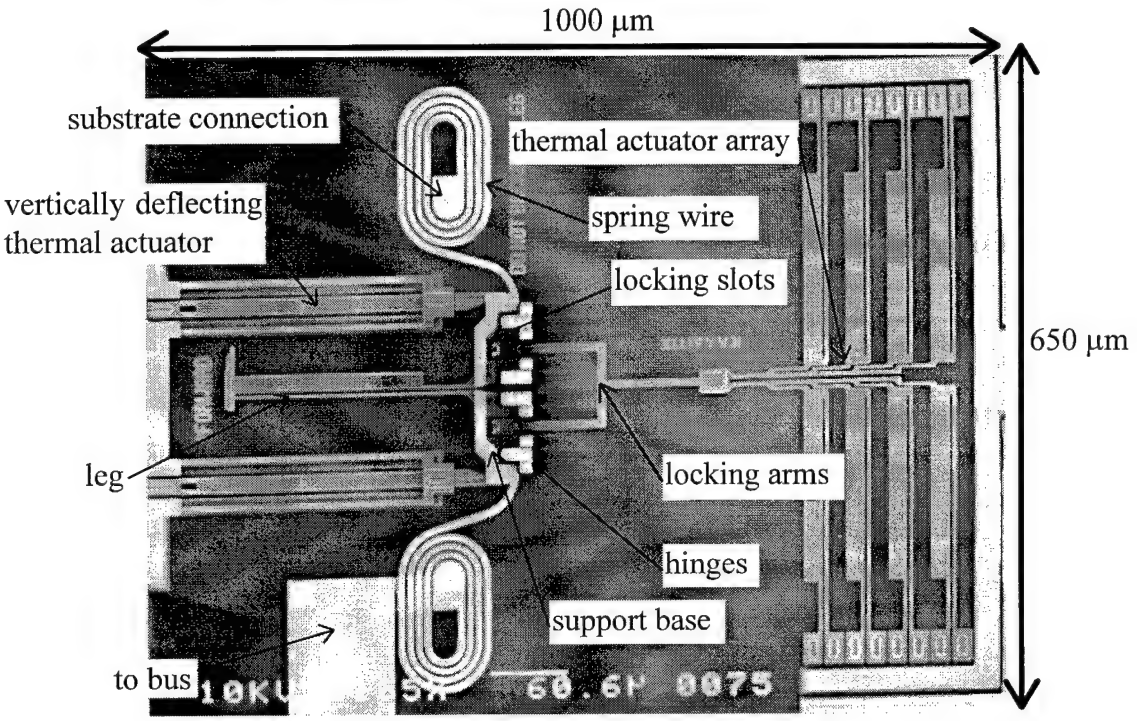

Figure 5-33: Scanning electron micrograph of one robot leg.

The support base is hinged at the bottom. Connected to either side of the support base are oval gold on poly2 spring wires. The spring wires provide power to the leg. With reference to Figure 5-33, the top spring wire is grounded to the substrate, and the bottom spring wire is supplied by a bus. The spring wires also flex to allow the leg and support base to be rotated to a normal to the substrate position. Positioned on either side of the support base are vertically deflecting thermal actuators. The vertically deflecting thermal

actuators are intended to lift the leg and base to their normal to the substrate position, after being back-bent. However, the vertically deflecting thermal actuators were not able to lift the leg and base, see Section 5.1 for details. All ninety-six legs were rotated into position manually using probes. Once the base is lifted to position, it locks onto the poly2 locking arms which are connected to the array of poly1 thermal actuators located to the right, in the micrograph. The array of thermal actuators is provided to demonstrate another degree of freedom of movement for the leg after assembling. Figure 5-34 shows a scanning electron micrograph of an assembled microrobot leg. Figure 5-35 shows another view of the leg from the opposite side than that of Figure 5-34. Figure 5-36 is a closer view of the foot. Figure 5-37 is a scanning electron micrograph of close views of the microrobot's leg base and locking arms, viewed from the front (a) and back (b).

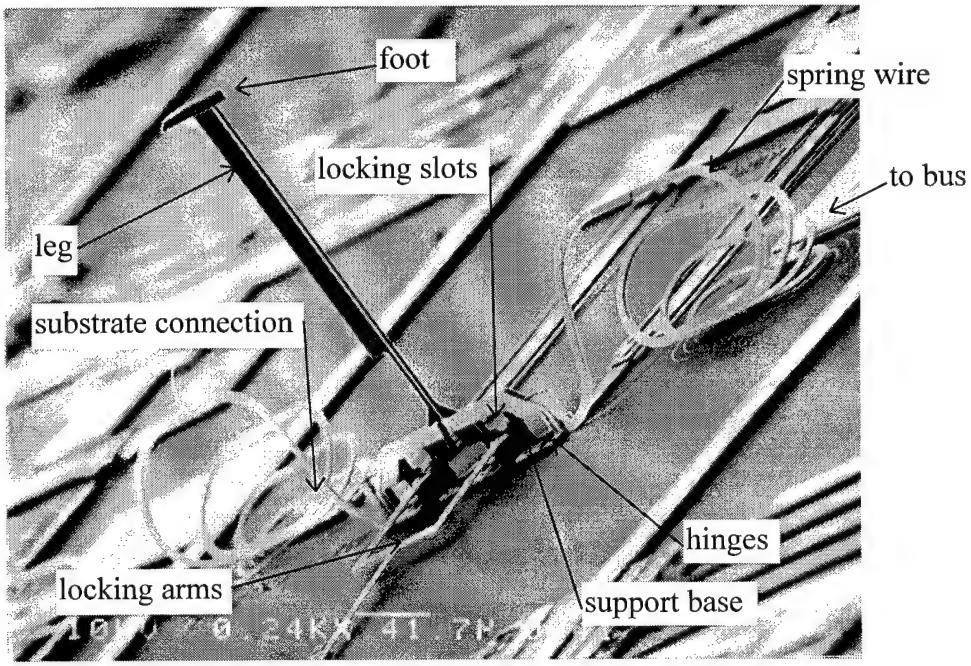

Figure 5-34: Scanning electron micrograph of one assembled microrobot leg.

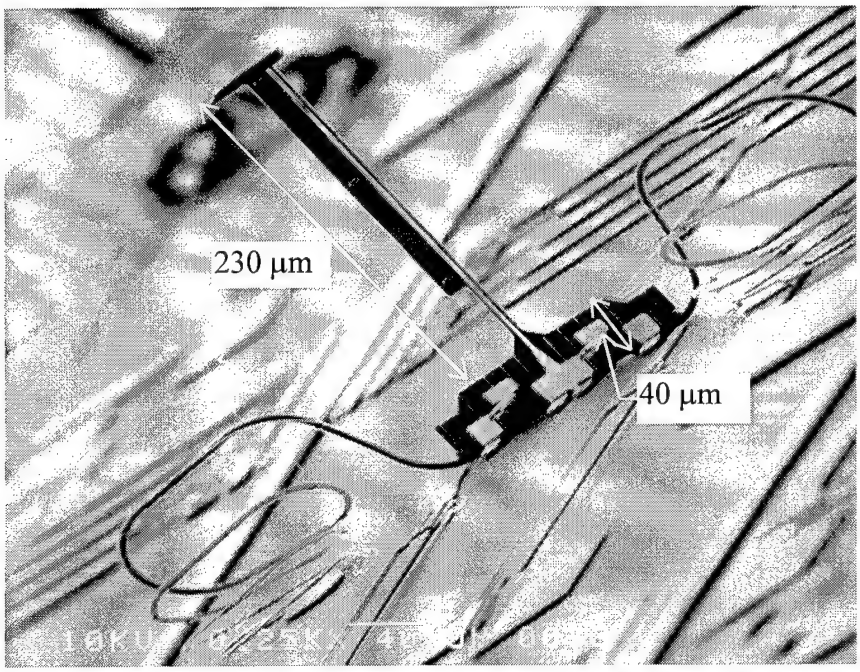

Figure 5-35: Scanning electron micrograph of a microrobot leg. This view is from the opposite side than that of Figure 5-34.

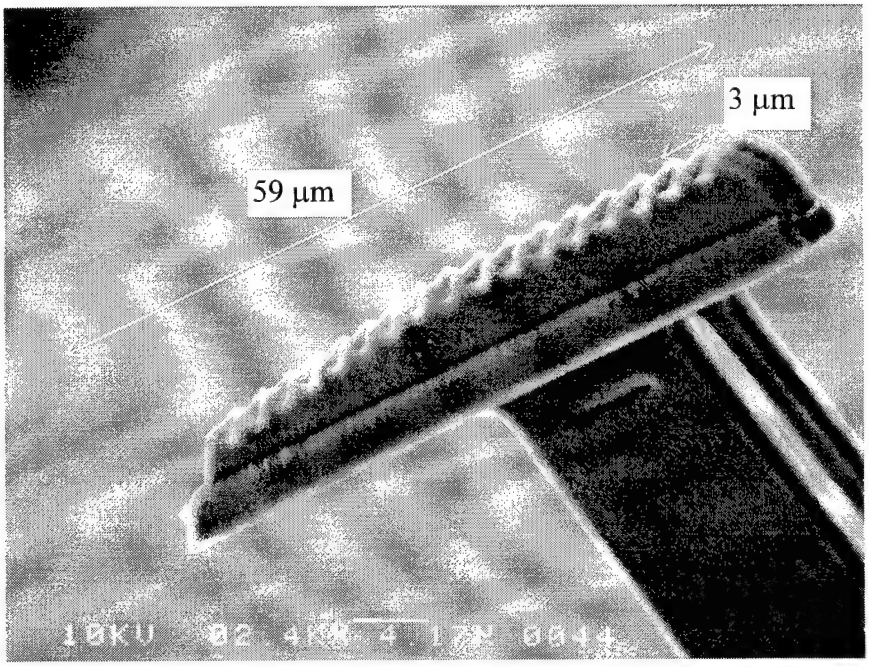

Figure 5-36: Scanning electron micrograph of microrobot's foot.

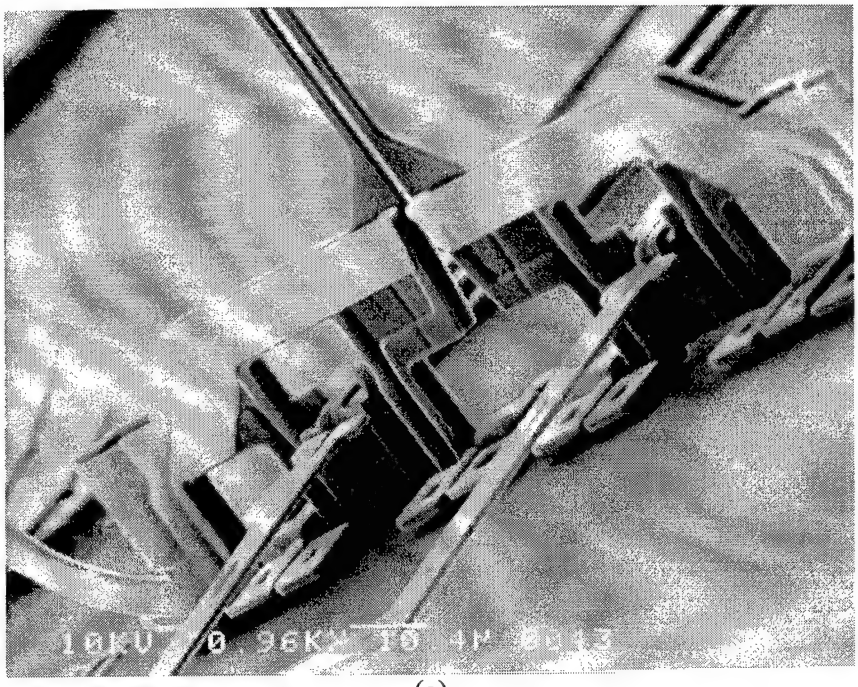

(a)

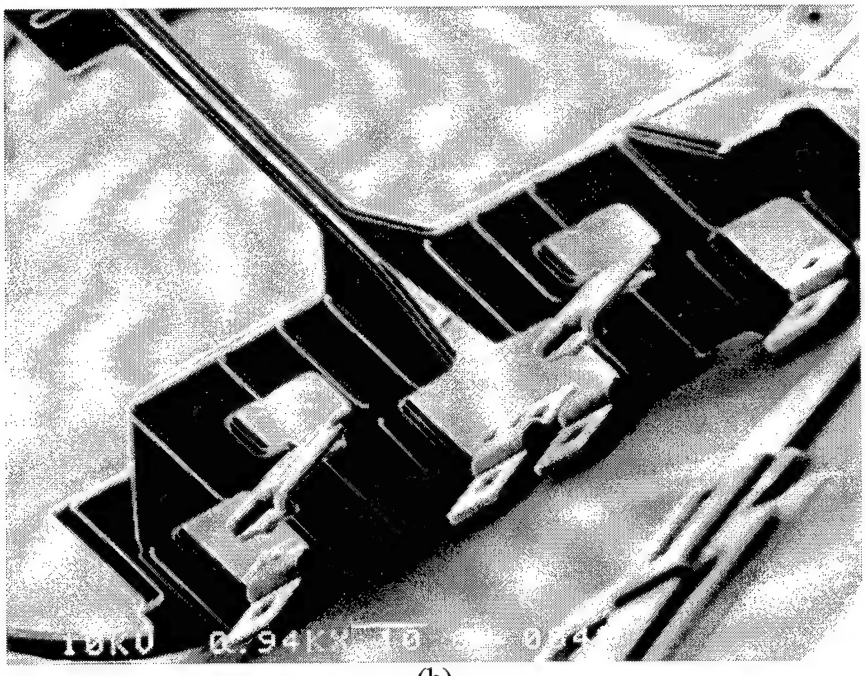

(b)

Figure 5-37: Scanning electron micrograph of close views of the microrobot's leg base and locking arms, viewed from the front (a) and back (b).

The leg thermal actuator is chosen because of its standard usage at AFIT and its proven design. Comtois and Bright, report that this thermal actuator can produce a force of 4.4 μN and unloaded deflection of 16 μm at the tip, while supplied by 3.68 mA at 2.94 V [7]. The authors also report that a single actuator will operate at maximum deflection up to 300 Hz. From this information, it can be predicted that the microrobot can move at a velocity of at most, 16 μm x 2 x 300 Hz = 9600 μm/second = 9.6 mm/second.

Determination of Microrobot Leg Length

The length of the robot leg was chosen as follows. Since the microrobot's thermal actuator legs will be powered externally through wires connected to the substrate by wirebonder ball bonds, the height of the ball bonds will dictate the length of the legs. The height of a ball bond can be determined from Figure 5-38, which is a scanning electron micrograph of two ball bonds.

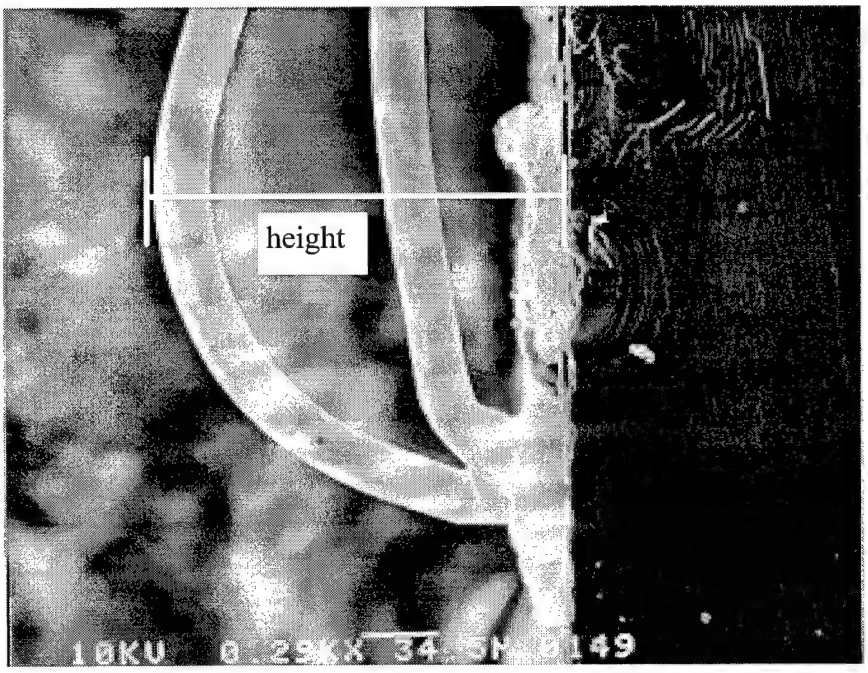

Figure 5-38: Scanning electron micrograph of two wirebonded ball bonds.

The shorter loop height bond was made using a low loop height setting on the wirebonder and is connected to a nearby gold pad. The taller loop height bond was made using a

high loop height and is connected to a distant gold pad. The loop height of the taller bond is dictated by the sag due to the wire's own weight. The loop height of the taller bond can be taken as the worst case height, and this height is estimated from Figure 5-38 as approximately 189.75 μm. The length of the legs must be greater than 189.75 μm. A scanning electron micrograph from another perspective of the same wire bonds is shown in Figure 5-39.

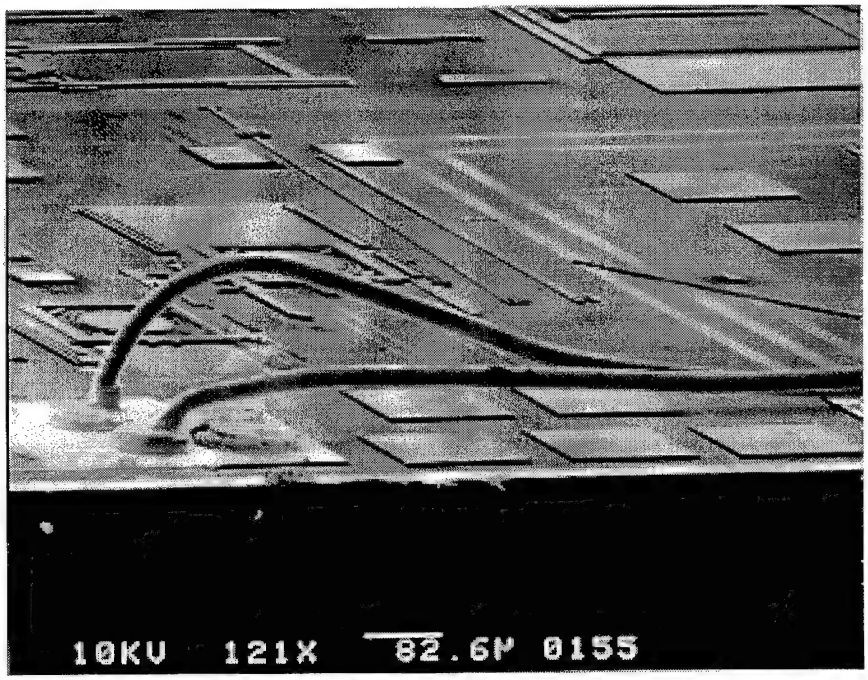

Figure 5-39: Different perspective scanning electron micrograph of ball bonds from Figure 5-38.

The length of the leg is 230 μm plus the height of the base, which is 40 μm. Therefor, it can be predicted that clearance of the ball bonds will not be a hindrance. Furthermore, if the power supply wires drag behind the microrobot, this could be useful

as stabilization, similar to a cockroach dragging its carcass as it scurries across the floor.

Determination of the Number of Legs Needed for the Microrobot

The number of legs needed to support the die can be predicted by calculating the weight one leg can support and then comparing that to the weight of the die. One leg can be modeled by a polysilicon column fixed at one end and free to move at the other. The column has a length *l*, cross sectional area *ab*, and a force *F* applied to the free end as shown in Figure 5-40.

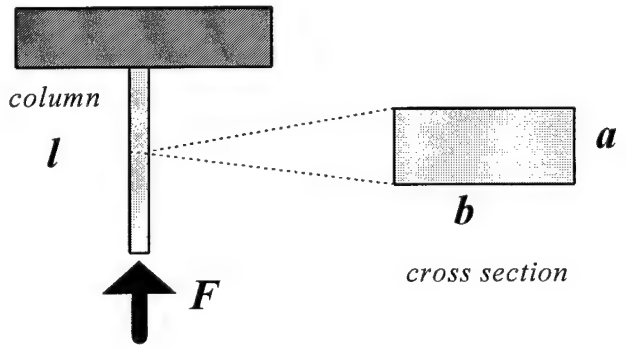

Figure 5-40: Column model of robot leg with length *l*, cross sectional area *ab*, and a force *F* applied to the free end.

The force necessary for causing the beam to fail from compression or fail from buckling can be estimated. The smaller of the two estimated forces will be taken as the weight one leg can support, and that force will be compared to the weight of the die.

Assuming that the compressive strength, S_c, is approximately the same as the tensile strength, S_t, a conservative estimate for the force, F_{CF}, causing a compressive

failure is:

$$F_{CF} = abS_c = abS_t \tag{1}$$

For a buckling failure, we can use Euler's column equation, Eq. (2), or J. B. Johnson's column equation, Eq. (3), to estimate the force, F_{BF}, necessary to cause a buckling failure [8]:

$$F_{BF} = \frac{C\pi^2 EI}{l^2} \tag{2}$$

$$F_{BF} = ab\left(S_Y - \left(\frac{S_Y l}{2\pi k}\right)^2 \frac{1}{CE}\right) \tag{3}$$

Where C is an end condition constant, 0.25, in this case; E is Young's Modulus; I is the area moment of inertia of the column, and for this case is

$$I = \frac{1}{12}ba^3 \tag{4}$$

k is the radius of gyration of the column, and for this case is

$$k = \sqrt{\frac{a^2}{12}} \tag{5}$$

and S_Y is the yield strength. To determine which equation to use, the following inequality must be checked:

$$\frac{l}{k} \geq \sqrt{\frac{2\pi^2 CE}{S_Y}}. \tag{6}$$

The quantity, l/k, is referred to as the slenderness ratio. If the inequality in Eq. (6) is true, then we can use Euler's column equation, otherwise, use J. B. Johnson's column equation.

Let us assume that the thick and corrugated poly1-poly2 leg base will not fail from buckling and that it is securely fixed in its normal to the substrate position. Therefor, we can neglect the base and just consider the buckling of the leg. Let us also assume that the leg is the width of its two flexures (2.5 μm + 2.5 μm). More appropriately, a leg could be modeled as two columns, each of the width of the flexure. Either way, however, the result will be the same -- the leg will be modeled as one component for the sake of keeping the presentation simple. Three fourths of the leg is actually 18.5 μm wide, but let us assume that its width is dictated by its weakest point at the flexures. For the poly1 thermal actuator, let the variables from above be assigned the following values:

$a =$ 2 μm, the nominal thickness of the poly1 layer.

$b =$ 2 x 2.5 μm = 5 μm, the width of two thermal actuator flexures considered together.

$l =$ 230 μm, tall enough to clear the wire bond loop.

$E =$ 169 GPa [3].

$S_Y = S_c = S_t =$ 1.2 GPa [3].

From Eq. (1), the maximum force one leg can withstand, before a compressive failure, is estimated as F_{CF} = 12 mN. By evaluating the inequality in Eq. (6), we can estimate the maximum force one leg can withstand, before a buckling failure, from Eq. (2). This force is estimated as F_{BF} = 26.2754 μN. Comparing F_{BF} to F_{CF} shows that F_{BF} is smaller indicating that the leg would be expected to fail from buckling and not compression.

The weight of a 1 cm x 1 cm die, assuming a die thickness of 550 μm, silicon

density of 2330 kg/m^3, and acceleration due to gravity 9.8 m/s^2, is 1255.87 μN. Comparing the weight of the die to F_{BF} we see that, approximately, 48 legs are needed to support the weight of the die.

At this point, it is important to explain that the result for F_{BF} is a prediction of a point of unstable equilibrium [8]. In other words, this number of legs will only support the weight of the die or load (assuming the material properties used in the calculation are exact) if: every leg is exactly perpendicular to the load and the walking surface; the die is magically placed on the walking surface such that no shifting of the leg or load occurs; and there is no shifting of, disturbance of, or applied force to the load. Some factor of safety should be multiplied times the number of legs, at least to obtain a stable static equilibrium, and an even greater factor of safety to obtain dynamic stability. Only experience can determine the factor of safety to be used.

For this microrobot, 2 x 48 = 96 legs are used to support the weight of the die. Regardless of the above result and unfortunately, 96 turns out to be the maximum number of legs that could be arranged onto the die using the design in Figure 5-33. A factor of safety of at least 10 would have been desired for dynamic stability.

Microrobot Chip Layout and Wiring Design

This section will describe the layout of the microrobot and the design behind the wiring. Figure 5-41 shows a CADENCE drawing of the microrobot chip showing the 96 legs and main wiring buses. Also contained on the chip are miscellaneous test structures.

Figure 5-42 is the same as Figure 5-41, except the view is one level back in cell design hierarchy. This view more clearly reveals the six groups of robot legs discussed in Section 5.4 and main wiring buses. Three groups are connected in parallel on one bus, and the other three are connected in parallel on a separate bus. The two separate circuits "A" and "B" are labeled in Figure 5-42 as front A, middle A, and rear A; and front B, middle B, and rear B.

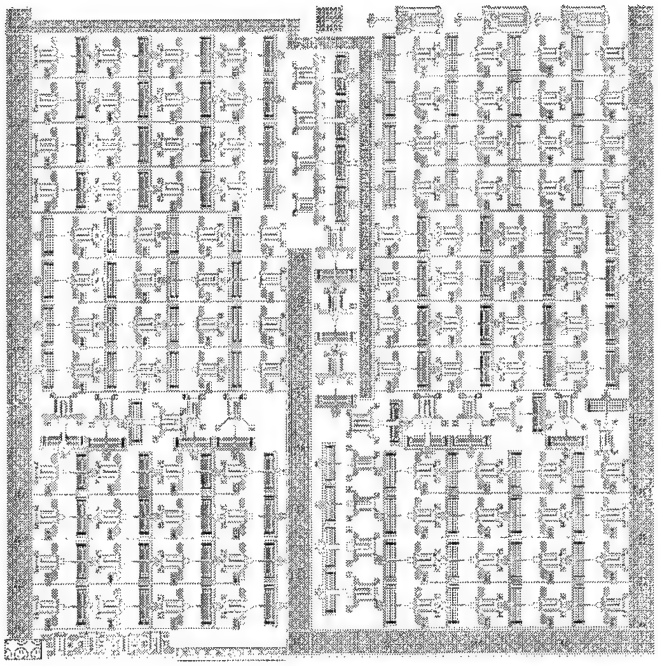

Figure 5-41: CADENCE drawing of the microrobot chip showing the 96 legs and main wiring buses.

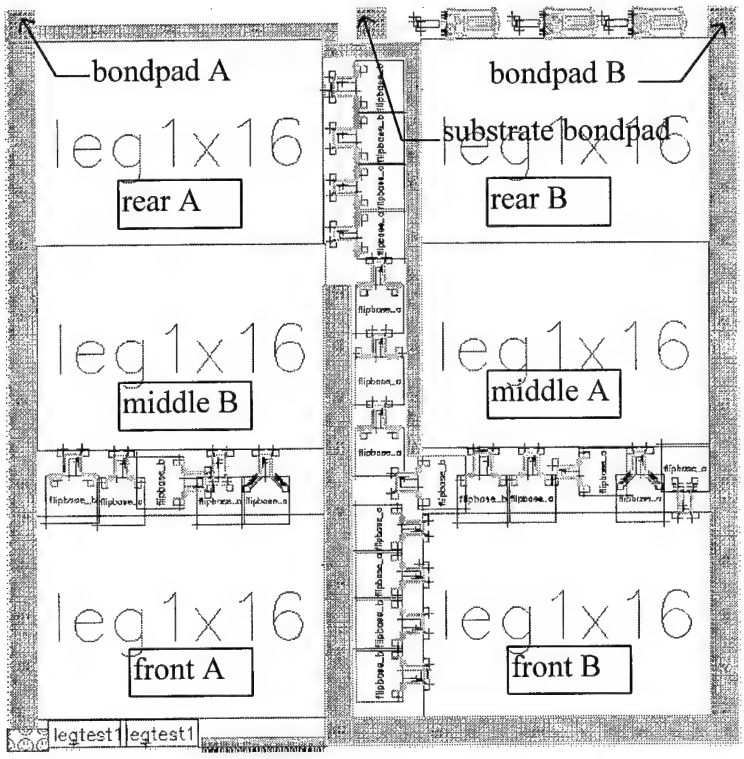

Figure 5-42: CADENCE drawing of the microrobot chip, one level back in the cell design hierarchy, revealing the six groups of robot legs and main wiring buses.

All of the individual legs are grounded to the substrate. The width of the buses are made as large as possible while still providing enough room for test structures. The buses are made from poly1, poly2, and gold, and are anchored to the substrate periodically with posts that are anchored to poly0. As large a gap as possible is desired between the substrate and the main buses to reduce parasitic capacitance. Parasitic capacitance could result in the loss of operational bandwidth. The gold cross sectional area of the main buses (400 μm × 0.5 μm) are half the cross sectional area of the gold bondwire (pi × (25/2 μm)^2). The width, lengths, and paths of the main buses were carefully designed so that the same resistance is encountered between the front groups, the middle groups, or the

rear groups of actuators. Figure 5-43 shows one of the six groups of robot legs. Four smaller buses that supply four individual legs are shown. The smaller buses are made from poly1, poly2, and gold. Overall, the main concern, in the design of the wiring, was ensuring that the resistances to the individual legs or groups are symmetric between group A and B.

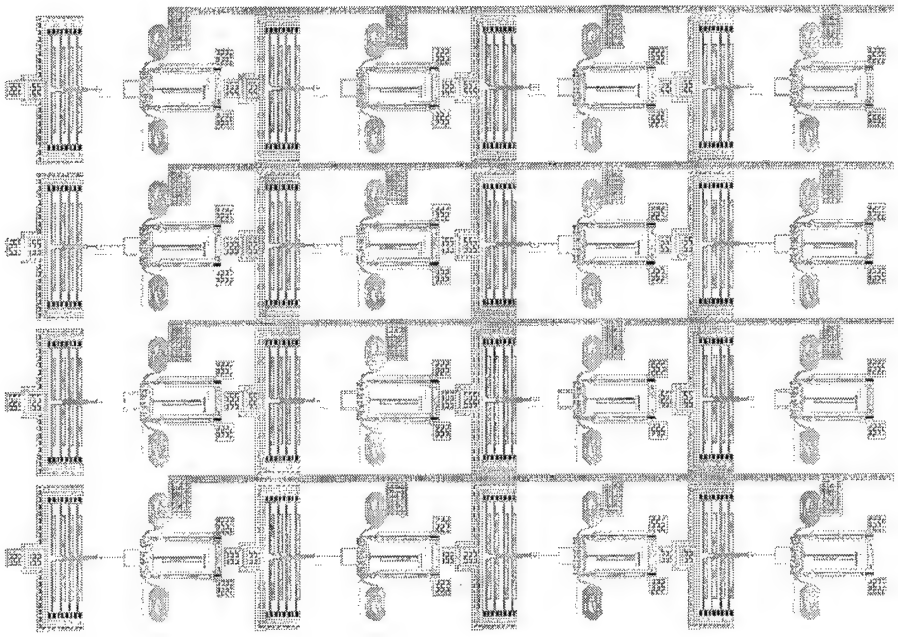

Figure 5-43: CADENCE drawing of one of the six groups of robot legs.

Figure 5-44 is a scanning electron micrograph of the microrobot, looking down on the micromachined side where the legs are. Dashed white lines demark the approximate locations of the six groups of legs. "Bondpad A" supplies the "rear," "middle," and "front A" groups, and likewise "bondpad B." Figure 5-45 is a scanning electron micrograph of three assembled microrobot legs. Figure 5-46, Figure 5-47 and Figure 5-48 are "zoomed out" views showing more legs, and with the "front A" group foremost in view.

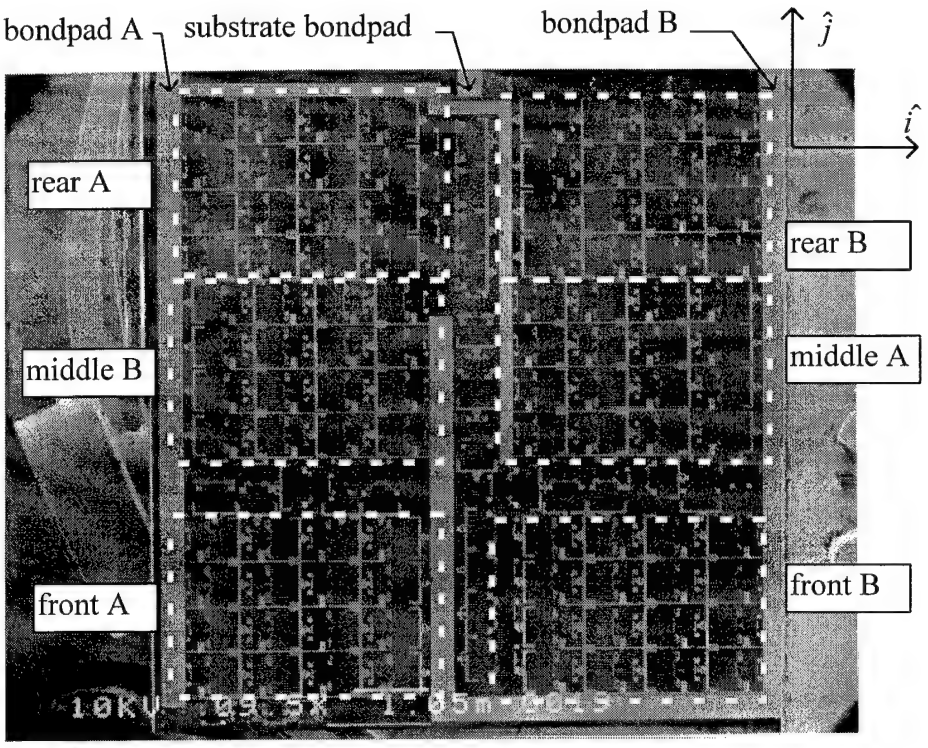

Figure 5-44: Scanning electron micrograph of the microrobot showing groups of legs on the "A" and "B" circuits and reference orientation.

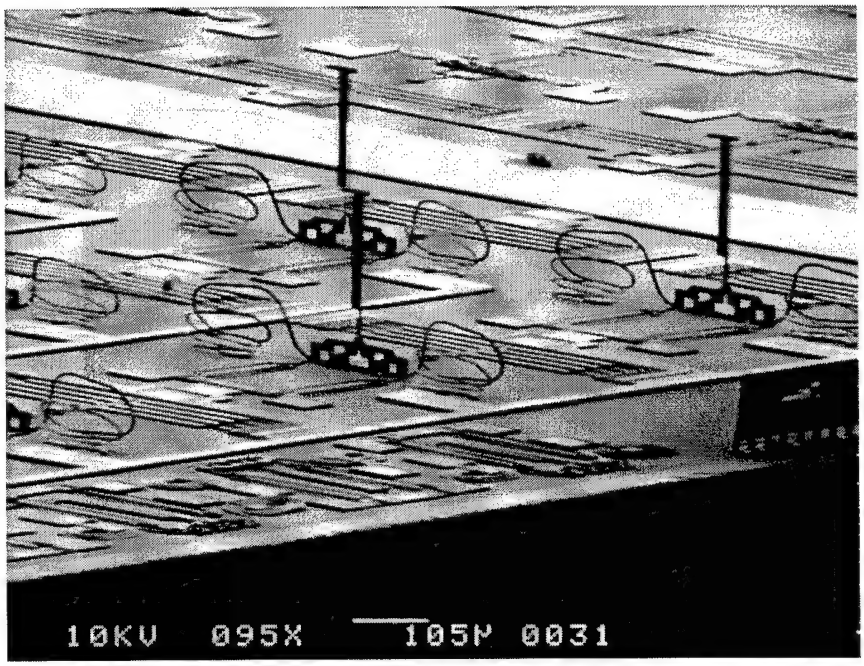

Figure 5-45: Scanning electron micrograph of three assembled microrobot legs.

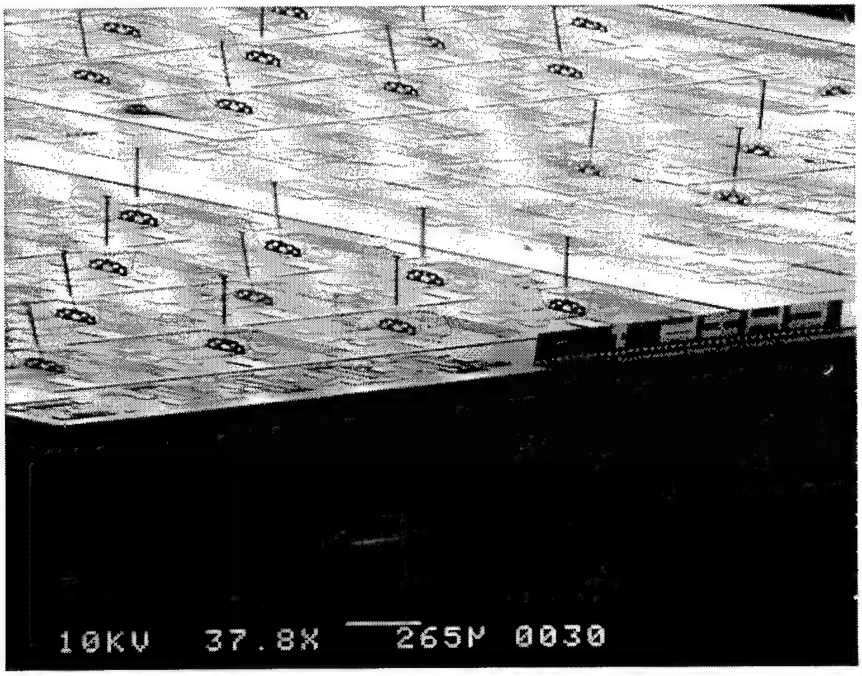

Figure 5-46: Scanning electron micrograph of the microrobot with the "front A" group closest in view.

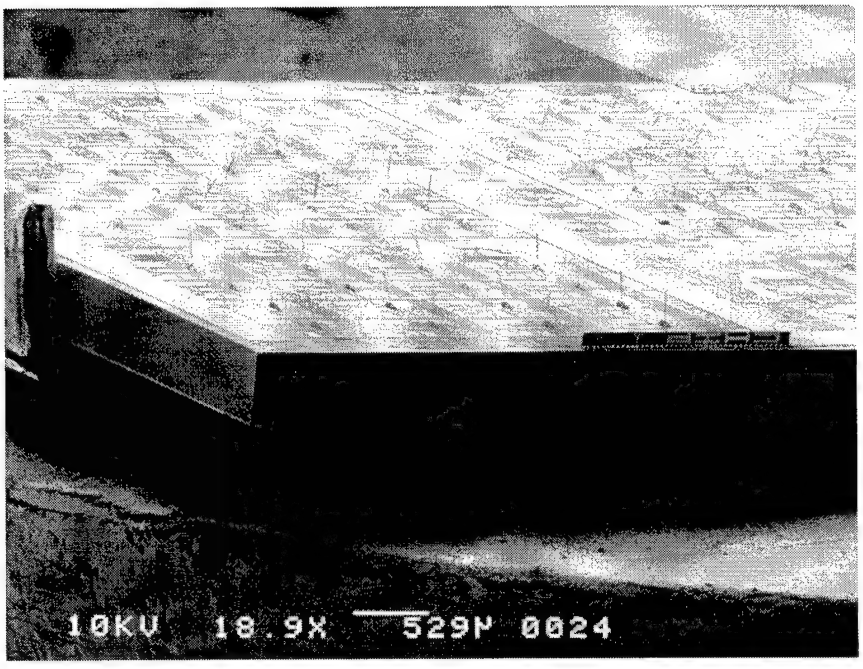

Figure 5-47: Scanning electron micrograph of the microrobot with the "front A" group closest in view (farther away view).

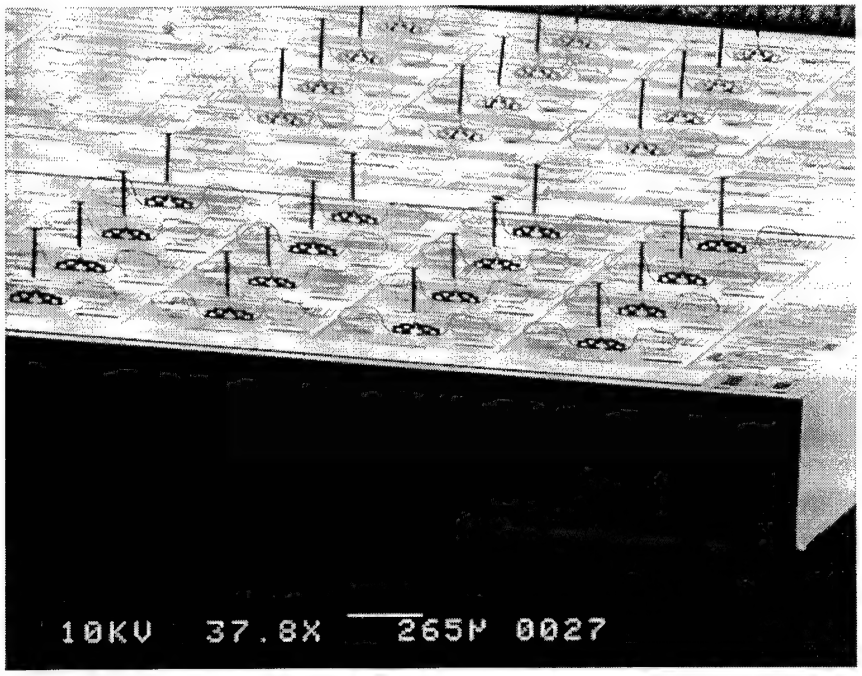

Figure 5-48: Scanning electron micrograph of a rotated view of the microrobot with the "front A" group, again, closest in view.

Microrobot Experiment and Results

The sequence of events used to prepare a microrobot for testing is as follows. Please refer to Chapter 4 for a detailed description of the experimental setup and the microrobot positioner.

1) Release a MUMPs 20 die according to the release process described in Chapter 3.
2) Erect all 96 microrobot legs, using probes, at the probe station. This procedure typically takes about 3 hours.
3) Remove the microrobot positioning arm from the microrobot positioner.

Carefully place the microrobot on the end of the microrobot positioning arm, over the vacuum hole, and secure into place using the mechanical hold down devices.

4) Place the microrobot positioning arm with microrobot (legs up) on the stage of the wirebonder, and connect a wire from each of the three pads of the microrobot to a corresponding pad on the PC board that is connected to the positioning arm. Be sure to provide at least a centimeter of slack in each wire.
5) Reattach the microrobot positioning arm to the microrobot positioner. And turn on the vacuum pump.
6) Remove the mechanical hold down devices from the microrobot positioning arm. The microrobot will remain connected to the microrobot positioner by vacuum.
7) The end of the microrobot legs can be viewed on a monitor connected to a video camera with a 50× zoom lens. The reflection of the legs on the walking surface can also be seen. Lower the microrobot until the legs meet their reflections.
8) Turn off the vacuum using the valve, or simply switch off the power supply to the vacuum pump. The microrobot is now released from the microrobot positioning arm.
9) Lift the positioning arm away from the microrobot. Also, move the positioning arm forward over the microrobot to provide more slack in the wires that are connected to the microrobot.

10) Turn on power supply for the robot leg circuits.

Figure 5-49 shows the microrobot after being released from the microrobot positioning arm onto the polyimide coated wafer or walking surface.

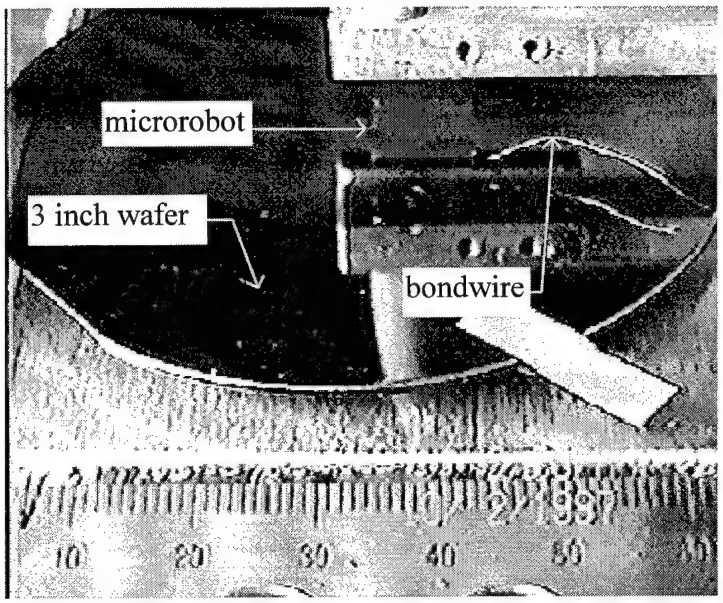

Figure 5-49: Video image of the microrobot after being placed, legs down, on a 3 inch polyimide coated wafer. Ruler scale is in millimeters.

In one test, a microrobot was prepared and released onto the walking surface as described above. However, the legs could not support the weight of the die and collapsed. The mass of the die was measured, and found to be 127.50 mg ± 0.01 mg. Some reasons for the failure of the legs are as follows:

1) The legs are not perpendicular to the die after assembly. The thermal actuator array that holds the leg and base in an upright position, flexes, allowing the leg to be angled instead of normal with the substrate. Figure 5-50 shows an

example of this non-normal and flexing condition.

2) There may be too few legs to support the weight of the die. As discussed earlier in this section, the number of legs are probably too few to be dynamically robust.

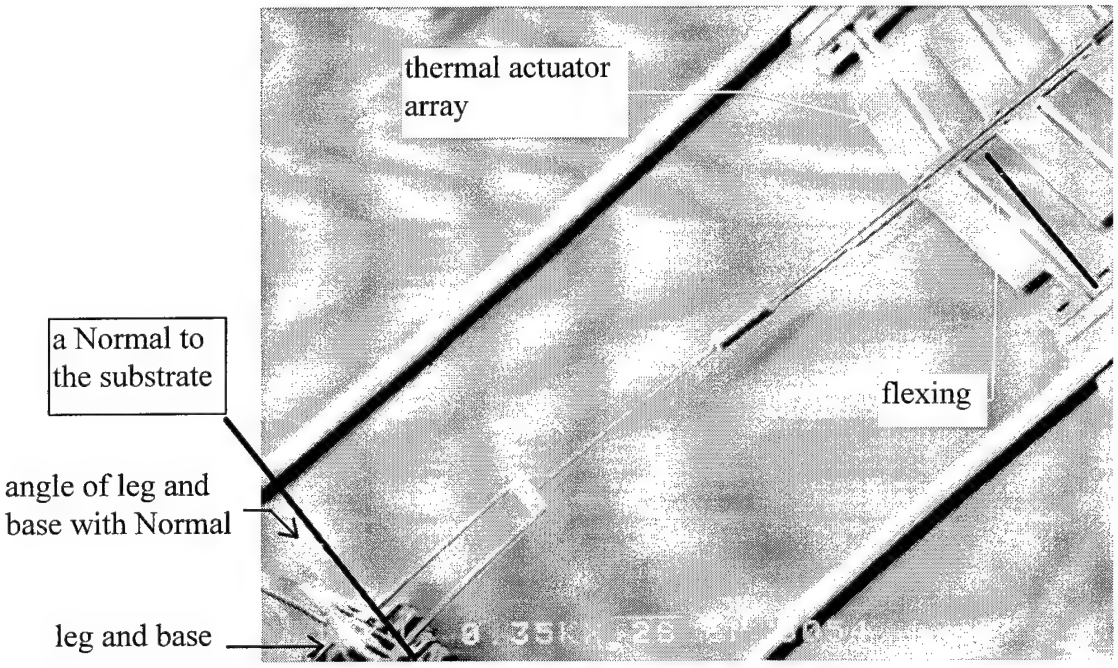

Figure 5-50: Scanning electron micrograph showing the thermal actuator array flexing allowing the microrobot leg to be angled instead of perpendicular to the substrate.

The microrobot was retrieved from the walking surface by simply turning on the vacuum and positioning the microrobot positioning arm over the microrobot and lowering. When the positioning arm is within 3 or 4 millimeters of the microrobot, the microrobot is suctioned up to the positioning arm. Figure 5-51 shows a scanning electron micrograph of the microrobot after retrieval from the walking surface. After analyzing

the microrobot, only three types of damage to the microrobot leg system were observed:

1) One flexure of the robot leg is broken, and no other damage. An example of this damage is shown in Figure 5-52.
2) The leg has broken completely off, leaving the cold arm flexure and part of the hot arm flexure, and no other damage. An example of this damage is shown in Figure 5-53.
3) The leg has broken completely off, leaving the cold arm flexure and part of the hot arm flexure. Also, one side of the base has unhooked from the locking arms or one of the two locking tabs has broken off of a locking arm. An example of this damage is shown in Figure 5-54

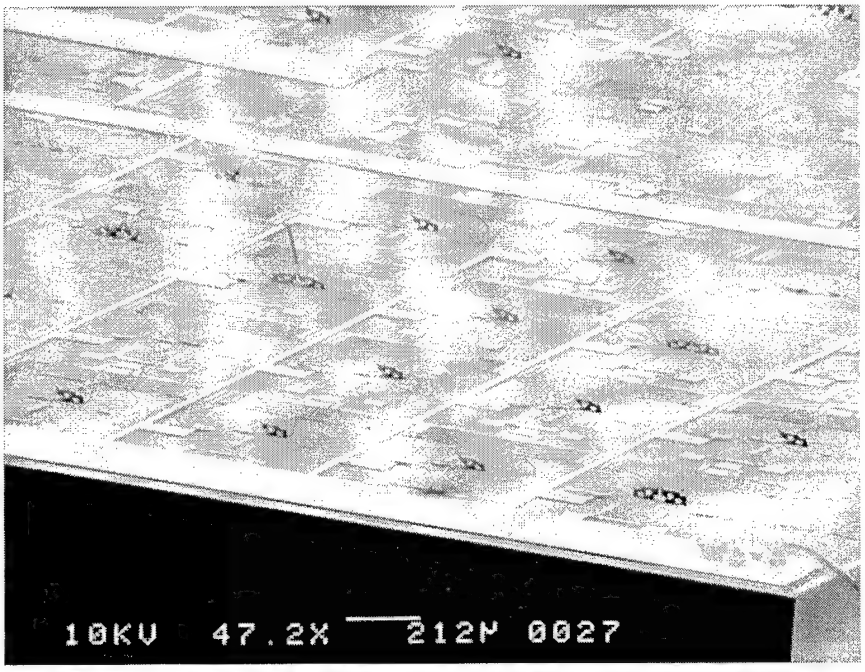

Figure 5-51: Scanning electron micrograph of a corner view of the collapsed microrobot showing a wire bond and some damaged legs.

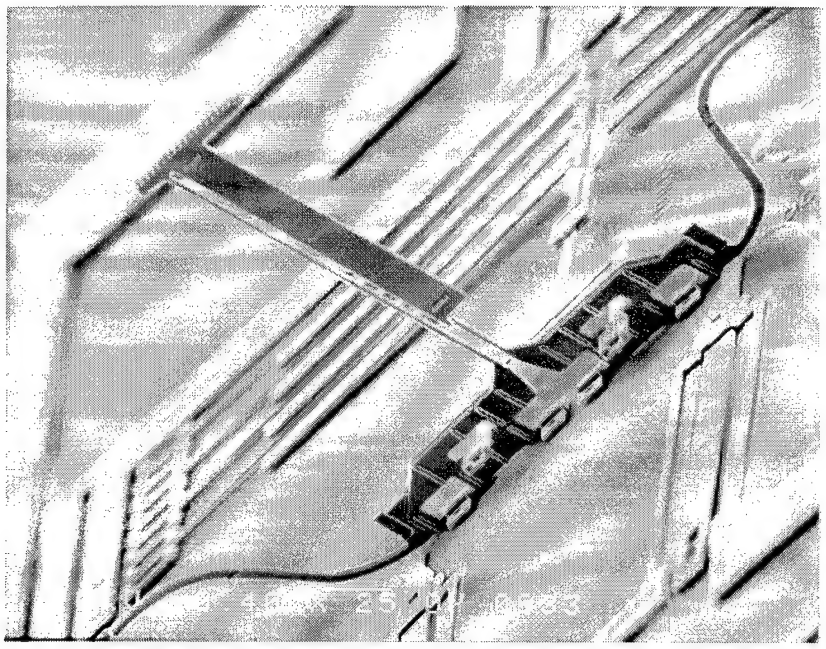

Figure 5-52 Scanning electron micrograph of one type of damage to a microrobot leg system, where the only damage is one flexure of the leg is broken.

Figure 5-53: Scanning electron micrograph of the second type of damage to a microrobot leg system, where the only damage is that the leg has broken completely off, leaving the cold arm flexure and part of the hot arm flexure.

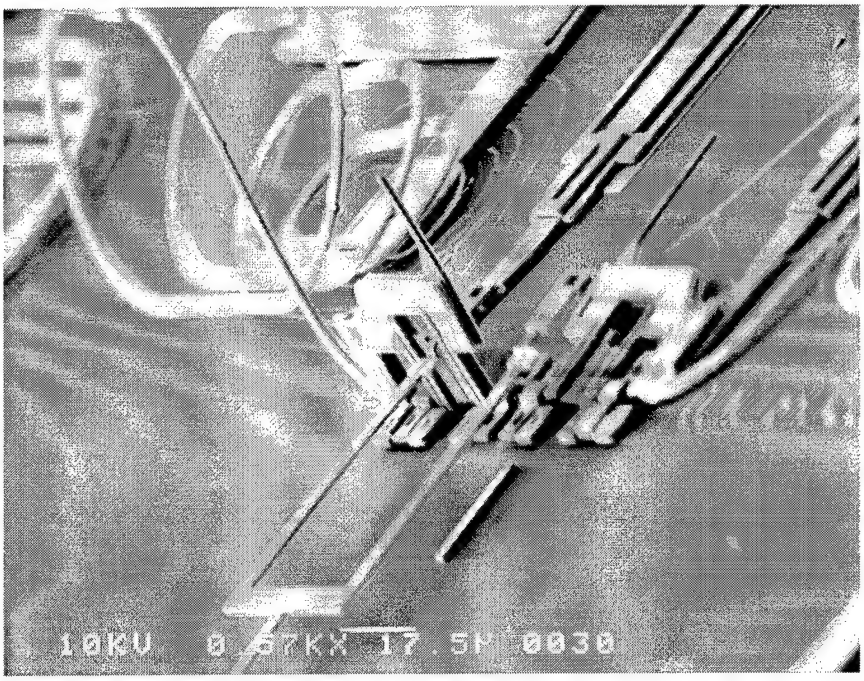

Figure 5-54: Scanning electron micrograph of the third type of damage to a microrobot leg system, where the only damage is that the leg has broken completely off, leaving the cold arm flexure and part of the hot arm flexure. Also, one side of the base has unhooked from the locking arms or one of the two locking tabs has broken off of a locking arm.

In another test, the mass of a microrobot was reduced to 37.32 mg ± 0.01 mg, by mechanically lapping approximately 75 % of the silicon off of the back of the chip. The die was lapped as described in Chapter 4, and prepared as described for the previous experiment. Figure 5-55 shows a scanning electron micrograph of the lapped microrobot.

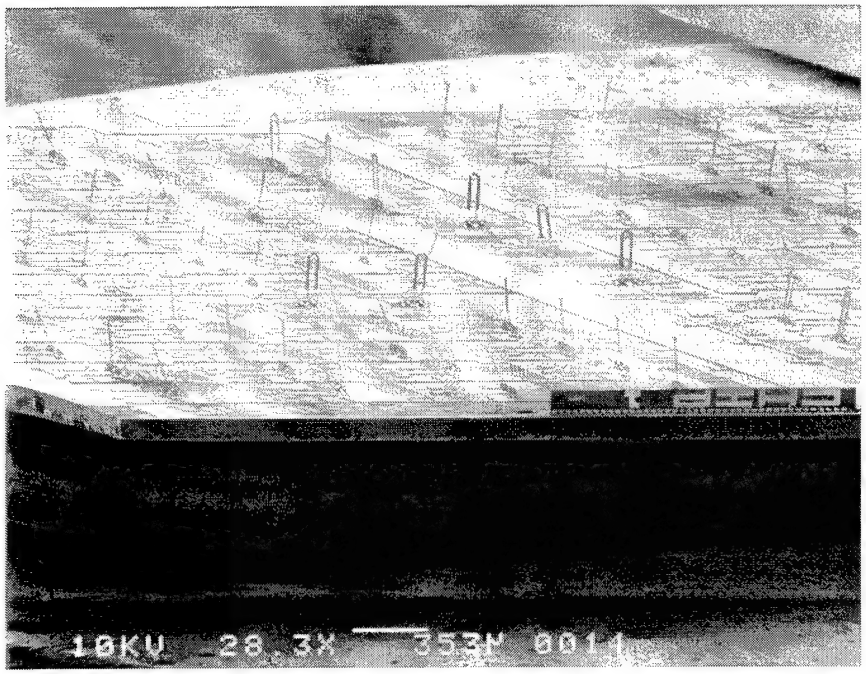

Figure 5-55: Scanning electron micrograph of an assembled microrobot that has been lapped to a quarter of its original thickness.

Figure 5-56 shows the lapped die as it is being lowered toward the walking surface. The legs were able to support the weight of the die, however, somewhat unstable. An attached bondwire recoiled shortly after releasing the microrobot, causing the robot to shift and collapse the legs at one corner. Afterwards, movement of the microrobot was not observed while powering the legs. The freestanding microrobot, before collapsing, is shown on a captured video image in Figure 5-57.

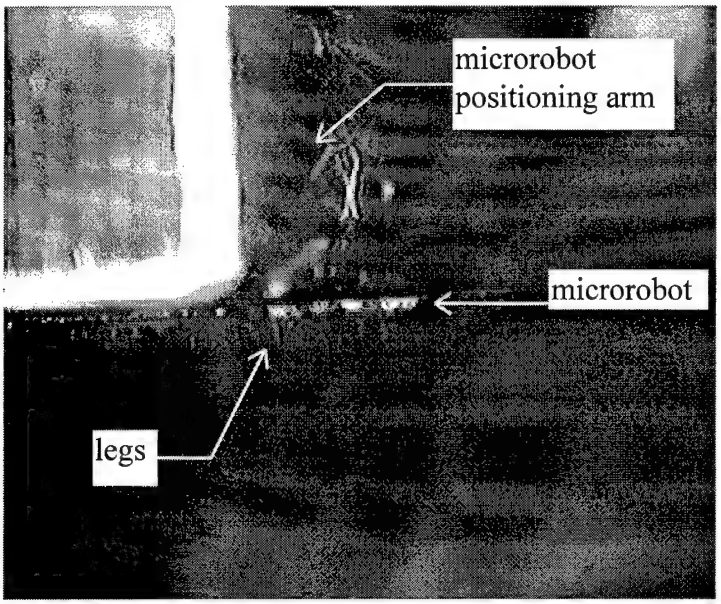

Figure 5-56: Captured video image of the lapped microrobot, held in place by vacuum on the microrobot positioning arm, while being lowered to the walking surface.

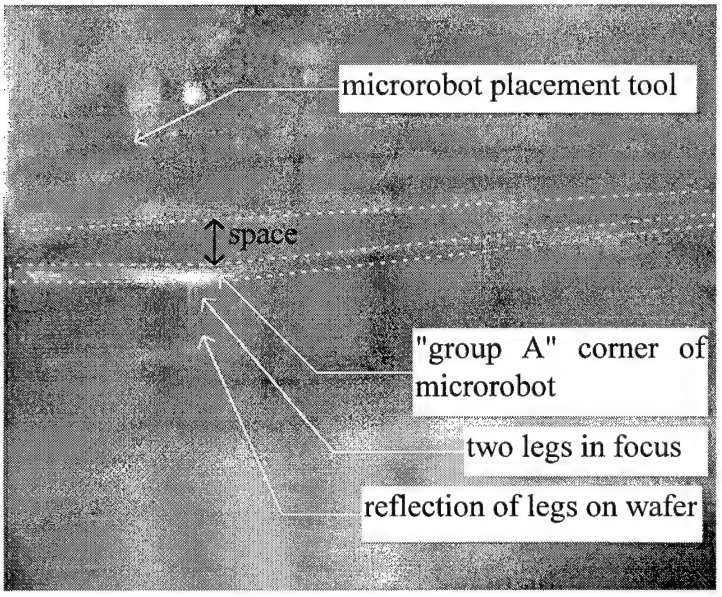

Figure 5-57: Captured video image of the freestanding microrobot. Dashed lines added to help distinguish between the microrobot chip and the placement tool.

To prove that the leg arrangement could cause movement, another robot was tested, belly side up at a probe station. The leg circuitry was powered through probes. A piece of kapton, 9.25 mm by 9 mm by 0.023 mm thick with a mass of 3.06 mg ± 0.01 mg, was placed, using tweezers, on top of the legs. The following results are given with reference to the $\hat{i}$ and $\hat{j}$ reference axes shown in Figure 5-44. The legs were able to transport the piece of kapton with an average vector velocity of $-446\hat{i} + 77\hat{j}$ μm/minute or with a magnitude of 453 μm/minute while being powered by a 0-5 volt square wave with a 50 % duty cycle at approximately 2 Hz. Assuming the kapton was moved with every step of the legs, the average minimum step size is:

$$(-446\hat{i} + 77\hat{j} \text{ μm/minute}) \div 120 \text{ steps/minute} = -3.7\hat{i} + 0.6\hat{j} \text{ μm/step.}$$

Figure 5-58 shows a video image of the initial position of the kapton. Also shown in Figure 5-58 are the reference axes, $\hat{i}$ and $\hat{j}$. Figure 5-59 shows the same image 3 minutes later after the kapton has been transported across the die by the microrobot legs. A defect in the kapton film served as a reference mark to track the kapton's motion.

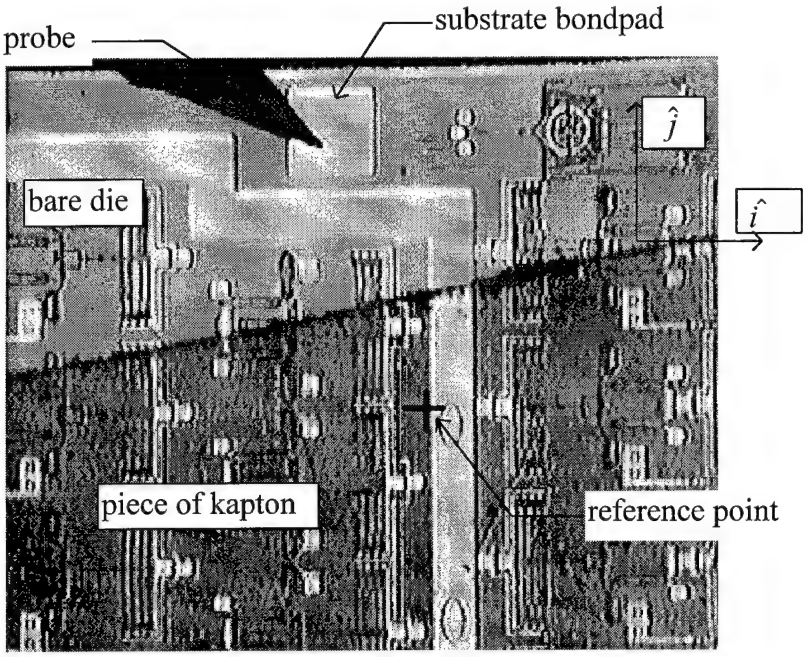

Figure 5-58: Captured video image of a piece of kapton that has been placed on the microrobot's legs.

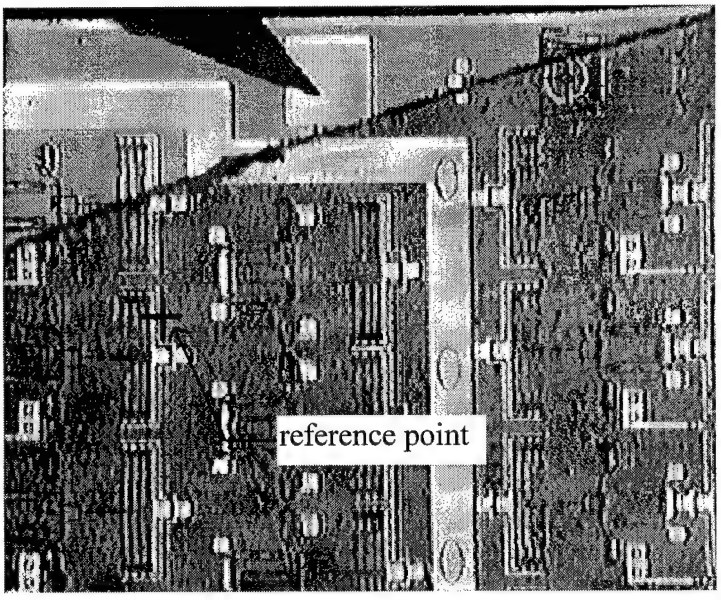

Figure 5-59: Captured video image of the same piece of kapton in Figure 5-58 after being transported across the die by the microrobot legs.

A maximum operating frequency of approximately 2.2 Hz was determined by trial

and error. Frequencies faster than this resulted in the microrobot's feet slipping on the kapton instead of transporting it. It is suspected that a heavier object would be able to be transported at higher operating frequencies, because the frictional force between the feet and the material would be greater. Each leg circuit can be operated at a maximum dc input voltage of 10 volts while drawing 287 mA, however, the lower 5 volt input, stated above, seemed to transport the kapton the best. The microrobot's legs were arranged and designed to cause motion in the $\hat{j}$ direction only, see the reference axes in Figure 5-44 or Figure 5-58. However, because of the non-flatness of the piece of kapton, the "A" circuit legs were able to grab and push the kapton better than the "B" circuit legs. The "B" circuit legs were observed to grab the kapton during their operating phase, but not shift the kapton.

The "A" circuit legs are undesirably angled toward the $-\hat{i}$ direction, and the "B" circuit legs are undesirably angled toward the $\hat{i}$ direction. Because the legs are not perpendicular to the substrate, a majority of the thermal actuator leg's motion is translated in the $\pm\hat{i}$ direction, instead of the $\hat{j}$ direction. If the legs were perpendicular to the substrate, a greater step size in the $\hat{j}$ direction could be expected. Also, a smaller, perhaps negligible, step size in the $\pm\hat{i}$ direction would be found.

An improved version of the microrobot was designed in the MUMPs 21 fabrication run. A CADENCE drawing of this microrobot is shown in Figure 5-60.

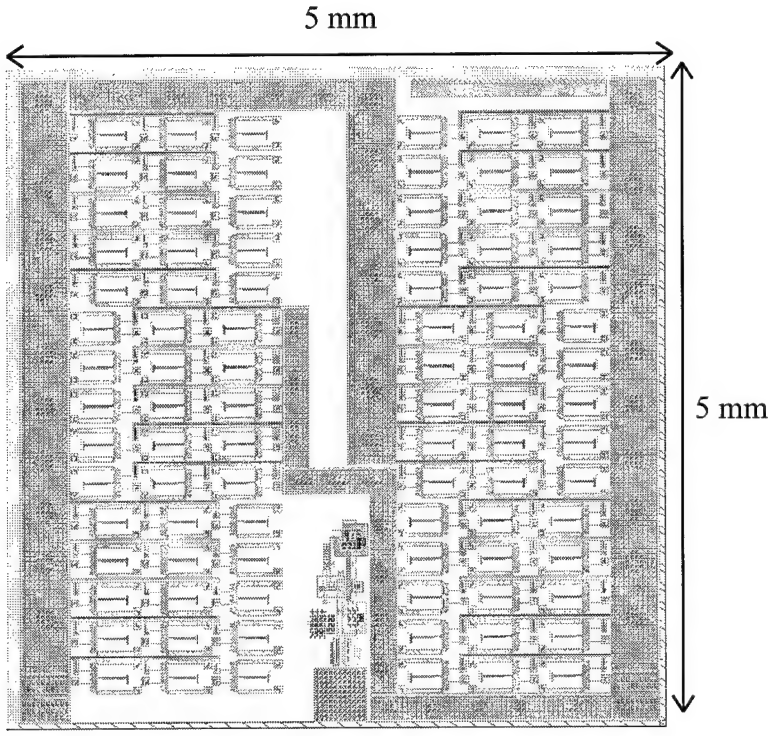

Figure 5-60: CADENCE drawing of a new version of microrobot designed for the MUMPs 21 fabrication run.

The dimensions of the this robot are 0.5 cm by 0.5 cm by 0.55 mm. The wiring design and wire widths are the same as used for the microrobot presented in the previous section, however, this microrobot is a quarter of the size. This microrobot has 90 legs arranged into 6 groups of 15. The intended operation of this microrobot is the same as for

the microrobot presented in the previous section. The leg design used is shown in Figure 5-12 and Figure 5-13. This leg is made from poly1 and poly2, instead of just poly1. The legs are guaranteed to be normal to the substrate after assembly because the base locks into locking arms that are anchored to the substrate.

Figure 5-61 shows a side view of this "quarter size" microrobot. Any legs that did not self assemble during the release process were assembled using probes. The microrobot shown in Figure 5-61 was used to test for the maximum operating voltage and current. This test caused the flexures of some of the legs to melt, hence the reason not all the legs are perpendicular with respect to the substrate in Figure 5-61. This microrobot's maximum supply voltage was determined to be approximately 8 volts at 74 mA.

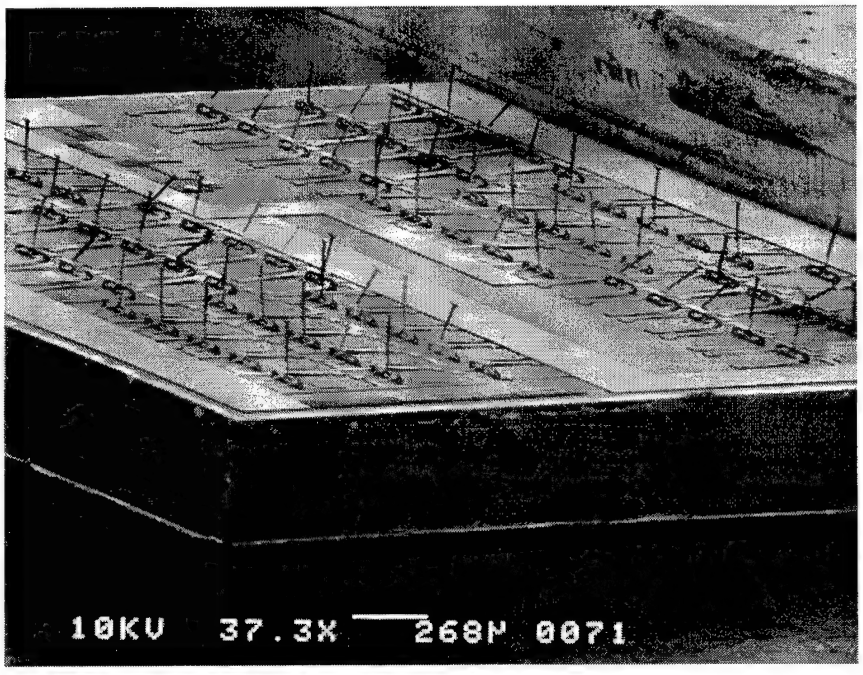

Figure 5-61: Scanning electron micrograph of a side view of the "quarter size" microrobot.

As already described in Section 5.1, the legs are powered through the polysilicon on polysilicon contact of the locking arms to the locking arm slots of the base. Figure 5-61 demonstrates the unreliability of this type of connection by showing that some legs melted, and some did not. Figure 5-62 shows a closer view of the microrobot legs from Figure 5-61. Although the connections are relatively unreliable, all the legs are observed to deflect when the circuit is provided power. Video recordings of the moving microrobot legs were obtained.

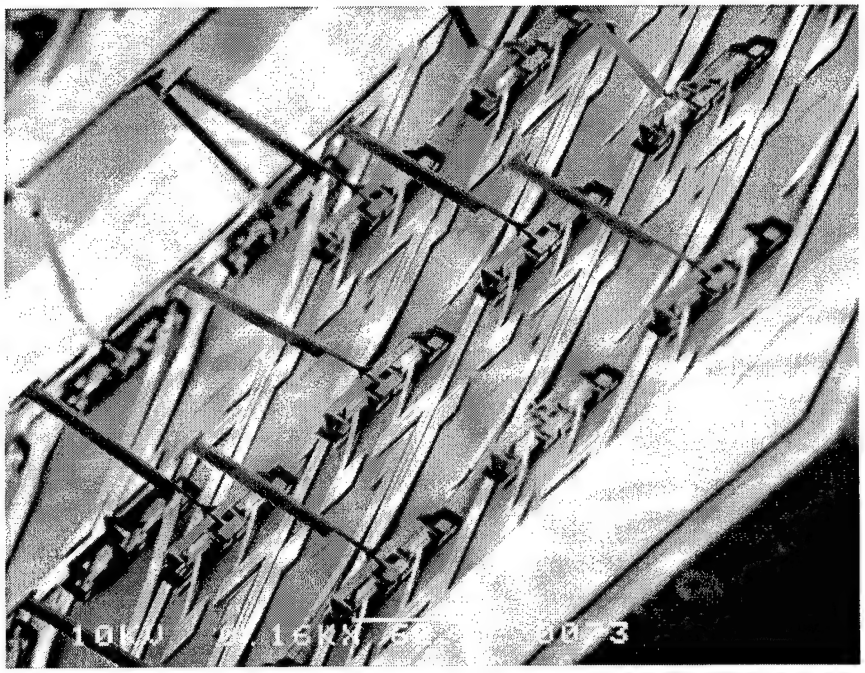

Figure 5-62: Closer view of the microrobot legs from Figure 5-61.

One microrobot was assembled and gold wires bonded to the wirebond pads. The resistance from each leg circuit to the substrate ground was measured to be approximately

1000 Ω. Assuming all the legs, in one leg circuit consisting of 45 legs, are connected equivalently, and neglecting the resistance of the gold wiring, the resistance of one leg system is estimated to be $45 \times 1000\ \Omega = 45\ k\Omega$.

Several attempts were made to lower a microrobot onto the walking surface using the same setup described for the previous microrobot. However, the gold bondwires would not allow the microrobot to release from the positioning arm. Similar to the case of the mechanically lapped microrobot, the microrobot's small mass allows the gold wires to restrict movement. As the microrobot is lowered toward the walking surface, the gold wires touch the walking surface before the microrobot. The small weight of the microrobot, relative to the stiffness of the gold wires, allows the gold wires to keep the microrobot pressed up against the positioning arm.

To show that this microrobot design could support its own weight, the microrobot was lowered onto the walking surface without gold wires connected. Figure 5-63 shows a captured video image of the freestanding microrobot with a freshly killed cockroach (asphyxiated using methanol) lying on the back of the microrobot.

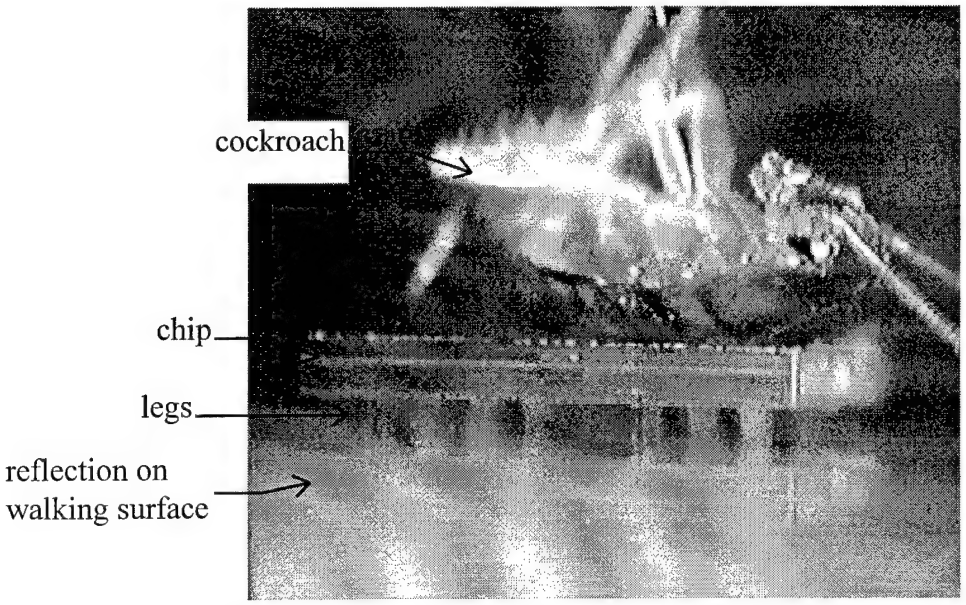

Figure 5-63: Captured video image of freestanding microrobot with a dead cockroach lying on the back of the microrobot.

A gold bondwire was wrapped around the cockroach's legs. The cockroach was then lowered, by holding onto the gold bondwire with the hand, onto the microrobot. Figure 5-64 is a series of captured video images showing the microrobot supporting its own weight plus the weight of (a) one more microrobot, (b) two more microrobots, (c) three more microrobots, (d) four more microrobots. Gold bondwires were connected to each load microrobot and used as handles to lower the load microrobot, by hand or tweezers, onto the freestanding microrobot.

During the placement of each load microrobot, the freestanding microrobot was unintentionally scooted around, demonstrating dynamic stability. Note that the load microrobots were not able to be stacked uniformly on top of the freestanding microrobot because of the gold bondwires. The addition of a fifth microrobot finally caused the

microrobot legs to collapse, as shown in Figure 5-65.

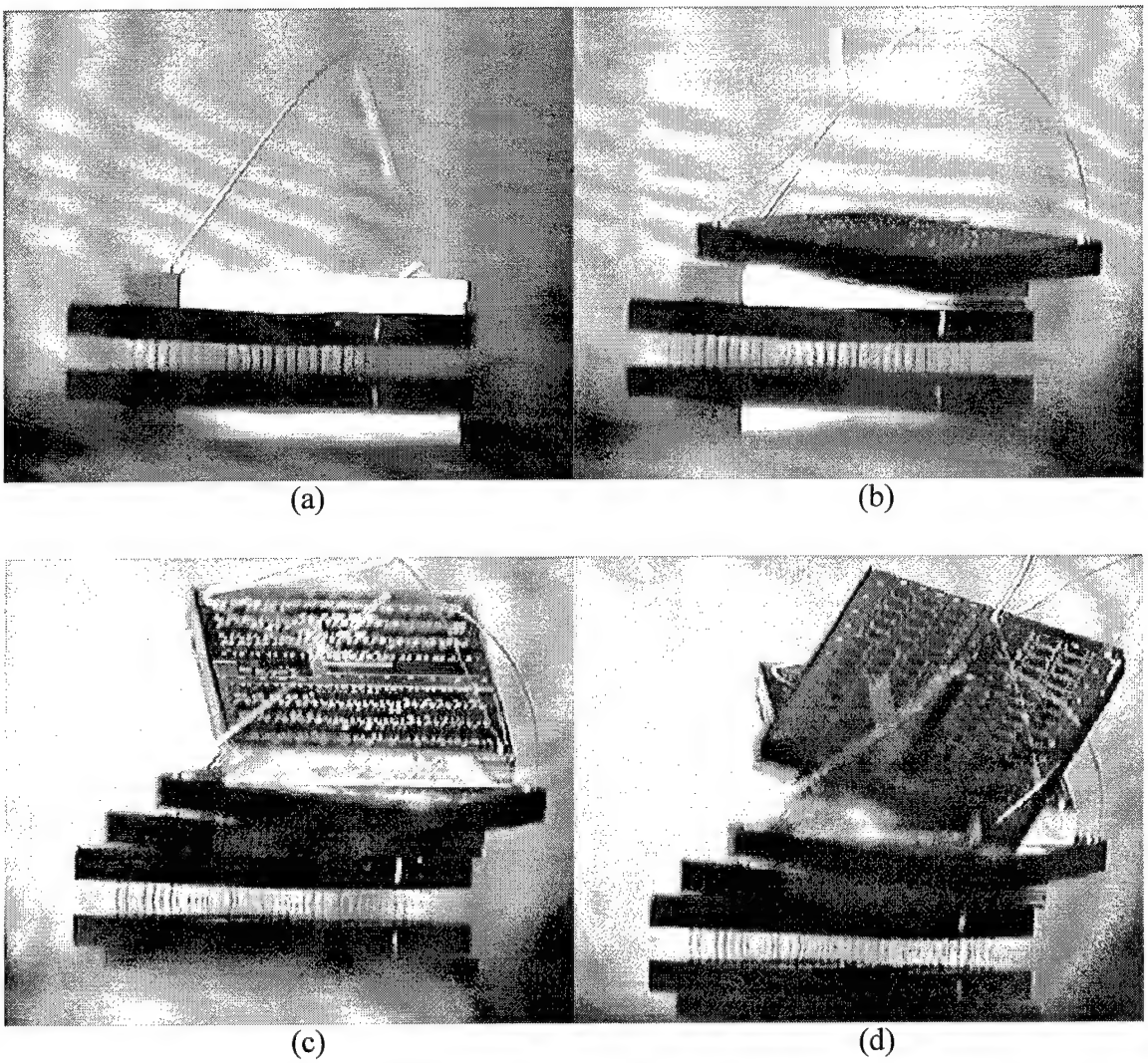

Figure 5-64: A series of captured video images showing the microrobot supporting its own weight plus the weight of (a) one more microrobot, (b) two more microrobots, (c) three more microrobots, (d) four more microrobots.

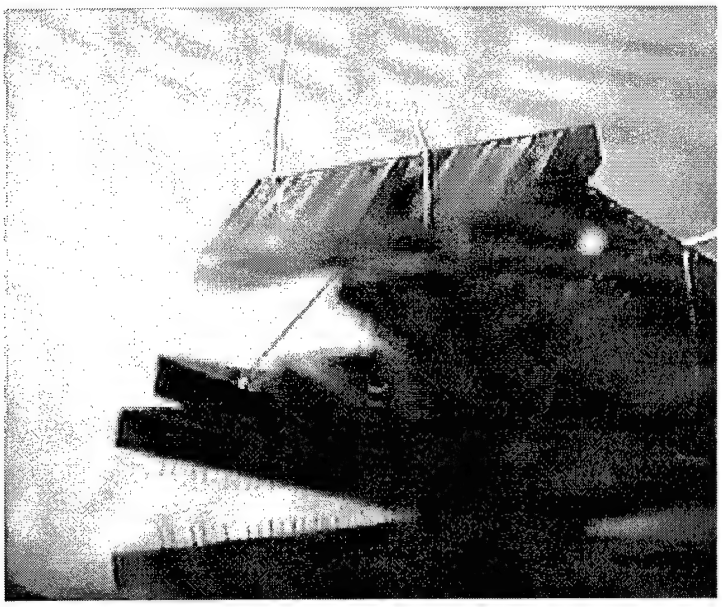

Figure 5-65: Captured video image of collapsed microrobot.

The microrobot was retrieved, and the resulting damage can be seen in the scanning electron micrograph in Figure 5-66. The bases were not affected and the legs broke off near the top of the flexures. The microrobot used in this experiment was initially missing five legs that were damaged during the release process. This microrobot was using only 85 legs.

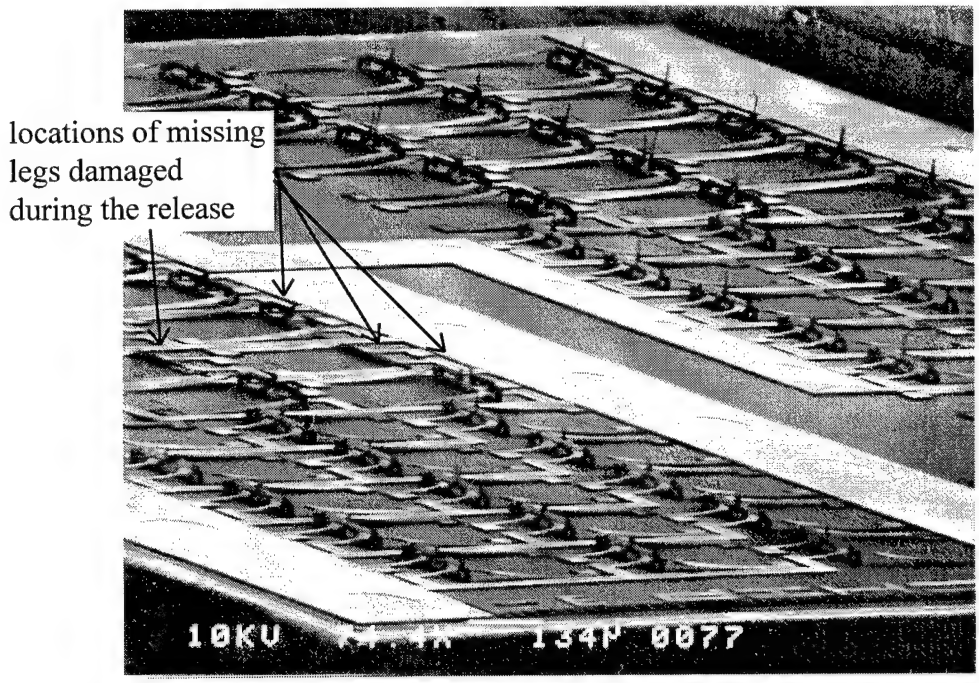

Figure 5-66: Scanning electron micrograph showing damage to the microrobot legs after collapsing.

Figure 5-64 (d) shows that the microrobot is able to support five times its original weight, were its original weight is approximately 313.97 μN. Using Eq. (2) and the following parameters:

a = 3.5 μm, the nominal thickness of the poly1 and poly2 layers

b = 2 x 2.5 μm = 5 μm, the width of two thermal actuator flexures considered together

l = 230 μm, length of the leg

E = 169 GPa [3]

F_{BF}, for this microrobot leg design, is found to be approximately 140.82 μN. Comparing F_{BF} to five times the weight of a microrobot, we can estimate that at least 12 legs are

needed for the chip to be supported by the legs in an unstable equilibrium. Since this loaded microrobot has 90 legs, this design possesses a factor of safety of at least 7.5. Finally, comparing F_{BF} to the weight of a single microrobot, it is estimated that at least 3 legs are needed for the chip to be supported by the legs in an unstable equilibrium, therefor, this design possesses a factor of safety of 90/3 = 30.

5.5 References

[1] J. Reid, V. Bright, and J. Comtois, "Automated assembly of flip-up micromirrors," *International Conference on Solid-State Sensors and Actuators, Transducers '97*, Chicago, IL, pp. 347-350, Jun. 1997.

[2] E. Obermeier, "Mechanical and thermophysical properties of thin film materials for MEMS: techniques and devices," *Materials Research Society Symposium Proceedings*, vol. 444, pp. 39-57, 1997.

[3] W. Sharpe, B. Yuan, R. Vaidyanathan, and R. Edwards, "Measurement of Young's Modulus, Poisson's Ratio, and tensile strength of polysilicon," *Proceedings of the 10th Annual International IEEE MEMS Workshop*, pp. 424-429, 1997.

[4] S. Garverick, M. Nagy, N. Rao, D. Harstfield, and A. Purushotham, "A capacitive sensing integrated circuit for deflection of micromotor critical angles," *IEEE Journal of Solid-State Circuits*, vol. 32, no. 1, pp. 23-30, Jan. 1997.

[5] I. Dufour, E. Sarraute and A. Abbas, "Optimization of the geometry of electrostatic micromotors using only analytical equations," Journal of Micromechanics and Microengineering, vol. 6, no. 1, pp. 108-111, 1996.

[6] B. J. Blosser, "A survey of insect motion," Private Communications, 15 Jan 1997.

[7] J. H. Comtois and V. M. Bright, "Surface micromachined polysilicon thermal actuator arrays and applications," *Technical Digest, Solid State Sensors and Actuators Workshop*, pp. 174-177, 1996.

[8] J. E. Shigley and C. R. Mischke, *Mechanical Engineering Design*, 5th ed., McGraw - Hill, 1989.

6. Conclusions and Recommendations

This chapter contains a brief description of the final status of this research and recommendations for future research. Sections 6.1 - 6.4 will cover the four research goals presented in Chapter 1.

6.1 Final Status and Recommendations for Erecting Microstructures to a Position Normal to the Substrate Using Self Assembly Techniques

The goal of erecting a microstructure normal to the substrate using self assembly techniques was not met in this research. The designs in this research concentrated on assembling microstructures with low resistance electrical connections available to power the assembled microstructure. Assembling a microstructure alone, without providing low resistance electrical contacts is an easier problem to solve, and has already been demonstrated. This research has achieved designs of microsystems that can be erected to angles less than 90 degrees while being supplied by low resistance electrical connections. The following are some possible applications for the novel achievements made in working towards this goal:

1) Microrobot legs for a robot where the body has a size on the order of 1000 μm. The robot must possess on board control circuitry and a power supply. The robot could walk or swim. Combining the compact design of the spring wires from the MUMPs 20 fabrication run with the jack, base, and leg design

in MUMPs 18 will produce a 2-degree of freedom leg or flipper.

2) Micro-sampler or micro-anchors for an autonomous micro-exploration vehicle. Consider fabricating a proven microgripper design on the microrobot leg-base instead of a leg. This system could be mounted on the outside of a micro-exploration vehicle. When the vehicle needs a sample from the environment, the microgrippers could deflect away from the vehicle, grab the sample, and return against the vehicle. The sample could then be dropped into a micro-analyzer situated under the gripper. The grippers could also act as an anchor by gripping the walls of an artery, for example, when the vehicle needs to be stationary.

The main problem with achieving this design goal is the lack of powerful actuation normal to the substrate. I would like to present two recommendations for realizing powerful, compact, and novel actuation methods. These two recommendations are not compatible with the MUMPs process, and the restriction on using the MUMPs process would have to be removed.

1) Making actuators from an expandable material which expands upon reaction with a chemical or electrical stimulation. Figure 6-1 shows a drawing of this expandable actuation idea. The fabrication process could include depositing and patterning a layer of expandable material. Next, a polysilicon cap could be deposited and patterned over the material to help channel or contain the expansion. The rest of the microstructures could then be deposited and

patterned as usual. The fabricated product could be released as usual, and then immersed in a reactant which causes the special expandable material to expand.

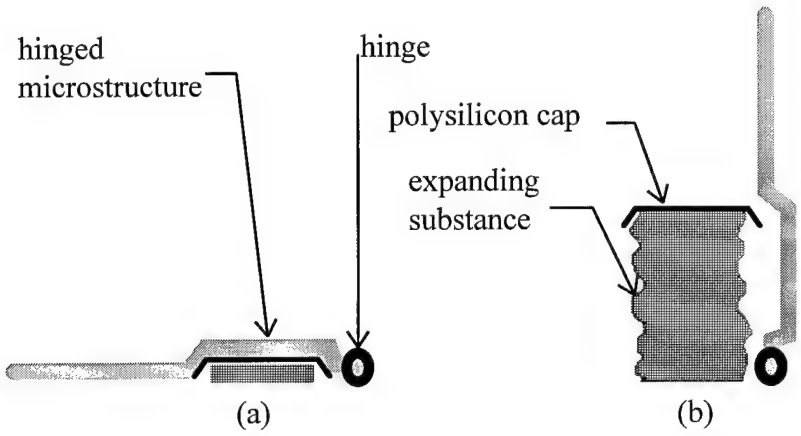

Figure 6-1: Drawing of a conceptual self assembly method using an expandable material: (a) shows the microstructure before assembly, and (b) after the expandable material expands, erecting the microstructure.

2) The most compact, powerful, and elegant actuators in the universe are muscles. Consider the ant. The ant can carry objects over ten times its own weight. The ant's leg contains muscles which take up less space than the exoskeleton leg as a whole. A second proposal involves depositing and patterning artificial muscles over the existing polysilcon hinge designs. When the muscles are introduced to a chemical, or stimulated electrically, the muscle should contract appreciably, causing hinges to fold and assemble microstructures.

6.2 Final Status and Recommendations for Providing Electrical Power to Erected Structures by Means of Practical Low Resistance Electrical Connections

The goal of providing electrical power by means of practical low resistance electrical connections is met in this research. Because the spring wires provide a contiguous connection to the device needing power, the spring wires provide the lowest resistance electrical connections possible for the MUMPs process. The resistance of the spring wires can be controlled by the quality and resistivity of the fabrication materials, and by the geometry of the wire design. The resistance of one of the spring wires used to power the robot leg in the MUMPs 20 design is approximately 13 Ω.

The spring wires are practical because no extra steps in fabrication or post processing are required to create them. They are also practical because they do not require any elaborate setup to connect them to a microstructure. The spring wires are extremely compact and can be fashioned into any shape imaginable.

6.3 Final Status and Recommendations for Realizing Circular Motion Normal to the Substrate

The goal of realizing circular motion normal to the substrate is met in this research. The results of this research have demonstrated that wheels can be assembled normal to the substrate and rotated by means of bumping the edge of the wheel with a

vertically deflecting thermal actuator. The design used in this research leaves much room for improvement, however. After improvements are made, the wheel could be used as an optical chopper, a useful optical signal processing tool. The frame holding the wheel must be redesigned such that the wheel can not get stuck on this frame. Also, the frame can be redesigned to be simpler and easier to assemble. Figure 6-2 shows a drawing of a proposed design for a wheel suitable to be fabricated using the MUMPs process. This structure is actually a one piece structure that requires no assembly except for lifting the frame into an upright position. The wheel would actually be half poly1 and half poly2. The axle would also have to be half poly1 and half poly2. The wheel would unfold from the axle as the frame is lifted. One or more vertically deflecting thermal actuators can be strategically placed under the frame to lift the frame. A vertically deflecting thermal actuator can also be strategically placed under the wheel to provide a means to rotate the wheel.

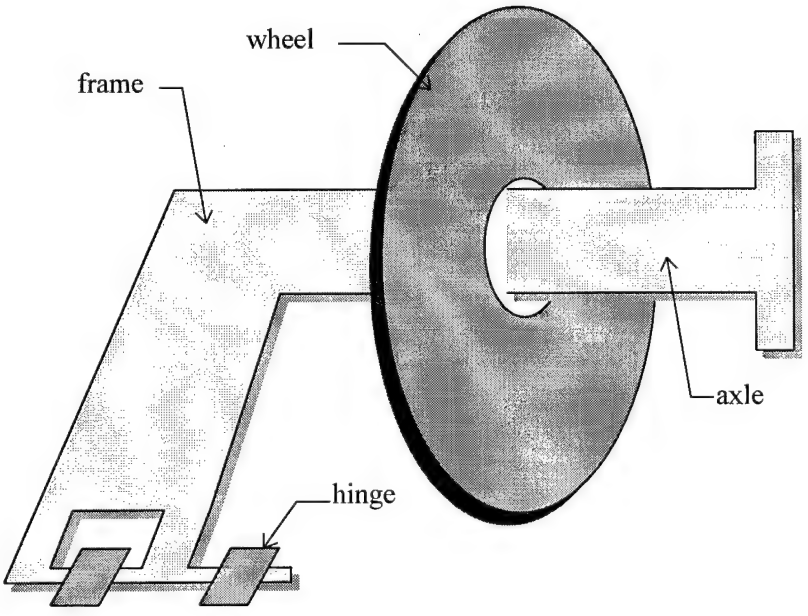

Figure 6-2: Drawing of proposed wheel.

6.4 Final Status and Recommendations for Realizing a Microrobot That Can Move on a Flat Surface

The goal of realizing a microrobot that can move on a flat surface has not been met in this research. The full die microrobot failed to walk because the legs could not support its weight. The lapped die microrobot failed to walk because the die was so light that the gold bondwires overpowered it, and dictated its movement. However, the walking scheme based on six legged insects was valid, as shown by being able to transport kapton film. One application for transport using microstructures is a precise micro-positioner.

The improved version of the microrobot proved to be dynamically robust, even after being loaded to five times its original weight. However, the light weight of the microrobot alone allowed it to be overpowered by the gold bondwires. Combining the leg design of the improved microrobot with the spring wiring and full die design of the original microrobot should produce a microrobot that walks.

6.5 Overall Conclusions

Overall, this research has brought the field of microelectromechanical engineering a little closer to the realization of minute unmanned surveillance vehicles, a valuable and life saving application for the military. This research has participated in transcending

MEMS from the two dimensional to the three dimensional world, opening a flood gate of potential applications.

Appendix A: Dynamic and Static Modeling of Microrobot Leg Self Assembly

This appendix attempts to explain the reasons for the failure of the jacks to lift the base described in Section 5.1. In this appendix, the static equations describing the microrobot leg self assembly system are derived. The components of the equation such as the force provided by the jack and the resisting torque on the base provided by the spring wires is estimated and compared.

A.1 Deriving Dynamic and Static Equations

Let the rigid hinged leg support base and rigid leg from the MUMPs 20 microrobot leg self assembly system be represented by the rigid hinged plate shown in Figure A-1.

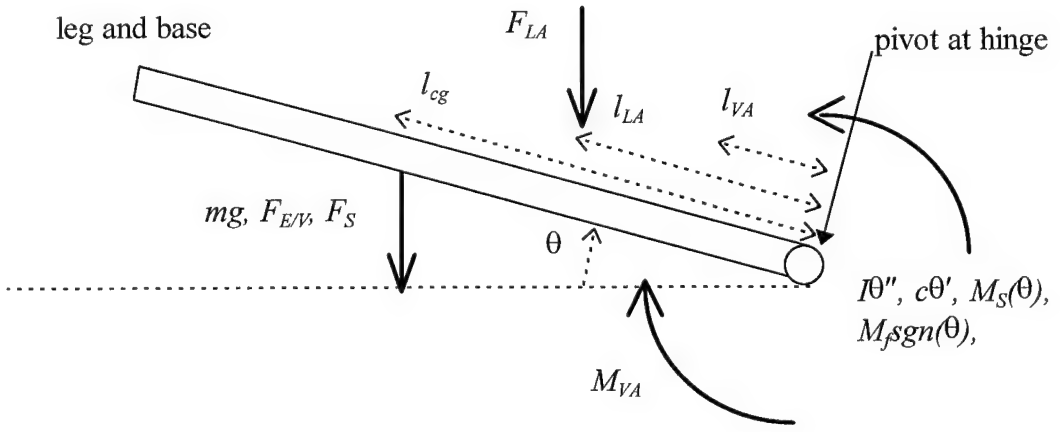

Figure A-1: Representation of the microrobot leg and base showing the different moments and forces acting upon it.

From Figure A-1, and Newton's second law, we can derive the dynamic equation that describes the rotation of the microrobot leg and base system (hereafter called the leg-base) about its hinge pin:

$$\sum M = I\theta'' = M_{VA} - c\theta' - mgl_{CG}\cos(\theta) - M_f\mathrm{sgn}(\theta) - F_{E/V}l_{CG}\cos(\theta) - M_S\delta(\theta) - M_{SW}(\theta) - F_{LA}l_{LA}\cos(\theta) \quad \text{(A-1)}$$

where the sum of the moments about the hinge pin is equal to the moment of inertia (I) of the leg-base structure times the angular acceleration (θ''); and where M_{VA} is the moment provided by the back-bent vertically deflecting thermal actuators, c is the angular damping coefficient, θ' is the angular velocity, m is the mass of the system, g is the acceleration of gravity, l_{CG} is the distance measured from the bottom of the hinge pin to the center of gravity of the system, θ is the angular displacement of the system measured from the substrate, M_f is the moment caused by the kinetic friction of the hinge pin against the nitride or hinge cap, $\mathrm{sgn}(\theta)$ is the signum function defined as $\{\mathrm{sgn}(\theta) = -1$ for $\theta < 0$, $\mathrm{sgn}(\theta) = 1$ for $\theta \geq 0\}$, $F_{E/V}$ is the superposition of electrostatic force and van der Waals forces, M_S is the moment caused by stiction, $\delta(\theta)$ is the discrete impulse function defined as $\{\delta(\theta) = 0$ for $\theta \neq 0$, $\delta(\theta) = 1$ for $\theta = 0\}$, $M_{SW}(\theta)$ is the moment function of θ caused by the restoring force of the spring wires, F_{LA} is the restoring force applied by the locking arms, and l_{LA} is the distance measured from the bottom of the hinge pin to the point where F_{LA} is applied.

The goal of this analysis is to determine if the jacks or vertically deflecting thermal actuators can lift the robot leg into position. At this point, the analysis will not be concerned with the dynamic behavior of the leg-base system during the lift. In other

words, we are not concerned with how the leg gets to the upright position -- the transient analysis, but whether or not the leg can get to the upright position -- a steady state analysis. For the leg to reach the upright position, the moment applied to the base by the vertically deflecting thermal actuators must be greater than the opposing static (or position dependent) moments at every deflection (θ) from 0 to $\pi/2$. Considering Equation (A-1) with $\theta'' = \theta' = 0$, and rearranging, yields the static model for the leg:

$$M_{VA} = mgl_{CG}\cos(\theta) + M_f\mathrm{sgn}(\theta) + F_{E/V}l_{CG}\cos(\theta) + M_S\delta(\theta) + M_{SW}(\theta) + F_{LA}l_{LA}\cos(\theta). \quad \text{(A-2)}$$

The following sections will analyze each term in Equation (A-2).

A.2 M_{VA}: Finding the Moment Caused by the Vertically Deflecting Thermal Actuators

The primary means for erecting the leg-base structure are the two vertically deflecting thermal actuators. At $\theta = 0$, the tip of an actuator contacts the base at a distance, l_{VA}, measured from the bottom of the base's hinge pin (refer to Figure A-1). Immediately after the actuators have been back-bent, a force, F_{EQ}, is applied by each actuator, to the base at l_{VA} causing a moment about the base's hinge pin. As θ increases, the tip of an actuator slides away from the hinge pin, thereby increasing the length of the moment arm of F_{EQ}. However, the perpendicular-to-the-moment-arm component of F_{EQ} decreases as θ increases. The moment provided by two actuators, M_{VA} is then:

$$M_{VA} = 2F_{EQ\perp} \times \textit{moment arm} = 2F_{EQ}\cos(\theta) \times l_{VA}/\cos(\theta) = 2F_{EQ}l_{VA}. \qquad \text{(A-3)}$$

To find F_{EQ}, consider the following. Figure A-2 shows a side view of two vertically deflecting thermal actuators after being backbent. The leg-base was lifted and locked into its vertical position before actuation. Note the deformed poly2 hot arms and the flexed poly1 cold arm. The reaction force, R_1, and reaction moment, M_0, on the cold arm, at the anchor point, near the probe pads, is also labeled in Figure A-2. This anchor point will also be the reference of the x-y axis whose orientation is shown in Figure A-3.

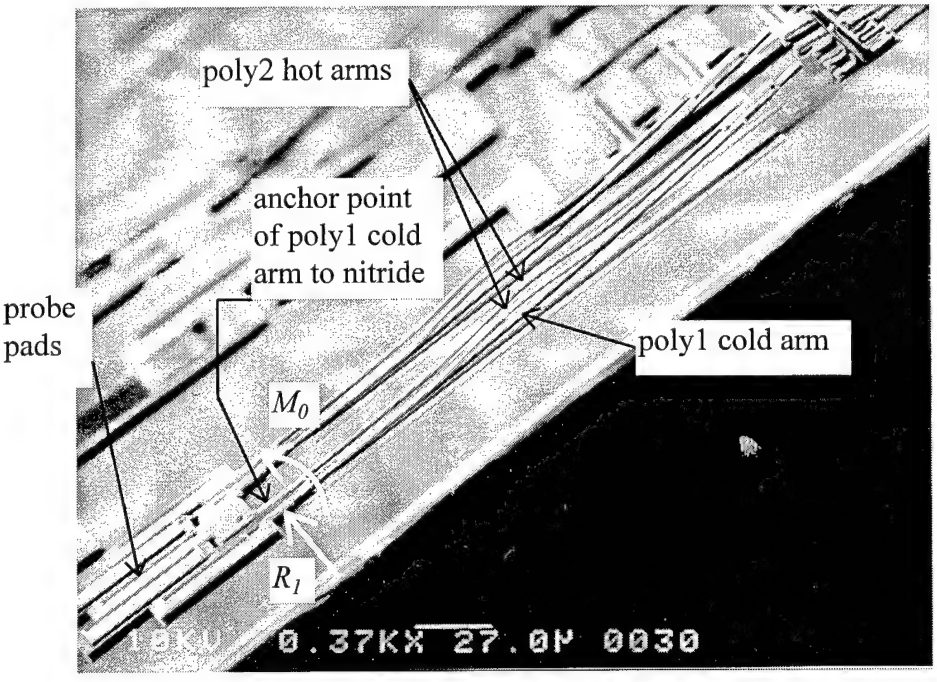

Figure A-2: Scanning electron micrograph showing a side view of two vertically deflecting thermal actuators after being backbent. The reaction force, R_1, and reaction moment, M_0, on the cold arm are also labeled.

Figure A-3 shows the tip of the vertically deflecting thermal actuator from Figure A-2 close up. Labeled in the figure is the deflection of the actuator tip, y_d, measured from the top of the poly1 beam, at point A, to the nitride, and the angle of the poly1 beam, ϕ, measured with reference parallel to the substrate plane. The angle, ϕ, actually represents the tangent ($dy/dx = \tan(\phi)$) to the curvature at point A. Point A is physically located at the center, on the top surface, of the poly1 beam, and is actually concealed by the poly2 layer, which, connects the hot arms to the cold arm.

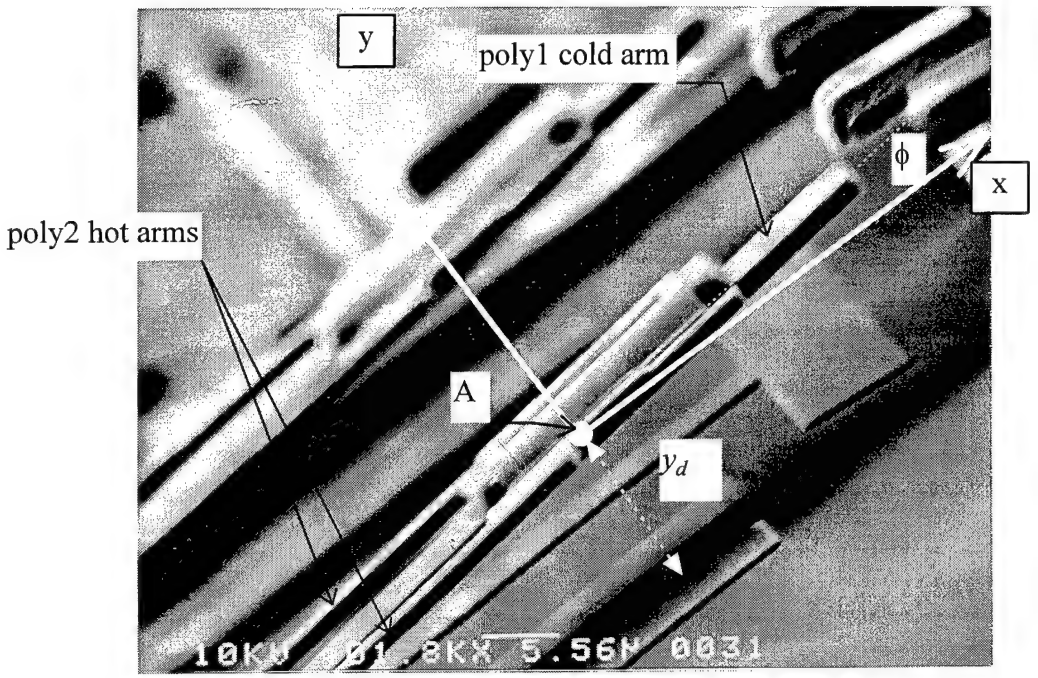

Figure A-3: Tip of the vertically deflecting thermal actuator from Figure A-2 shown close up. The deflection of the actuator tip, y_d, measured from the top of the poly1 beam, at point A, to the nitride, and the angle of the poly1 beam, ϕ, measured with reference parallel to the substrate plane is labeled.

Figure A-4 is a not-to-scale representation of one of the vertically deflecting thermal actuators from Figure A-2 and Figure A-3. Referring to Figure A-4, point B is physically located at the center, on the top surface, of the poly2 layer that connects the hot arms to the cold arm. The distance between points A and B is h, where h = 1 μm. The length, L, is the undeflected length of the cold arm from point 0 to A.

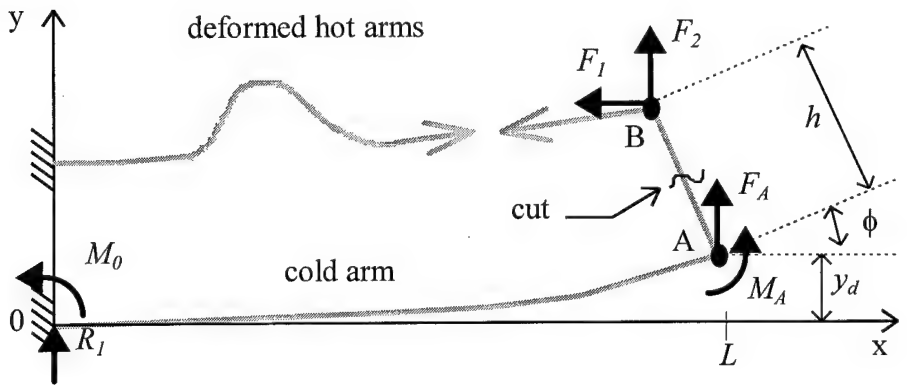

Figure A-4: Not-to-scale drawing of a single vertically deflecting thermal actuator after being back-bent. The forces and moments modeled in this analysis are labeled.

After back bending, the deformed hot arms exert some force, with components F_1 and F_2, at point B. If the connecting arm were to be cut, as shown in Figure A-4, the effects of point B on A can be represented by a reaction force at A (F_A), and a moment about A (M_A). The equivalent force, F_{EQ}, can be estimated using two methods, by using the beam deflection equation for a cantilever with an end load or by developing general bending moment and shear force expressions using singularity functions [1].

Beam Deflection Equation for a Cantilever with an End Load

A simple way to estimate F_{EQ} can be found by assuming that there is a single force, F_A, acting on the tip of the actuator, at point A causing the cold arm to deflect a measured deflection, y_d. The deflection, y_d, was measured experimentally at a probe station using a 100x objective. The objective was first focused on the nitride, and the reading from the micrometer-scaled fine-focus knob recorded. Next, the objective was refocused onto point B, and the reading on the fine-focus knob was again recorded. The difference between the two readings is the deflection of point B. The deflection of point A is then obtained by subtracting 1.5 μm, which is, the thickness of poly2. Eight, unloaded, actuators where back-bent in air by applying 4.3 mA at 16 V for 10 seconds. The deflections were recorded and a simple non-weighted average was taken to be, y_d = (13.5 ± 0.5) μm. The error due to imprecise measurements is taken as one half of the smallest discernible increment of measurement, 1 μm on the fine-focus knob, in this case. From henceforth, error due to imprecise measurements will be determined in this manner. The deflection, y_d, was confirmed by measuring the distance between point A and the nitride, on the SEM of Figure A-3, with a ruler. The resulting distance is 2.45 cm x 5.56 μm/cm = 13.62 μm. The actuator in Figure A-3 was photographed because it was optically measured to have deflected 13.5 μm. Neglecting the weight and any other force acting on the poly1 beam, the beam deflection equation for a cantilever with an end load yields [1]:

$$F_{EQ} = F_A = \frac{y_d 3EI}{L^3} = \frac{(13.5 \pm 0.5) \times 10^{-6} 3(169 \times 10^9) 1 \times 10^{-23}}{(235 \times 10^{-6})^3} \qquad \text{(A-4)}$$
$$= (\ 5.2740 \pm 0.1953) \times 10^{-6}\ \text{N}$$

where $a = 2$ μm and $b = 15$ μm are used for I, where $I = \frac{1}{12} ba^3$.

General Bending Moment and Shear Force Expressions using Singularity Functions

A more general approach to finding F_{EQ}, along with all the moments and reaction forces labeled in Figure A-4, is to use singularity functions [1]. Unless stated otherwise, the convention will be adopted where all clockwise bending moments and all shear forces acting in the positive x-y axis directions are positive. For this analysis, any effect on the actuator from electrostatic, van der Waals, or stiction forces will be neglected. With reference to Figure A-4, the loading function, q, for the cold arm is:

$$q = -M_0\langle x\rangle^{-2} + R_1\langle x\rangle^{-1} - w\langle x\rangle^{0} + F_A\langle x - L\rangle^{-1} - M_A\langle x - L\rangle^{-2} \qquad \text{(A-5)}$$

where $\langle x\text{-}c\rangle^{-2}$ is the concentrated moment (unit doublet) at point c defined as $\{\langle x\text{-}c\rangle^{-2} = 0$ for $x \neq c$, $\langle x\text{-}c\rangle^{-2} = \pm\infty$ for $x = c\}$, $\langle x\text{-}c\rangle^{-1}$ is the concentrated force (unit impulse) at point c defined as $\{\langle x\text{-}c\rangle^{-1} = 0$ for $x \neq c$, $\langle x\text{-}c\rangle^{-1} = +\infty$ for $x = c\}$, $\langle x\text{-}c\rangle^{0}$ is the unit step at point c defined as $\{\langle x\text{-}c\rangle^{0} = 0$ for $x < c$, $\langle x\text{-}c\rangle^{0} = 1$ for $x \geq c\}$, and w is the weight density of the cold arm defined as $w = (abL \times$ density of Si $\times$ acceleration of gravity$)/L = 2$ μm $\times$ 15

$\mu m \times 2330\ kg/m^3 \times 9.8\ m/s^2 = 685.02\times10^{-9}$ N/m. Integrating Equation (A-5) yields a relationship for the shear forces (V) acting on the cold arm:

$$V = EI\frac{\partial^3 y}{\partial x^3} = \int_{-\infty}^{L+} q\,dx = -M_0\langle x\rangle^{-1} + R_1\langle x\rangle^{0} - w\langle x\rangle^{1} + F_A\langle x-L\rangle^{0} - M_A\langle x-L\rangle^{-1}\Big|_{-\infty}^{L+} \quad \text{(A-6)}$$
$$= R_1 - wL + F_A = 0$$

where $\langle x\text{-}c\rangle^1$ is the ramp function at point c defined as $\{\langle x\text{-}c\rangle^1 = 0$ for $x < c$, $\langle x\text{-}c\rangle^1 = x\text{-}c$ for $x \geq c\}$. Integrating Equation (A-6) yields a relationship for the bending moments (M) acting on the cold arm:

$$M = EI\frac{\partial^2 y}{\partial x^2} = \int_{-\infty}^{L+} V\,dx = -M_0\langle x\rangle^{0} + R_1\langle x\rangle^{1} - \frac{w}{2}\langle x\rangle^{2} + F_A\langle x-L\rangle^{1} - M_A\langle x-L\rangle^{0}\Big|_{-\infty}^{L+} \quad \text{(A-7)}$$
$$= -M_0 + R_1 L - \frac{w}{2}L^2 - M_A = 0$$

where $\langle x\text{-}c\rangle^2$ is the parabolic function at point c defined as $\{\langle x\text{-}c\rangle^2 = 0$ for $x < c$, $\langle x\text{-}c\rangle^2 = (x\text{-}c)^2$ for $x \geq c\}$. Integrating Equation (A-7) yields a relationship for the tangent ($\tan(\phi)$) of the cold arm:

$$EI\frac{\partial y}{\partial x} = \int_{-\infty}^{L+} M\,dx = -M_0\langle x\rangle^{1} + \frac{R_1}{2}\langle x\rangle^{2} - \frac{w}{6}\langle x\rangle^{3} + \frac{F_A}{2}\langle x-L\rangle^{2} - M_A\langle x-L\rangle^{1}\Big|_{-\infty}^{L+} \quad \text{(A-8)}$$
$$= -M_0 L + \frac{R_1}{2}L^2 - \frac{w}{6}L^3 = EI\tan(\phi)\Big|_{\phi\ at\ x=L}$$

where $\langle x\text{-}c\rangle^3$ is the cubic function at point c defined as $\{\langle x\text{-}c\rangle^3 = 0$ for $x < c$, $\langle x\text{-}c\rangle^3 = (x\text{-}c)^3$ for $x \geq c\}$, and ϕ at $x = L$ (at point A) on the cold arm was measured from the SEM in Figure A-3, using a protractor, as $\phi = 5° \pm 0.5°$. Integrating Equation (A-8) yields a relationship for the deflection (y) of the cold arm:

$$EIy = \int_{-\infty}^{L+} EI\frac{\partial y}{\partial x}dx = -\frac{M_0}{2}\langle x\rangle^2 + \frac{R_1}{6}\langle x\rangle^3 - \frac{w}{24}\langle x\rangle^4 + \frac{F_A}{6}\langle x-L\rangle^3 - \frac{M_A}{2}\langle x-L\rangle^2\Big|_{-\infty}^{L+} \quad \text{(A-9)}$$
$$= -\frac{M_0}{2}L^2 + \frac{R_1}{6}L^3 - \frac{w}{24}L^4 = EIy\big|_{y\,at\,x=L}$$

where $\langle x\text{-}c\rangle^4$ is the tetradic function at point c defined as $\{\langle x\text{-}c\rangle^4 = 0$ for $x < c$, $\langle x\text{-}c\rangle^4 = (x\text{-}c)^4$ for $x \geq c\}$, and y at $x = L$ (at point A) on the cold arm is y_d as found in the previous paragraphs. Summing the moments about point A gives:

$$-M_0 + R_1 L - F_1 h\cos(\phi) + F_2 h\cos(\phi) - \frac{w}{2}L^2 = 0. \quad \text{(A-10)}$$

Finally, summing the forces in the y direction yields:

$$R_1 + F_2 - wL = 0. \quad \text{(A-11)}$$

Equations (A-6) through (A-11) represent six equations in six unknowns. Building Equations (A-6) through (A-11) into matrix form, the forces and moments can be found by solving the following linear equation:

$$\begin{bmatrix} 0 & 1 & 1 & 0 & 0 & 0 \\ -1 & L & 0 & -1 & 0 & 0 \\ -L & \frac{L^2}{2} & 0 & 0 & 0 & 0 \\ -\frac{L^2}{2} & \frac{L^3}{6} & 0 & 0 & 0 & 0 \\ -1 & L & 0 & 0 & -h\cos(\phi) & h\cos(\phi) \\ 0 & 1 & 0 & 0 & 0 & 1 \end{bmatrix} \begin{bmatrix} M_0 \\ R_1 \\ F_A \\ M_A \\ F_1 \\ F_2 \end{bmatrix} = \begin{bmatrix} wL \\ \frac{w}{2}L^2 \\ EI\tan(\theta) + \frac{w}{6}L^3 \\ EIy_d + \frac{w}{24}L^4 \\ \frac{w}{2}L^2 \\ wL \end{bmatrix}. \quad \text{(A-12)}$$

Solving Equation (A-12) using MATLAB on an IBM compatible 486DX2 running at 66 MHz with 16 Mbytes of RAM with L = 235 μm, h = 1 μm, ϕ = 5°, w = 685.02×10^{9} N/m, E = 169 GPa [2], $I = 1\times10^{-23}$ m^4, and y_d = 13.5 μm gives:

$$\begin{bmatrix} M_0 \\ R_1 \\ F_A \\ M_A \\ F_1 \\ F_2 \end{bmatrix} = \begin{bmatrix} -1.2204\times10^{-9}\ \text{Nm} \\ -5.0318\times10^{-6}\ \text{N} \\ 5.0320\times10^{-6}\ \text{N} \\ 3.7923\times10^{-11}\ \text{Nm} \\ 4.3100\times10^{-5}\ \text{N} \\ 5.0320\times10^{-6}\ \text{N} \end{bmatrix}.$$

For this analysis, F_{EQ} is also assumed to be equal to F_A. Table 1 lists values for F_{EQ} as a function of y_d and ϕ.

	y_d		
ϕ	13 μm	13.5 μm	14 μm
4.5°	5.8640 μN	6.6454 μN	7.4267 μN
5°	4.2506 μN	5.0320 μN	5.8133 μN
5.5°	2.6348 μN	3.4161 μN	4.1974 μN

Table 1: Values for F_{EQ} as a function of y_d and ϕ.

Choosing F_{EQ} to be the nominal value of 5.0320 μN, the moment contribution, M_{VA}, in Equation (A-2) is estimated from Equation (A-3) as 1.0567×10^{-10} Nm. M_{VA} is estimated assuming that F_{EQ} is constant throughout the deflection of the actuator and F_{EQ} is translated through a rigid extension from point A to the point where the extension contacts the leg-base, where $l_{VA} = 10.5$ μN.

A.3 mgl_{CG}: Finding the Moment Contribution of the Leg-Base System's Weight

Let l_{CG} be defined as the y-component of the center of gravity of the system shown in Figure A-5. Figure A-5 shows a not-to-scale drawing of a microrobot leg-base represented by elementary shapes. The right half of the base, not shown, is symmetric with the left. Labeled is the area of the elementary shape, #x#; x-y coordinate for the center of mass of the elementary shape, (#,#); and structural materials that the shape is made from , p1 = poly1, p2 = poly2, and g = gold. The center of gravity will be found with respect to the x-y coordinate system shown in the figure.

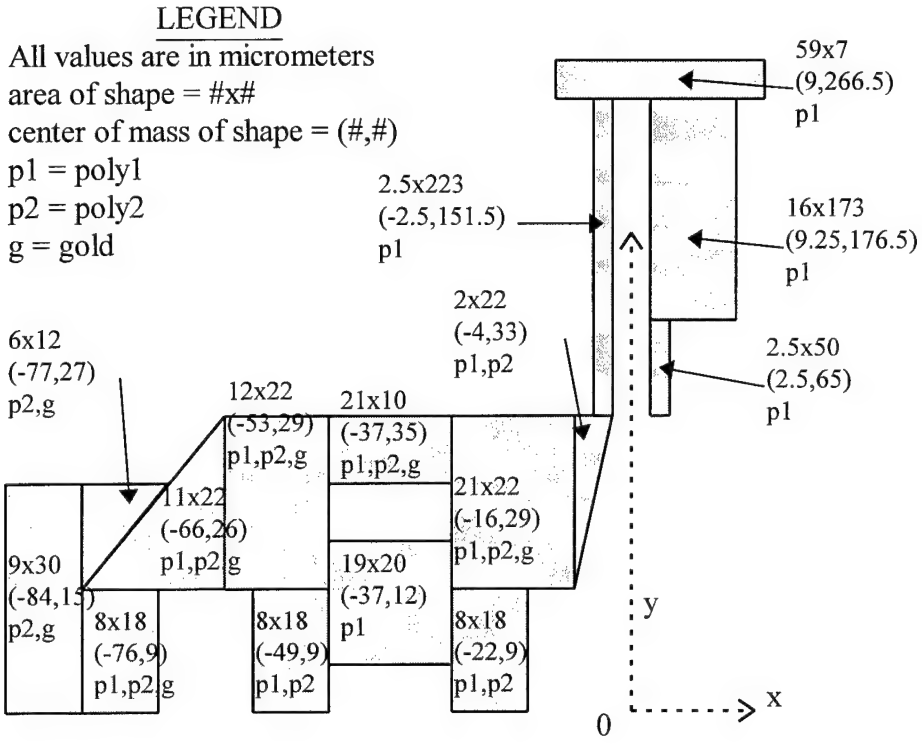

Figure A-5: Not-to-scale drawing of a microrobot leg-base represented by elementary shapes. The right half of the base, not shown, is symmetric with the left. Labeled is the area of the elementary shape, #x#; x-y coordinate for the center of mass of the elementary shape, (#,#); and structural materials that the shape is made from , p1 = poly1, p2 = poly2, and g = gold.

The y-coordinate of the center of gravity is:

$$l_{CG} = \frac{\sum y_i m_i}{\sum m_i} = \frac{4.7705 \times 10^{-15}}{8.3061 \times 10^{-11}} = \ 57.434 \times 10^{-6}\,\text{m} \qquad \text{(A-13)}$$

where y_i is the y coordinate of the center of mass , m_i is the mass for each elementary shape, the density for Si is 2330 kg/m^3, and the density for Au is 19320 kg/m^3. The

moment contribution, in Equation (A-2), due to the weight of the leg-base system, is therefor:

$$mgl_{CG}\cos(\theta) = \quad 8.3061\times10^{-11}\ (9.8)57.434\times10^{-6}\cos(\theta) = 4.6751\times10^{-14}\ \cos(\theta)\ \text{Nm}. \quad \text{(A-14)}$$

A.4 $M_f$sgn(θ): Finding the Moment Caused by Friction at the Hinge Pin

The type of hinge used for the microrobot leg can be seen in Figure 3-4. At $\theta = 0$, the hinge pin is suspended between the hinge cap and the nitride by the spring wires. The hinge pin will not experience contact forces until motion is already in progress, and even then, one can imagine that the contact force will be applied gradually. For the aforementioned reason, the frictional forces will be treated as kinetic, instead of static. During actuation, $\theta > 0$, the contact point of the hinge pin may be against the hinge cap, the nitride, or nothing. As an estimate, let the moment caused by kinetic friction, in Equation (A-2), be given by:

$$M_f = 0.4\left|2F_{EQ} - 2F_{SW}\right|2.0156\times10^{-6}\ \text{Nm} \quad \text{(A-15)}$$

where 0.4 is the coefficient of kinetic friction for glass on glass [3], F_{SW} is the restoring force of the spring wire parallel to F_{EQ}, and 2.0156×10^{-6} m is the moment arm measured from the center of the hinge pin to a corner of the hinge.

A.5 $F_{E/V}l_{CG}\cos(\theta)$: Finding the Moment Caused by Electrostatic and van der Waals Forces

Electrostatic force is the attraction or repulsion felt between two bodies due to the electronic charge on each body. The energy of attraction, between two parallel objects, due to electrostatic forces is given by [4]:

$$E_{el} = \frac{\varepsilon_0 V^2}{2\delta} \text{ J/m}^2 \tag{A-16}$$

where E_{el} is normalized by area, ε_0 is the permativity of free space (8.8542×10^{-12} C^2/Nm^2), V is the voltage difference between the objects, and δ is the distance of separation. Since the leg-base system is grounded to the substrate ($V = 0$) and since the vertical thermal actuators are not electrically energized when they back bend and lift the base, electrostatic force could be neglected. However, as a worst case estimate, suppose some charge density were to build up on the leg-base and nitride, causing a voltage difference of 0.5 V. The force between the leg-base and substrate can be found from Equation (A-16) as:

$$F_{el} = \frac{A\varepsilon_0 V^2}{2\delta^2} = \frac{8.6155\times10^{-9}\varepsilon_0 0.5^2}{2(2\times10^{-6})^2} = 2.3839\times10^{-9} \text{ N} \tag{A-17}$$

where A is the area of the leg-base system found from Figure A-5.

Van der Waals forces is the attractive force due to the electrostatic force arising from the dipole fields of atoms [5]. The energy of attraction, between two parallel solid objects, due to van der Waals forces is given by [4]:

$$E_{vdW} = \frac{H}{12\pi\delta^2} \text{ J/m}^2 \tag{A-18}$$

where E_{vdW} is normalized by area and H is Hamaker's constant for Si in air, 27×10^{-20} J. The force between the leg-base and substrate can be found from Equation (A-18) as:

$$F_{vdW} = \frac{AH}{12\pi\delta^3} = \frac{8.6155\times10^{-9}(27\times10^{-20})}{12\pi(2\times10^{-6})^3} = 7.7130\times10^{-12} \text{ N} \tag{A-19}$$

The moment contribution to Equation (A-2) from electrostatic and van der Waals can now be estimated as:

$$\begin{aligned} F_{E/V}\, l_{CG} = (F_{es} + F_{vdW})\, l_{CG} &= (2.3839\times10^{-9} + 7.7130\times10^{-12})\, 57.4340\times10^{-6} \\ &= 1.3736\times10^{-13} \text{ Nm} \end{aligned} \tag{A-20}$$

A.6 $M_S\delta(\theta)$: Finding the Moment Caused by Stiction Forces

Stiction is the unwanted adhesion of microstructures to the substrate after a release process using liquid solvents and solutions. Stiction is assumed to be caused by capillary forces drawing structures to the substrate during drying. Legtenberg, et al. predict forces on the order of 1 mN for a structure with the area of the leg-base structure at a 1 μm separation from the substrate [4]. Unfortunately, actuators that can deliver mN of force are not on hand for this research.

Many methods have been developed to eliminate stiction, however. Some reported methods are limiting structure length [4], using "dry" release processes [6], coating microstructures with a hydrophobic coating [7], and "steering" liquid bridging away using special features on the periphery of a microstructure [8]. The method most commonly employed at AFIT and in this research of eliminating post release stiction is to use the MUMPs dimple layer. The dimple layer is used to create small support posts on the underside of microstructures. The small support posts serve two purposes, first, they "roughen" up the contact surface between the microstructure and the substrate. Secondly, they provide support across long microstructures that would normally buckle, if not supported by dimples, by the pull of capillary forces during the drying of the release chemicals. Stiction has not been observed during this research using dimples. Therefor, for this analysis, the moment contribution in Equation (A-2) due to stiction will be neglected.

A.7 $M_{SW}(\theta)$: Finding the Restoring Moment of the Spring Wires

The spring wires are the primary means of supplying electricity to the thermal actuator serving as a microrobot leg. There are two spring wires for each robot leg connected to the pivot point of leg-base hinges. Figure A-6 shows a cadence drawing of the bottom spring wire (with reference to Figure 5-10). The inset shows the cross section of the wire. The scale shown is in micrometers, and the grid lines are spaced every 10 micrometers.

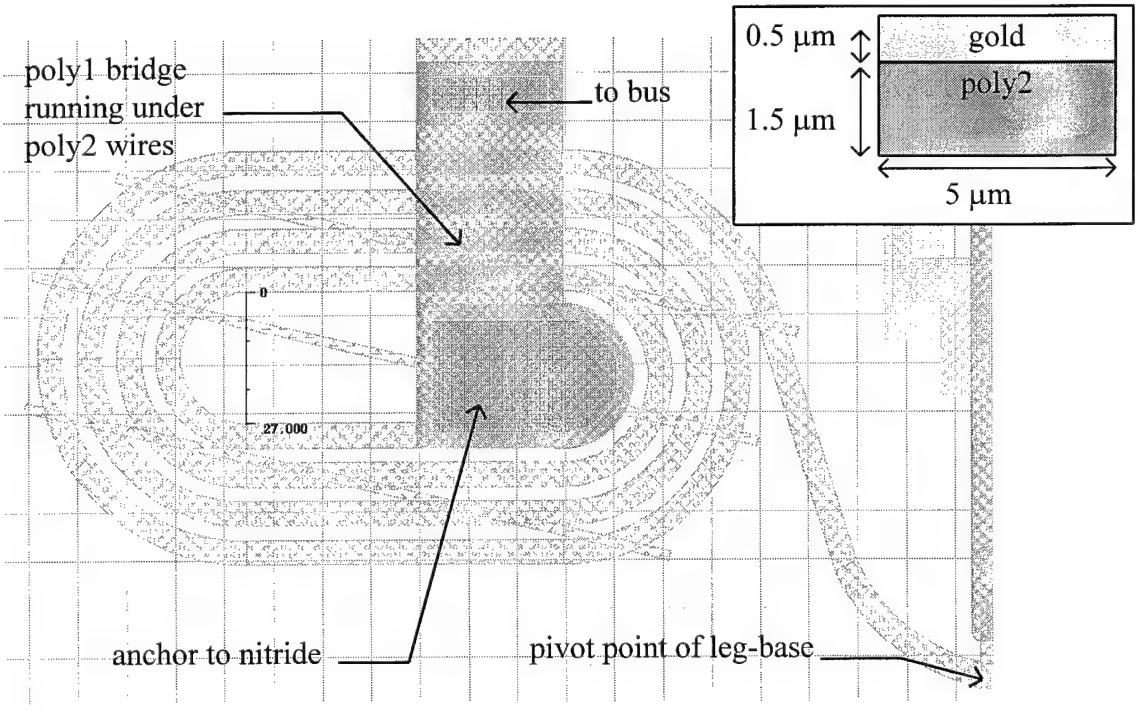

Figure A-6: CADENCE drawing of the left spring wire (with reference to Figure 5-10) showing the cross section of the wire in the inset. The scale shown is in micrometers, and the grid lines are spaced every 10 micrometers.

Since the spring wire is attached to the leg-base, it must be able to yield enough to allow a 90 degree rotation to the upright and final position of the leg-base system. Also, for self assembly to be possible, the mechanically resistive moments applied by the left and right spring wires at the pivot point of the leg-base must be less than the moment applied by the vertically deflecting thermal actuators.

To find an analytical prediction for the mechanically resistive moment, $M_{SWI}(\theta)$, of one spring wire for a given deflection, θ, at the pivot point, one could partition the spring wire into a series of straight and curved beams. Static relations for each partitioned beam could be derived by summing the moments acting on the beam, summing the forces acting on the beam, analyzing deflections of the beam along three axes, and analyzing torsion of the beam about three axes, yielding at least eight relationships. The relationships derived for the eighteen partitioned beams, in this case, could then be related to each other as $8 \times 18 = 144$ linear equations. Using known endpoint conditions at the leg-base-pivot and nitride-anchor points (i.e. θ), the 144 linear equations could then be solved. This method of finding $M_{SWI}(\theta)$ can be tedious and inaccurate since some of the conventional relations used are small angle approximations [1].

In this analysis, $M_{SWI}(\theta)$ will be predicted by modeling the spring wire using finite elements. The Vibration Toolbox for MATLAB is used to perform the finite element analysis [9]. The spring wire is modeled using 138 straight beam elements connected in series at nodes (139 nodes). The number of nodes was chosen by noting

that higher numbers of nodes did not effect any changes of the significant figures of the solution. Each node possess six degrees of freedom, which can be specified: three deflections along and three rotations about the three coordinate axes. Figure A-7 shows the finite element spring wire model, nodes, and reference axes.

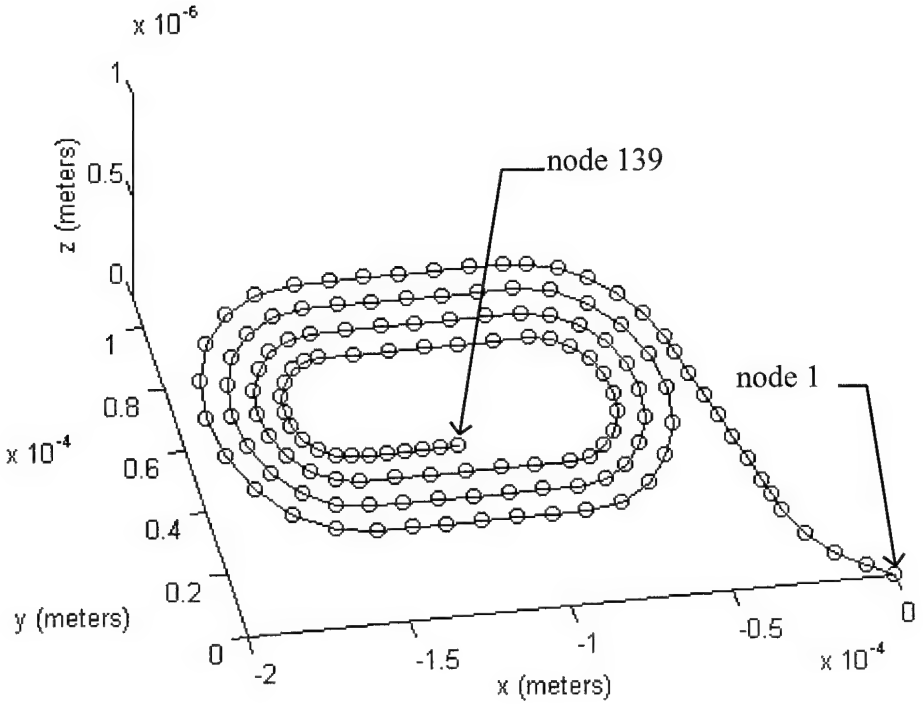

Figure A-7: MATLAB plot of finite element spring wire model showing nodes and reference axes.

The six degrees of freedom for nodes 2 - 138 are unconstrained. For node 139, all the degrees of freedom are constrained, because this is where the spring wire is anchored to the nitride. For node 1, all the degrees of freedom are constrained except for a rotation about the x-axis, because this is where the spring wire is attached to the leg-base.

For this analysis, the material type of each element is considered all poly2. The effects of the gold layer is approximated by an equivalent poly2 layer. The cross sectional area of the gold layer is scaled by the ratio of Young's modulus for gold to Young's modulus for polysilicon. With reference to Figure A-8, b = 5 μm and "a" is determined to be (1.5 + 0.2) = 1.7 μm.

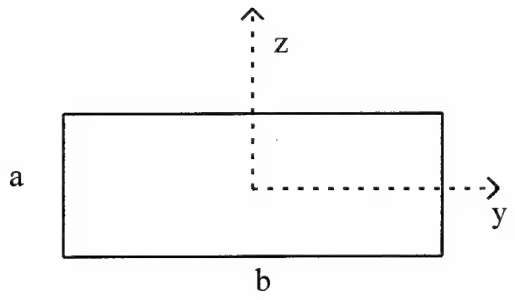

Figure A-8: Cross section of an element showing the reference axes for the element where the x-axis is out of the page, "a" is the thickness, and "b" is the width.

Also, with reference to Figure A-8, the following 2nd moments of area are used:

$$Iyy = (ba^3)/12 \quad \text{(A-21)}$$

$$Izz = (ab^3)/12 \quad \text{(A-22)}$$

$$Ixx = Iyy + Izz \quad \text{(A-23)}$$

$$J = Ixx. \quad \text{(A-24)}$$

Twenty three simulations where performed on a PC, where a single moment ($M_{SW1}(\theta)$) was applied to the system, about the x-axis at node 1, causing a rotational displacement (θ) about the x-axis. The moment was varied and displacements from zero

to pi/2 predicted. Figure A-9 (a-c) shows different viewpoints of the resulting deformation of the spring wire when node 1 has displaced $\theta = pi/2$ radians.

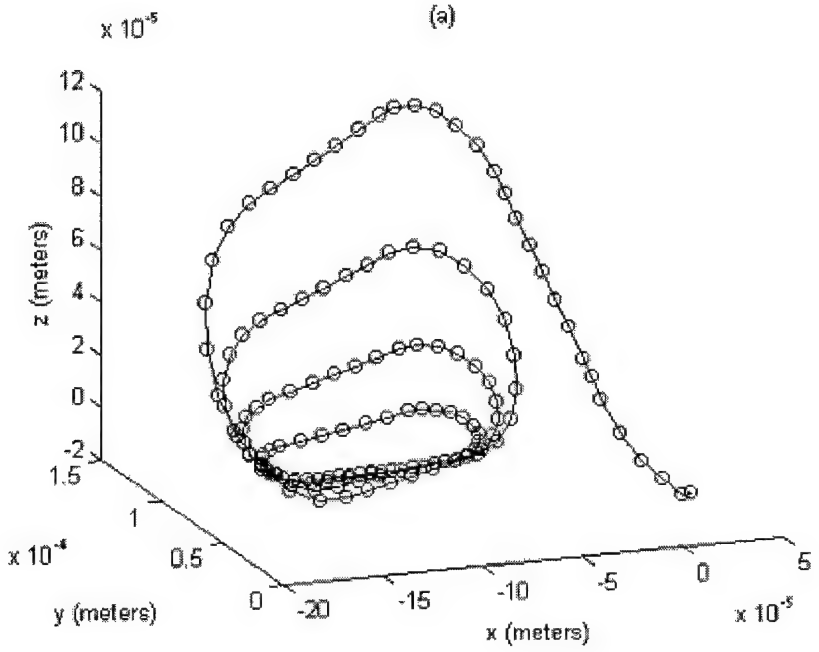

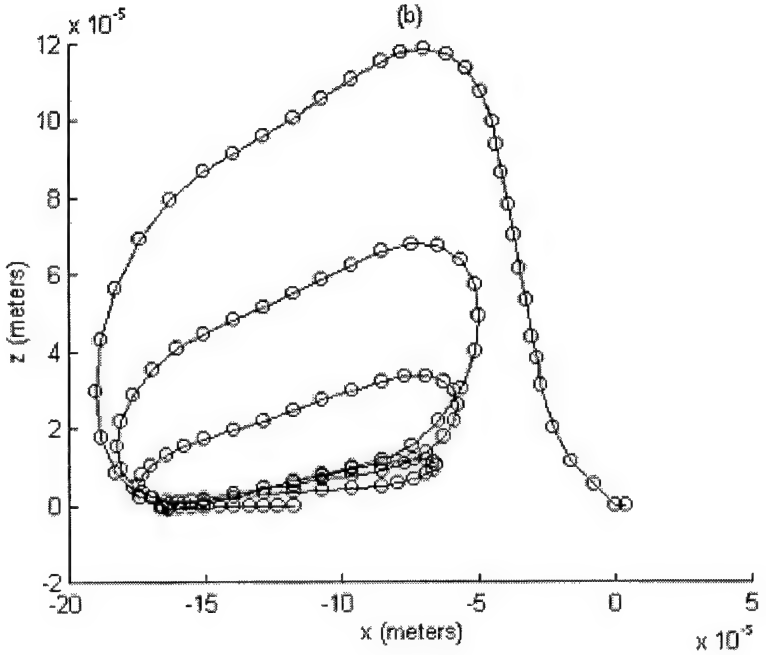

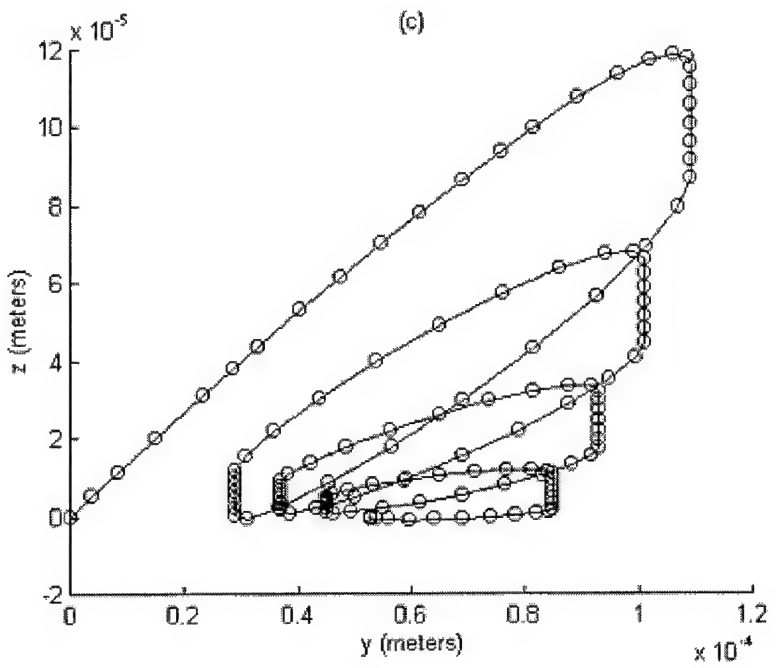

Figure A-9: MATLAB plots (a-c) showing different viewpoints of the spring wire after an angular displacement at node 1 of θ = pi/2.

The resulting forces and moments, at node 1, caused by an angular displacement at node 1 are presented in the following plots. Figure A-10 shows a MATLAB plot of the mechanically resistive moment, $M_{SW1}(\theta)$, at node 1, caused by a given deflection, θ, also at node 1. Figure A-11 shows a MATLAB plot of the resulting force, F_{SW}, parallel to the z-axis at node 1, caused by a given deflection, θ, also at node 1. Recall, F_{SW}, is needed to solve Equation (A-14). Figure A-12 shows a MATLAB plot of the resulting moment, M_{SW1y}, about the y-axis at node 1, caused by a given deflection, θ, also at node 1. The data file created for this finite element analysis is shown in Figure A-13.

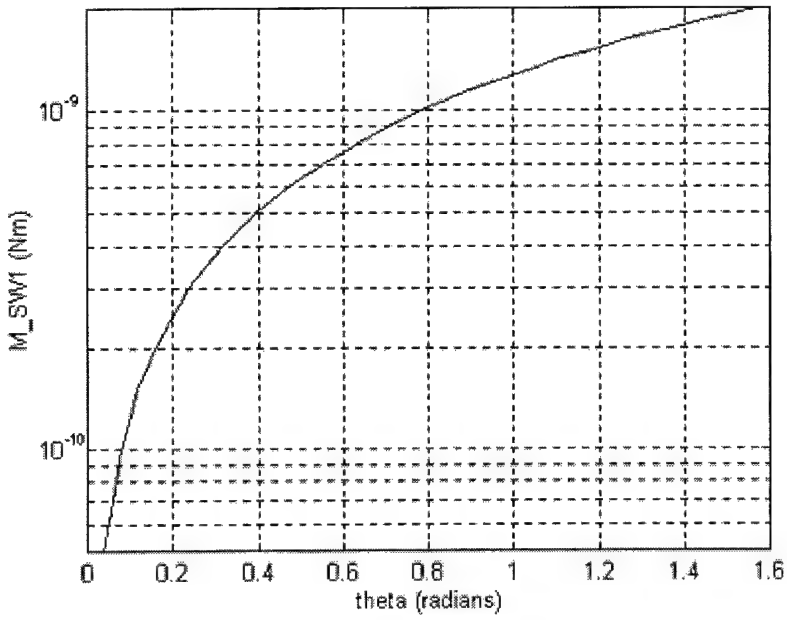

Figure A-10: MATLAB plot showing the mechanically resistive moment, $M_{SW1}(\theta)$, at node 1, caused by a given deflection, θ, also at node 1.

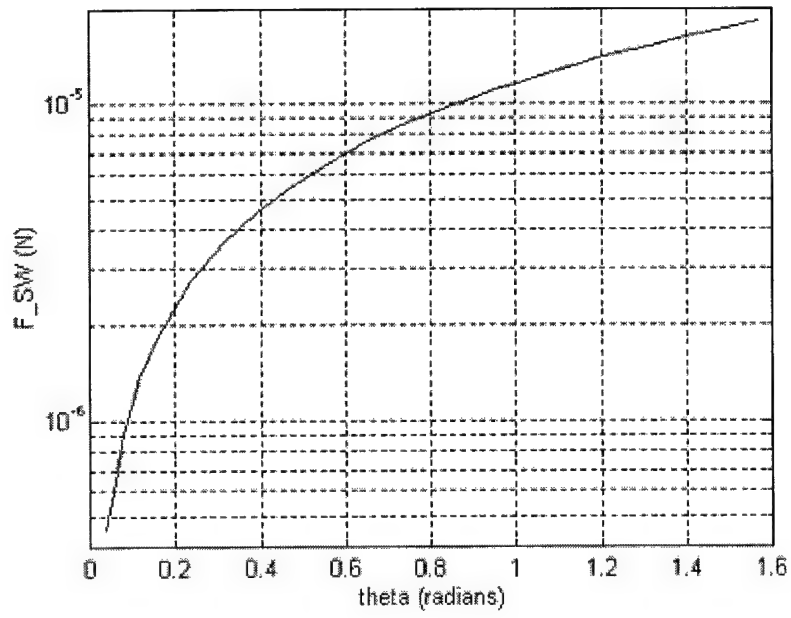

Figure A-11: MATLAB plot showing the resulting force, F_{SW}, parallel to the z-axis at node 1, caused by a given deflection, θ, also at node 1.

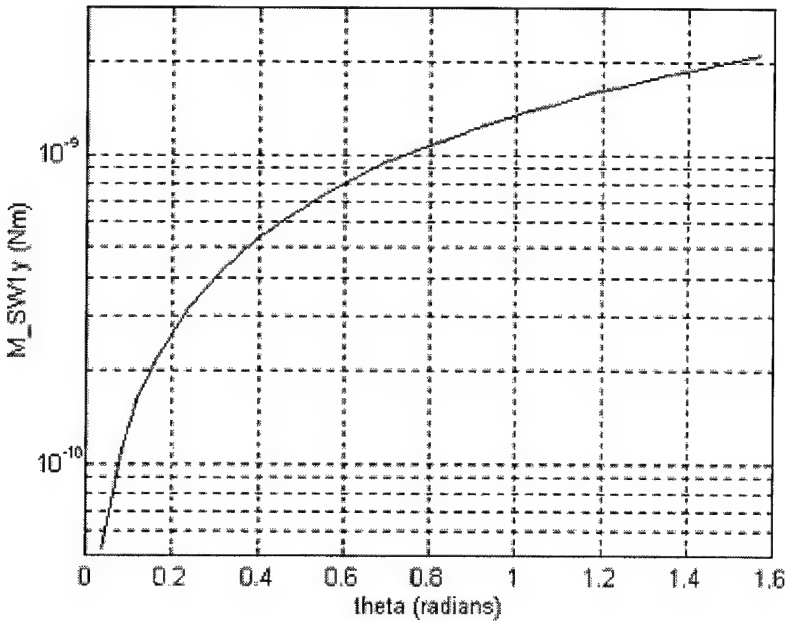

Figure A-12: MATLAB plot showing the resulting moment, M_{SW1y}, about the y-axis at node 1, caused by a given deflection, θ, also at node 1.

```
%spring m
%
%Code written by Paul E. Kladitis
%using Matlab version 4.2c1 on a PC.
%

% First a name for this problem is given.
modelname = 'Spring Wire Using frame6 Elements';

%NMODES = 10;

%3-D coordinates of nodes
%values in matrix are in centimeters, scaler converts to micrometers
delq1=10;
qr=(-pi/2+pi/delq1):pi/delq1:(pi/2-pi/delq1);
ql=(pi/2+pi/delq1):pi/delq1:(3*pi/2-pi/delq1);
delq=6;
nodecoordinates = [
(30e-6/4)*[ 5      0
            0      0
           -1      .5
           -2.1    1.1
           -3      2
           -3.6    3.1
           -3.8    3.8
```

```
        -4      4.4
        -4.3    5.4
        -4.65   6.35
        -4.9    7.3
        -5.15   8.2
        -5.5    9.2
        -5.75   10.1]
1e-6*[ [-85.5+44*cos(0.38:2*1.03/delq1:1.41)]' [65+44*sin(0.38:2*1.03/delq1:1.41)]' ]
1e-6*[ [-85.5:-65/delq:-150.5]' [109*ones(delq+1,1)] ]
1e-6*[ [-150.5+40*cos(ql)]' [69+40*sin(ql)]' ]
1e-6*[ [-150.5:65/delq:-85.5]' [29*ones(delq+1,1)] ]
1e-6*[ [-85.5+36*cos(qr)]' [65+36*sin(qr)]' ]
1e-6*[ [-85.5:-65/delq:-150.5]' [101*ones(delq+1,1)] ]
1e-6*[ [-150.5+32*cos(ql)]' [69+32*sin(ql)]' ]
1e-6*[ [-150.5:65/delq:-85.5]' [37*ones(delq+1,1)] ]
1e-6*[ [-85.5+28*cos(qr)]' [65+28*sin(qr)]' ]
1e-6*[ [-85.5:-65/delq:-150.5]' [93*ones(delq+1,1)] ]
1e-6*[ [-150.5+24*cos(ql)]' [69+24*sin(ql)]' ]
1e-6*[ [-150.5:65/delq:-85.5]' [45*ones(delq+1,1)] ]
1e-6*[ [-85.5+20*cos(qr)]' [65+20*sin(qr)]' ]
1e-6*[ [-85.5:-65/delq:-150.5]' [85*ones(delq+1,1)] ]
1e-6*[ [-150.5+16*cos(ql)]' [69+16*sin(ql)]' ]
1e-6*[ [-150.5:32.5/delq:-118]' [53*ones(delq+1,1)] ] ];
nl=size(nodecoordinates,1);
GNodes=[ [1:nl]', nodecoordinates, zeros(nl,1) ];

%Element properties and connectivity data in order of columns:
%1: element#
%2: elementtype: frame6 (see def_el m for types)
%3: MatProp: row 1 (defined below)
%4: GeoProp: row 1 (defined below)
%5&6: Nodes that form the element
GConnect = [ [1:(nl-1)]' 3*ones(nl-1,1) ones((nl-1),2) [1:(nl-1)]' [2:nl]' ];

%Material Properties:  Young's modulus, Poisson's ratio, and density
MatProp(1,:) = [169e9 0.22 2330];

%Geometric Properties:  cross sectional area (A), moment of inertia
%along longitudinal axis (Ixx), 2 moment of area along perpendicular
%axes (Iyy, Izz), polar moment of inertia for torsion (J)
b=5e-6;             %width
a=1.7e-6;           %thickness
A=a*b;
Iyy = (b*a^3)/12;
Izz = (a*b^3)/12;
Ixx = Iyy+Izz;
J = Ixx;
GeoProp(1,:) = [A Ixx Iyy Izz J];   %A Ixx Iyy Izz J

%Specifies what degrees of freedom of a node are constrained
%node,x,y,z,thetax,thetay,thetaz: 0=free, 1=constrained.
GBound=[ [1:nl]' zeros(nl,6)];
GBound(1,:)=[1 1 1 1 0 1 1];
GBound(nl,:)=[nl 1 1 1 1 1 1];
```

```
GForceC=[1 0 0 0 20e-10 0 0];
probsize;
%End
```

Figure A-13: Data file used to perform the finite element analysis.

To check the numerical result for $M_{SWI}(\theta)$, we can consider the spring wire as one long straight beam of length 1274 μm, and same cross sectional area defined in Figure A-8, subjected to a twist (or torque) about the beam's longitudinal axis. The relation between torque and angular deflection of the end of the beam is given by $T = \frac{GJ}{l}\theta$, where G is the modulus of rigidity J is the polar second moment of area defined in Eq. (A-24) calculated to be 1.9755×10^{-23} m^4, l is the length of the beam. G is related to Young's modulus (E) and Poisson's ratio (ν) [2] by the relation $G = \frac{E}{2(1+\nu)} = \frac{169\times10^9}{2(1+0.22)} = 69.2623\times10^9$ Pa. A plot of T for different values of θ from 0 to $\pi/2$ is shown in Figure A-14. A comparison of Figure A-14 to Figure A-10 shows similar results between the numerical analysis and this simple straight beam approximation.

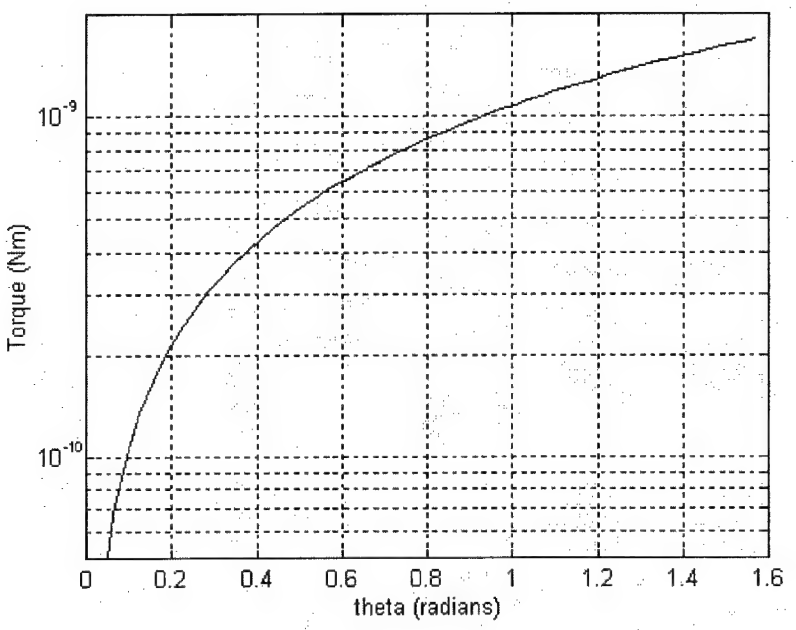

Figure A-14: MATLAB plot of the torque required to twist a long beam an angle θ.

A.8 $F_{LA}l_{LA}\cos(\theta)$: Finding the Moment Caused by the Locking Arms.

The locking arms are shown in Figure 5-10, and a closer view is redrawn in Figure A-15 showing an evolution to the simplified beam used in the modeling.

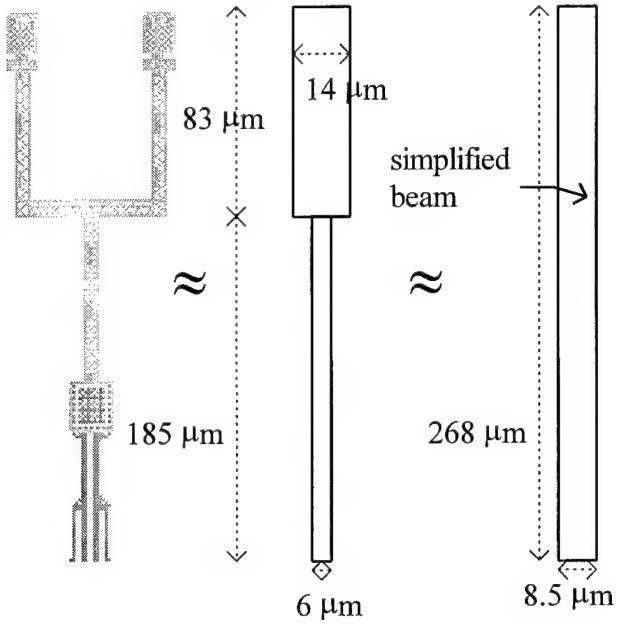

Figure A-15: Drawing of locking arms showing evolution of simplified beams to be used to model it. The rightmost beam is used to model the locking arms.

The simplified beam is found by averaging the area of the locking arms over the same length. The original locking arms possesses the same length and area as the simplified beam. The beam is made from poly2.

The force, F_{LA}, is derived from Figure A-16 which shows a drawing of where the locking arm makes contact with the leg-base:

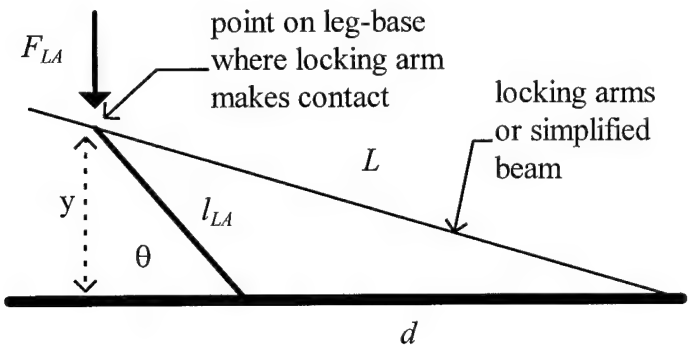

Figure A-16: Drawing of where the locking arm makes contact with the leg-base.

where y is the vertical displacement of the point of contact, l_{LA} = (22 μm), d is the distance from the anchor point of the locking arms to the hinge pin of the leg-base (268 μm), and L is the distance from the anchor point of the locking arms to the point of application of F_{LA}. The force applied to the contact point as the simplified beam bends can be predicted by:

$$F_{LA} = \frac{3EIy}{L^3} \tag{A-25}$$

where

$$y = l_{LA}\sin(\theta) \tag{A-26}$$

and using the law of cosines,

$$L = \sqrt{l_{LA}^2 + d^2 - 2l_{LA}d\cos(\pi - \theta)} \tag{A-27}$$

and E is Young's modulus for polysilicon, and I is defined in Equation (A-21). Combining Equations (A-25) through (A-27), and using the dimensions given in the

preceding paragraphs, we can determine the moment contribution to Equation (A-2) by the locking arms:

$$F_{LA} l_{LA} \cos(\theta) = \frac{3EI(l_{LA}\sin(\theta))}{\left(l_{LA}^2 + d^2 - 2l_{LA}d\cos(\pi-\theta)\right)^{3/2}} l_{LA}\cos(\theta) = \frac{5.8663\times10^{-22}\sin(\theta)\cos(\theta)}{7.2308\times10^{-8} - 1.1792\times10^{-8}\cos(\pi-\theta)} \quad \text{(A-28)}$$

A.9 Static Analysis of the Microrobot Leg: Summing it All Up

Figure A-17 is a plot of the moments from Equation (A-2) versus the angular deflection of the leg-base. By inspection of Figure A-17, we can immediately draw the conclusion that the vertically deflecting thermal actuators can overcome the combination of weight, friction, van der Waals, electrostatic, and locking arm forces. However, the plot also shows that the restoring moment of the spring wires is approximately 37.85 times greater than the moment provided by the thermal actuators at a deflection of pi/2. This analysis predicts that the microrobot legs can not be self assembled because the vertically deflecting thermal actuators can not produce a moment that will overcome the resistive moment of the spring wires.

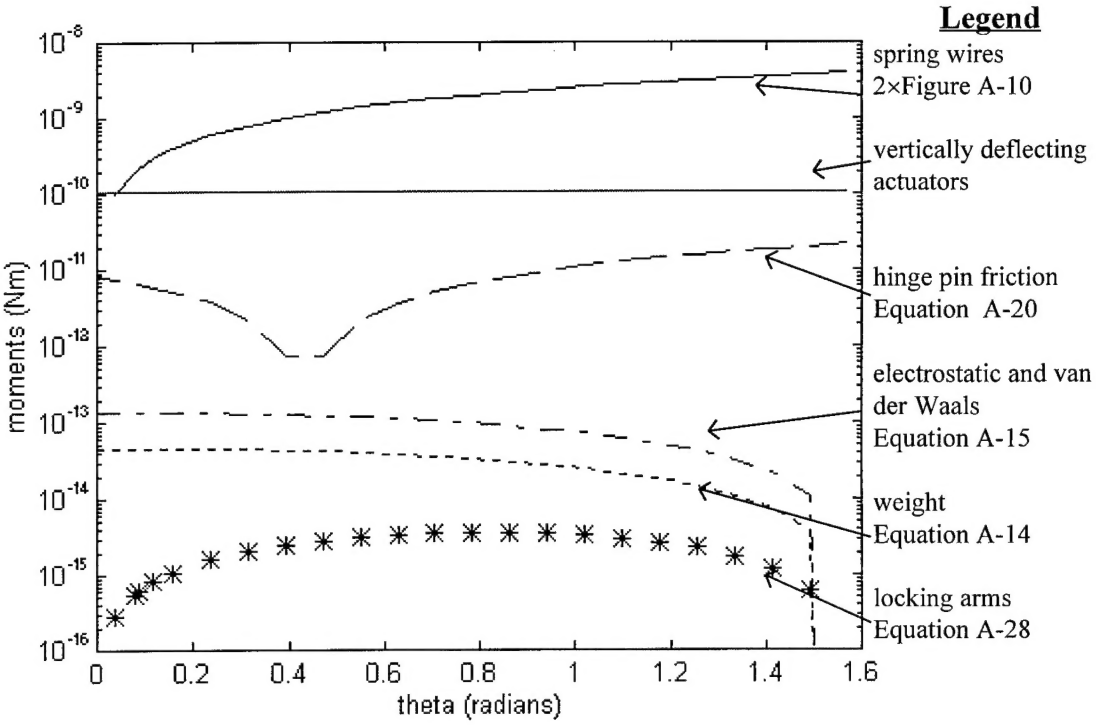

Figure A-17: MATLAB plot of the moments from Equation (A-2) versus angular deflection of the leg-base.

A.10 References

[1] J. E. Shigley and C. R. Mischke, *Mechanical Engineering Design*, 5th ed., McGraw - Hill, 1989.

[2] W. Sharpe, B. Yuan, R. Vaidyanathan, and R. Edwards, "Measurement of Young's Modulus, Poisson's Ratio, and tensile strength of polysilicon," *Proceedings of the 10th Annual International IEEE MEMS Workshop*, pp. 424-429, 1997.

[3] R. A. Serway, *Physics for Scientists & Engineers*, 3rd ed., Saunders College Publishing, 1990.

[4] R. Legtenberg, H. Tilmans, J. Elders, and M. Elwenspoek, "Stiction of surface micromachined structures after rinsing and drying: model and investigation of adhesion mechanisms," *Sensors and Actuators A*, vol. 43, pp. 230-238, 1994.

[5] J. Israelachvili, Intermolecular & Surface Forces, 2nd ed., p. 179, Academic Press, 1992.

[6] J. H. Lee, Y. I. Lee, W. I. Jang, C. S. Lee, and H. J. Yoo, "Gas-phase etching of sacrificial oxides using anyhydrous HF and CH//3OH," *Proceedings of the 10th Annual International Workshop on MEMS*, pp. 448-453, 1997.

[7] P. F. Man, B. P. Gogoi, and C. H. Mastrangelo, "Elimination of post-release adhesion in mocrostructures using conformal flourocarbon coatings," *Journal of Microelectromechanical Systems*, vol. 6, no. 1, pp. 25-34, March 1997.

[8] T. Abe and M. L. Reed, "Control of liquid bridging induced stiction of micromechanical structures," *Journal of Micromechanics and Microengineering*, vol. 6, no. 2, June 1996.

[9] M. J. Atalla and J. C. Slater, "The Vibration Toolbox: Finite Elements using MATLAB," Garman Systems Inc., Version 1.0, February 1996.

Appendix B: Vita

Second Lieutenant Paul E. Kladitis was born on 23 January 1969 in Youngstown, Ohio and raised in Dayton, Ohio. He graduated from Meadowdale High School in 1987 and enlisted in the U. S. Army as an infantry soldier. His first assignment was with CSC Company, 1st Battalion, 506th Infantry, Korea, as a first line of defense against North Korea on the 48th parallel. His next assignment was with Troop D, 6th Squadron, 12th Cavalry Regiment, Ft. Knox, Kentucky in the operations section. Other duties included unit armorer and caretaker of the domestic and foreign weapons collection at the Patton Museum. He attained the rank of Sergeant before his honorable discharge on 9 September 1991.

Upon discharge from the Army he entered undergraduate studies at Wright State University in Dayton, Ohio. He graduated Summa Cum Laude with a Bachelor of Science in Electrical Engineering in March 1996. He received his reserve commission on 1 April 1996 upon graduation from the U. S. Air Force Reserve Officer Training Corps. He received his regular commission on 31 July 1996. In May 1996, he entered the School of Engineering, Air Force Institute of Technology.

Permanent Address: 240 W. Norman Ave.
Dayton, OH 45405

REPORT DOCUMENTATION PAGE

Form Approved
OMB No. 0704-0188

1. AGENCY USE ONLY *(Leave blank)*	2. REPORT DATE	3. REPORT TYPE AND DATES COVERED
	December 1997	Master's Thesis

4. TITLE AND SUBTITLE
SELF ASSEMBLY OF MICROSTRUCTURES

5. FUNDING NUMBERS

6. AUTHOR(S)
Paul E. Kladitis, Second Lieutenant, USAF

7. PERFORMING ORGANIZATION NAME(S) AND ADDRESS(ES)
Air Force Institute of Technology
2750 P. Street
WPAFB, OH 45433-7765

8. PERFORMING ORGANIZATION REPORT NUMBER
AFIT/GE/ENG/97D-02

9. SPONSORING/MONITORING AGENCY NAME(S) AND ADDRESS(ES)
Phillips Laboratory (PL/VTMR)
Major John H. Comtois
3550 Aberdeen Ave. S. E.
Kirtland AFB, New Mexico 87117-5776

10. SPONSORING/MONITORING AGENCY REPORT NUMBER

11. SUPPLEMENTARY NOTES

12a. DISTRIBUTION AVAILABILITY STATEMENT
Approved for public release; distribution unlimited

12b. DISTRIBUTION CODE

13. ABSTRACT *(Maximum 200 words)*

Four areas are investigated in this research: erecting microstructures normal to the substrate plane without direct human intervention (self assembled), providing low resistance electrical connections to the erected microstructure, realizing circular motion normal to the substrate plane, and implementing a microrobot. The designs in this research concentrate on erecting and providing power to a leg designed for use with the microrobot. The leg and the attached low resistance electrical connectors were not self assembled because the accompanying actuators were not powerful enough. However, the novel connectors provide the most practical, versatile, and lowest possible resistance connections for the MUMPs fabrication process. The microrobot was a 1 cm by 1 cm by 0.125 mm thick silicon chip with ninety-six legs micromachined on one side. The legs were able to support the weight of the chip but could not move the chip bec. The gold wires used to remotely power the legs, restricted the chip's movement. The chip was turned over, and used as a micropositioner to transport a 1 cm by 1 cm by 0.023 mm piece of kapton film. A vertically deflecting actuator was used to bump the edge of a 222 mm diameter wheel, causing circular motion normal to the substrate.

14. SUBJECT TERMS
Micro-Electro-Mechanical Systems (MEMS), self assembly, automated assembly, micro assembly, microrobot, robot, micro positioner, micro wheel, micro wires, spring wires, micro unmanned vehicles

15. NUMBER OF PAGES
192

16. PRICE CODE

17. SECURITY CLASSIFICATION OF REPORT	18. SECURITY CLASSIFICATION OF THIS PAGE	19. SECURITY CLASSIFICATION OF ABSTRACT	20. LIMITATION OF ABSTRACT
Unclassified	Unclassified	Unclassified	UL